



Ministério da
Ciência e Tecnologia



INPE-13269-MAN/45 - versão 1

DYNAMICS OF CORONAL MASS EJECTIONS IN THE INTERPLANETARY MEDIUM

Andrea Inés Borgazzi

PhD Thesis of the Post-Graduation Space Geophysics Course, advisored by Drs.
Maria Virgínia Alves, Ezequiel Echer and Alejandro Lara, and approved on May
26, 2009

The original of this document is available at:
<<http://urlib.net/sid.inpe.br/iris@1916/2005/05.19.15.27>>

INPE
São José dos Campos
2009

Livros Grátis

<http://www.livrosgratis.com.br>

Milhares de livros grátis para download.

PUBLICADO POR:

Instituto Nacional de Pesquisas Espaciais - INPE

Gabinete do Diretor (GB)

Serviço de Informação e Documentação (SID)

Caixa Postal 515 - CEP 12.245-970

São José dos Campos - SP - Brasil

Tel.:(012) 3945-6911/6923

Fax: (012) 3945-6919

E-mail: pubtc@sid.inpe.br

CONSELHO DE EDITORAÇÃO:

Presidente:

Dr. Gerald Jean Francis Banon - Coordenação Observação da Terra (OBT)

Membros:

Dra. Maria do Carmo de Andrade Nono - Conselho de Pós-Graduação

Dr. Haroldo Fraga de Campos Velho - Centro de Tecnologias Especiais (CTE)

Dra. Inez Staciaroni Batista - Coordenação Ciências Espaciais e Atmosféricas (CEA)

Marciana Leite Ribeiro - Serviço de Informação e Documentação (SID)

Dr. Ralf Gielow - Centro de Previsão de Tempo e Estudos Climáticos (CPT)

Dr. Wilson Yamaguti - Coordenação Engenharia e Tecnologia Espacial (ETE)

BIBLIOTECA DIGITAL:

Dr. Gerald Jean Francis Banon - Coordenação de Observação da Terra (OBT)

Marciana Leite Ribeiro - Serviço de Informação e Documentação (SID)

Jefferson Andrade Ancelmo - Serviço de Informação e Documentação (SID)

Simone A. Del-Ducca Barbedo - Serviço de Informação e Documentação (SID)

REVISÃO E NORMALIZAÇÃO DOCUMENTÁRIA:

Marciana Leite Ribeiro - Serviço de Informação e Documentação (SID)

Marilúcia Santos Melo Cid - Serviço de Informação e Documentação (SID)

Yolanda Ribeiro da Silva e Souza - Serviço de Informação e Documentação (SID)

EDITORAÇÃO ELETRÔNICA:

Viveca Sant'Ana Lemos - Serviço de Informação e Documentação (SID)



Ministério da
Ciência e Tecnologia



INPE-13269-MAN/45 - versão 1

DYNAMICS OF CORONAL MASS EJECTIONS IN THE INTERPLANETARY MEDIUM

Andrea Inés Borgazzi

PhD Thesis of the Post-Graduation Space Geophysics Course, advisored by Drs.
Maria Virgínia Alves, Ezequiel Echer and Alejandro Lara, and approved on May
26, 2009

The original of this document is available at:
<<http://urlib.net/sid.inpe.br/iris@1916/2005/05.19.15.27>>

INPE
São José dos Campos
2009

Cataloging in Publication Data

Cutter Andrea Inés Borgazzi.

DYNAMICS OF CORONAL MASS EJECTIONS
IN THE INTERPLANETARY MEDIUM/ Andrea Inés
Borgazzi. – São José dos Campos: INPE, 2009.

136p. ; (INPE-13269-MAN/45 - versão 1)

1. ICME. 2. Transport in the Interplanetary Medium /
Transporte no meio interplanetário. 3. Drag Force / Força
de arrasto. 4. Travel Time / Tempo de viagem. 5. Viscosity
/ Viscosidade.

CDU

**ATENÇÃO! A FOLHA DE
APROVAÇÃO SERÁ INCLU-
IDA POSTERIORMENTE.**

.

*Ojos de salamandra,
Diente de dragon,
Pelo de cola de raton para hacer la poción.
Todos los conjuros son posibles, solo hay que creer en ellos.
(no hay virus que me detenga)*

ABSTRACT

In this work we present an accurate description of the Interplanetary Coronal Mass Ejections (ICMEs) dynamics in their travel from Sun to Earth. We propose a mechanism of momentum transfer between ICMEs and the surrounding solar wind that decelerate the fast ICMEs ($V_{cme} > V_{sw}$). In this case, the deceleration involves viscous forces acting between the ICME and the surrounding medium. We solve the differential equations that describe the process using different expressions for the viscous force. We find solutions that include the variability of the ICME radio and the mass density of the medium and find out the speed behavior of the ICMEs versus the traveled distance. We present the analytical solutions with the corresponding in situ and remote data analysis and discuss the implications of the different parameters involved in this mechanism of momentum transfer. We consider the ICME mass, (m_{cme}), the density of the interplanetary medium, the solar wind speed, (V_{sw}), the exponent of radial expansion of the ICME, (p), the drag coefficient, (C_d), and kinematic viscous coefficient, (ν).

DINÂMICA DAS EJEÇÕES CORONAIS DE MASSA NO MEIO INTERPLANETÁRIO

RESUMO

Neste trabalho nós apresentamos uma descrição acurada da dinâmica das ejeções coronais de massa interplanetárias (ICMEs) em sua viagem do Sol à Terra. Nós propomos um mecanismo de transferência de momento entre as ICMEs e o vento solar que a circunda que desacelera as ICMEs rápidas ($V_{cme} > V_{sw}$). Neste caso, a desaceleração envolve a ação de forças entre a ICME e o meio que a circunda. Nós resolvemos as equações diferenciais que descrevem o processo e usamos diferentes expressões para a força viscosa, de acordo com o número de Reynolds. Nós encontramos soluções que incluem a variabilidades do raio da ICME bem como a da densidade de massa do meio interplanetário. Nós encontramos o comportamento da velocidade da ICME versus a distância percorrida e apresentamos as soluções analíticas com a correspondente análise de dados remotos e in situ. Nós discutimos as implicações dos diferentes parâmetros envolvidos neste processo de transferência de momento. Nós consideramos a massa da ICME, (m_{cme}), a densidade do meio interplanetário, a velocidade do vento solar, (V_{sw}), o expoente da expansão radial das ICMEs, (p), o coeficiente de arrasto, (C_d), e o coeficiente da viscosidade cinética, (ν).

CONTENTS

Pág.

LIST OF FIGURES

LIST OF TABLES

| | |
|--|-----------|
| 1 INTRODUCTION | 25 |
| 1.1 Coronal and Interplanetary Mass Ejections | 26 |
| 1.1.1 Geoeffectiveness of CMEs-ICMEs | 27 |
| 1.2 Transport models | 29 |
| 1.2.1 Theoretical models | 29 |
| 1.2.2 Empirical models | 29 |
| 1.2.3 Numerical Simulations | 30 |
| 1.3 Scope of the present work | 30 |
| 2 CORONAL AND INTERPLANETARY MASS EJECTIONS | 33 |
| 2.1 Coronal Mass Ejections (CMEs) | 33 |
| 2.1.1 Flux rope model and flux cancellation | 35 |
| 2.1.2 The breakout model | 35 |
| 2.1.3 Flux injection model | 36 |
| 2.2 Interplanetary coronal mass ejections (ICMEs) | 36 |
| 3 HYDRODYNAMICS THEORY | 39 |
| 3.1 Strain state of a body | 39 |
| 3.1.1 Linear or normal strain rate of a fluid | 39 |
| 3.1.2 Shear strain rate of a fluid | 40 |
| 3.2 Vorticity | 41 |
| 3.3 Conservation laws | 42 |
| 3.3.1 Control-volume formulations | 42 |
| 3.3.2 Conservation of mass | 44 |
| 3.3.3 Conservation of linear momentum | 45 |
| 3.4 Newton's law | 45 |
| 3.5 Navier-Stokes equation | 47 |
| 3.6 Reynolds's number | 48 |

| | | |
|----------|---|-----------|
| 3.7 | Derivation of Navier-Stokes equation for high and low Reynolds number . | 48 |
| 3.8 | Derivation of laminar drag force | 49 |
| 3.9 | Derivation of turbulent drag force | 50 |
| 3.9.1 | Laminar boundary layers | 50 |
| 3.9.2 | The displacement thickness | 52 |
| 3.9.3 | Momentum thickness related to the flat plate drag | 52 |
| 4 | HYDRODYNAMICS MODEL FOR THE TRANSPORT IN THE INTERPLANETARY MEDIUM OF CORONAL MASS EJECTIONS | 55 |
| 4.1 | ICME - SW interaction - Time dependence | 55 |
| 4.1.1 | Variability of ICME radius | 55 |
| 4.2 | ICME - SW interaction - Position dependence | 57 |
| 4.2.1 | ICME Initial conditions | 57 |
| 4.2.2 | Variability of ICME radius | 58 |
| 4.2.3 | ICME interplanetary medium density and radius variable | 59 |
| 4.2.3.1 | Turbulent Regime | 60 |
| 4.2.3.2 | Laminar Regime | 60 |
| 4.3 | Results | 61 |
| 4.3.1 | ICME - SW interaction - Time dependence | 61 |
| 4.3.2 | ICME - SW interaction - Distance dependence (case a) | 62 |
| 4.3.3 | ICME - SW interaction - Distance dependence (case b) | 64 |
| 4.4 | Variation of parameters | 65 |
| 4.4.1 | Methodology | 67 |
| 4.4.2 | Results - Variation of parameters | 69 |
| 4.4.2.1 | Turbulent regime | 69 |
| 4.4.2.2 | Laminar regime | 72 |
| 4.4.2.3 | K - S test result, laminar regime | 77 |
| 4.4.2.4 | K - S test result, turbulent regime | 78 |
| 5 | DATA | 81 |
| 5.1 | Data Analysis | 81 |
| 5.2 | Satellite data | 82 |
| 5.2.1 | Data - At 1 AU | 82 |
| 5.2.2 | Insitu data - at distances lower than 1 AU | 84 |
| 5.2.3 | Results - Satellite data | 84 |

| | | |
|----------|--|------------|
| 5.3 | Type II burst data | 90 |
| 5.4 | Method: Type II burst-ICME speed versus position | 92 |
| 5.4.1 | Results - Type II burst data | 92 |
| 6 | RESULTS AND DISCUSSION | 103 |
| 6.1 | Results for the events detected by satellites at 1 AU | 103 |
| 6.2 | Results for the events detected by satellites at distances lower than 1 AU | 103 |
| 6.3 | Type II burst | 104 |
| 6.4 | ICME Travel Time | 109 |
| 6.5 | The drag term | 112 |
| 6.6 | ICME speed versus distance | 114 |
| 7 | CONCLUSION AND FUTURE WORKS | 117 |
| | REFERENCES | 119 |
| A | ENERGETICS CONSIDERATION | 127 |
| B | KOLMOGOROV-SMIRNOV TEST | 129 |
| C | THEORY - TYPE II BURST | 131 |
| C.1 | Mechanism of plasma emission | 132 |
| C.1.1 | Induced scattering | 134 |
| C.1.2 | Alternative forms of plasma emission | 135 |

LIST OF FIGURES

| | <u>Pág.</u> |
|---|-------------|
| 1.1 CME observed by LASCO (C2), date: 6 June of 2000, 18:42 UT. | 28 |
| 1.2 Sequence of images in Fe XII (19.5 nm), with the method of running difference images. It is easy to see the dimining region in black. Event May 12 of 1997. | 28 |
| 3.1 Illustration of the linear strain rate in a fluid. | 40 |
| 3.2 Illustration of shear strain rate in a fluid. | 41 |
| 3.3 Control volume. | 42 |
| 3.4 Surface stress on a fluid element. | 46 |
| 3.5 Boundary layer for high \Re number in a flat plate. | 51 |
| 4.1 Schematic representation of the total viscous force F_v which decelerates the ICME during the travel in the interplanetary space. | 56 |
| 4.2 Solar wind speed versus distance (continuous line), Leblanc density model versus distance (diamonds line) and density profile $1/x^2$ (dotted line) versus distance (distance in R_\odot). | 58 |
| 4.3 a) Evolution of the ICME speed in terms of the initial CME speed under the laminar drag force. The dotted lines correspond to a viscous coeffi- cient of 0.002 kg/m.s and the continuous lines to 0.02 kg/m.s. The stars and triangles represent the travel time from the Sun to 1 AU. b) Tempo- ral behavior of the ICME speed under a turbulent drag force- The dotted lines correspond to a drag coefficient of 200 and the continuous lines to a value of 2000. | 62 |
| 4.4 ICME speed in terms of time, for laminar plus turbulent forces. Dotted lines represent a drag and viscous coefficient of 200 and 0.002 kg/m.s respectively, and continuous lines a drag coefficient of 2000 and a viscous coefficient of 0.02 kg/m.s. | 63 |
| 4.5 a) ICME speed in terms of the distance to the Sun for the laminar in- teraction. Two cases are shown: the dotted lines represent the behavior using a viscous coefficient of 0.002 kg/m.s, and the continuous lines with a coefficient of 0.02 kg/m.s. b) Similar to Figure (4.5 a) but for the tur- bulent force. Dotted lines represent the behavior under a drag coefficient of 200, and the continuos lines with a coefficient of 2000. | 63 |

| | | |
|------|---|----|
| 4.6 | Similar to Figure (4.5) but for the laminar plus turbulent forces. Dotted lines represent the ICME behavior under a drag coefficient of 200 and a viscous coefficient of 0.002 kg/m.s, and the continuous lines with a coefficient of 2000 and a viscous coefficient equal to 0.02 kg/m.s. | 64 |
| 4.7 | a) ICME speed versus distance for laminar regime, showing a weak ($\mu=0.1$ g/cm.s in continuous lines) and strong ($\mu=0.25$ g/cm.s in dotted lines) ICME-SW interaction. Here and in the following figures, the y-axis at distance equal to zero, indicates the initial CME speed used to obtain the curves. b) ICME speed versus distance for turbulent regime, showing a weak ($C_d = 6 \times 10^4$ in continuous lines) and strong ($C_d = 1.6 \times 10^5$ in dotted lines) ICME-SW interaction. | 65 |
| 4.8 | a) ICME speed versus distance for turbulent regime considering ICME radius and SW density variable. The ICME-SW interaction is weak for a drag coefficient $C_d = 2 \times 10^4$ (continuous lines) and strong for $C_d = 8 \times 10^4$ (dotted lines). b) ICME speed versus distance for laminar regime considering ICME radius and SW density variable, in this case the value of the kinematic viscosity is 5×10^{20} cm ² /s for the weak ICME-SW interaction (continuous lines) and 1.25×10^{21} cm ² /s for the strong interaction (dotted lines). | 66 |
| 4.9 | a) Speed versus distance family solutions for the turbulent regime with the variation of mass (m_{cme}) parameter presented in Table (4.1) (second line). b) Speed versus distance family solutions for the turbulent regime with the variation of solar wind velocity (V_{sw}) parameter presented in Table (4.1) (fifth line). | 70 |
| 4.10 | a) Speed versus distance family solutions for the turbulent regime with the variation of density parameter presented in Table (4.1) (third line). b) Speed versus distance family solutions for the turbulent regime with the variation of exponent (p) parameter presented in Table (4.1) (fourth line). | 70 |
| 4.11 | Speed versus distance family solutions for the turbulent regime with the variation of drag coefficient (C_d) parameter presented in Table (4.1) (first line). | 71 |

| | | |
|------|--|----|
| 4.12 | a) Speed versus distance family solutions for the turbulent regime with the variation of mass (m_{cme}) parameter presented in Table (4.3) (second line). b) Speed versus distance family solutions for the turbulent regime with the variation of solar wind velocity (V_{sw}) parameter presented in Table (4.3) (fifth line). | 72 |
| 4.13 | a) Speed versus distance family solutions for the turbulent regime with the variation of density parameter presented in Table (4.3) (third line). b) Speed versus distance family solutions for the turbulent regime with the variation of exponent (p) parameter presented in Table (4.3) (fourth line). | 72 |
| 4.14 | Speed versus distance family solutions for the turbulent regime with the variation of drag coefficient (C_d) parameter presented in Table (4.3) (first line). | 73 |
| 4.15 | a) Speed versus distance family solutions for the laminar regime with the variation of mass (m_{cme}) parameter presented in Table (4.2) (second line). b) Speed versus distance family solutions for the laminar regime with the variation of solar wind (V_{sw}) parameter presented in Table (4.2) (fifth line). | 73 |
| 4.16 | a) Speed versus distance family solutions for the laminar regime with the variation of density parameter presented in Table (4.2) (third line). b) Speed versus distance family solutions for the laminar regime with the variation of exponent (p) parameter presented in Table (4.2) (fourth line). | 74 |
| 4.17 | Speed versus distance family solutions for the laminar regime with the variation of kinematic viscous coefficient (ν) parameter presented in Table (4.2) (first line). | 74 |
| 4.18 | a) Speed versus distance family solutions for the laminar regime with the variation of mass (m_{cme}) parameter presented in Table (4.4) (second line). b) Speed versus distance family solutions for the laminar regime with the variation of solar wind (V_{sw}) parameter presented in Table (4.4) (fifth line). | 75 |
| 4.19 | a) Speed versus distance family solutions for the laminar regime with the variation of density parameter presented in Table (4.4) (third line). b) Speed versus distance family solutions for the laminar regime with the variation of exponent (p) parameter presented in Table (4.4) (fourth line). | 76 |

| | | |
|------|--|----|
| 4.20 | Speed versus distance family solutions for the laminar regime with the variation of kinematic viscous coefficient (ν) parameter presented in Table (4.4) (first line). | 76 |
| 4.21 | a) Result of the K-S test for the laminar case using the five parameters: Mass (m_{cme}) (dash line), Solar wind velocity (V_{sw}) (dash-dot-dot-dot line), Density (dash-dot line), Exponent (p) (dot line), and Kinematic viscous coefficient (ν) (continuous line). As presented in Table (4.2). b) Result of the K-S test for the laminar using the five parameters: Mass (m_{cme}) (dash line), Solar wind velocity (V_{sw}) (dash-dot-dot-dot line), Density (a) (dash-dot line), Exponent (p) (dot line), and Kinematic viscous coefficient (ν) (continuous line). As presented in Table (4.4). | 77 |
| 4.22 | a) Result of the K-S test for the turbulent case using the five parameters: Mass (m_{cme}) (dash line), Solar wind velocity (V_{sw}) (dash-dot-dot-dot line), Density (dash-dot line), Exponent (p) (dot line), and Drag Coefficient (C_d)(continuous line). Table (4.1). b) Result of the K-S test for the turbulent using the five parameters: Mass (m_{cme}) (dash line), Solar wind velocity (V_{sw}) (dash-dot-dot-dot line), Density (dash-dot line), Exponent (p) (dot line), and Drag Coefficient (C_d)(continuous line). Variation parameter of 10 %. Table (4.3). | 78 |
| 5.1 | a) Kilometric (km) type II burts event (good), September 5, 2002. Model: Turbulent regime (dotted line, fundamental and first harmonic), Laminar regime (continuous line, fundamental and first harmonic). b) Decametric (DH) type II burts event (good), September 5, 2002. Model: Turbulent regime (dotted line, fundamental and first harmonic), Laminar regime (continuous line, fundamental and first harmonic). | 95 |
| 5.2 | a) Kilometric (km) type II burts event (regular), November 4, 2001. Model: Turbulent regime (dotted line, fundamental and first harmonic), Laminar regime (continuous line, fundamental and first harmonic). b) Decametric (DH) type II burts event (regular), November 4, 2001. Model: Turbulent regime (dotted line, fundamental and first harmonic), Laminar regime (continuous line, fundamental and first harmonic). | 95 |

| | | |
|-----|---|-----|
| 5.3 | a) Kilometric (km) type II burts event (questionable), May 28, 2003. Model: Turbulent regime (dotted line, fundamental and first harmonic), Laminar regime (continuous line, fundamental and first harmonic). b) Decametric (DH) type II burts event (questionable), May 28, 3003. Model: Turbulent regime (dotted line, fundamental and first harmonic), Laminar regime (continuous line, fundamental and first harmonic). | 96 |
| 5.4 | Kilometric (km) type II burts event (good), a) November 22, 2001, b) October 19, 2001, c) November 7, 2004, d) April 17, 2002, e) September 16, 2000. Model: Turbulent regime (dotted line, fundamental and first harmonic), Laminar regime (continuous line, fundamental and first harmonic). | 97 |
| 5.5 | Decametric (DH) type II burts event (good), a) November 22, 2001, b) October 19, 2001, c) November 7, 2004, d) April 17, 2002, e) September 16, 2000. Model: Turbulent regime (dotted line, fundamental and first harmonic), Laminar regime (continuous line, fundamental and first harmonic). | 98 |
| 5.6 | Kilometric (km) type II burts event (regulars), a) August 16, 2002, b) March 29, 2001, c) April 15, 2001, d) July 14, 2000, e) October 29, 2003. Model: Turbulent regime (dotted line, fundamental and first harmonic), Laminar regime (continuous line, fundamental and first harmonic). . . . | 99 |
| 5.7 | Decametric (DH) type II burts event (regulars), a) August 16, 2002, b) March 29, 2001, c) April 15, 2001, d) July 14, 2000, e) October 29, 2003. Model: Turbulent regime (dotted line, fundamental and first harmonic), Laminar regime (continuous line, fundamental and first harmonic). . . . | 100 |
| 5.8 | Kilometric (km) type II burts event (questionables), a) October 28, 2003, b) April 10, 2001. Model: Turbulent regime (dotted line, fundamental and first harmonic), Laminar regime (continuous line, fundamental and first harmonic). | 101 |
| 5.9 | Decametric (DH) type II burts event (questionables), a) October 28, 2003, b) April 10, 2001. Model: Turbulent regime (dotted line, fundamental and first harmonic), Laminar regime (continuous line, fundamental and first harmonic). | 101 |
| 6.1 | Histograms for coefficients ν and C_d . Case: Satellite at 1 AU, Table (5.3). a) Laminar regime, b) Turbulent regime. | 103 |
| 6.2 | Histograms for radial exponent p . Case: Satellite at 1 AU, Table (5.3). a) Laminar regime, b) Turbulent regime. | 104 |

| | | |
|------|---|-----|
| 6.3 | Histograms for mass m_{cme} . Case: Satellite at 1 AU, Table (5.3). a) Laminar regime, b) Turbulent regime. | 104 |
| 6.4 | Histograms for density. Case: Satellite at 1 AU, Table (5.3). a) Laminar regime, b) Turbulent regime. | 105 |
| 6.5 | Histograms for solar wind velocity V_{sw} . Case: Satellite at 1 AU, Table (5.3). a) Laminar regime, b) Turbulent regime. | 105 |
| 6.6 | Model ICME speed versus distance. Case: Satellite at 1 AU, a) Laminar regime, b) Turbulent. | 106 |
| 6.7 | Histograms for coefficients ν and C_d . Case: Satellite at distances lower than 1 AU, Table (5.5). a) Laminar regime, b) Turbulent regime. | 106 |
| 6.8 | Histograms for radial exponent p . Case: Satellite at distances lower than 1 AU, Table (5.5). a) Laminar regime, b) Turbulent regime. | 107 |
| 6.9 | Histograms for mass m_{cme} . Case: Satellite at distances lower than 1 AU, Table (5.5). a) Laminar regime, b) Turbulent regime. | 107 |
| 6.10 | Histograms for density. Case: Satellite at distances lower than 1 AU, Table (5.5). a) Laminar regime, b) Turbulent regime. | 108 |
| 6.11 | Histograms for solar wind velocity V_{sw} . Case: Satellite at distances lower than 1 AU, Table (5.5). a) Laminar regime, b) Turbulent regime. | 108 |
| 6.12 | Model ICME speed versus distance. Case: Satellite at distances lower than 1 AU, a) Laminar regime, b) Turbulent. The diamonds correspond to the satellite position and velocity of ICME for each event. | 109 |
| 6.13 | Histograms for coefficients ν and C_d . Case: Type II burst, Table (5.8). a) Laminar regime, b) Turbulent regime. | 109 |
| 6.14 | Histograms for radial exponent p . Case: Type II burst, Table (5.8). a) Laminar regime, b) Turbulent regime. | 110 |
| 6.15 | Histograms for mass m_{cme} . Case: Type II burst, Table (5.8). a) Laminar regime, b) Turbulent regime. | 110 |
| 6.16 | Histograms for density. Case: Type II burst, Table (5.8). a) Laminar regime, b) Turbulent regime. | 111 |
| 6.17 | Histograms for solar wind velocity V_{sw} . Case: Type II burst, Table (5.8). a) Laminar regime, b) Turbulent regime. | 111 |
| 6.18 | Model ICME speed versus distance. Case: Type II burst, a) Laminar regime, b) Turbulent regime. | 112 |
| 6.19 | This figure shows the time-travel covered by the ICME as a function of its velocity comparing our results for different ν and C_d values with respect to empirical models (GOPALSWAMY et al., 2000; GOPALSWAMY et al., 2001). | 113 |

| | | |
|------|---|-----|
| 6.20 | ICME speed versus distance for the four models analyzed in this work. a) laminar regime considering variability in ICME radius (Eq. 4.9) and $\mu = 0.175 \text{ g/cm} \cdot \text{s}$ (dashed line). b) turbulent regime considering variability in ICME radius (Eq. 4.10) and $C_d = 5 \times 10^4$ (dot-dashed line). c) laminar regime considering variability in ICME radius and SW density (Eq. 4.16) and $\nu = 8.75 \times 10^{20} \text{ cm}^2/\text{s}$ (continuous line). and d) turbulent regime considering variability in ICME radius and SW density (Eq. 4.13) and $C_d = 1.1 \times 10^5$ (dot line). | 115 |
| B.1 | Kolmogorov-Smirnov statistics D. A measured distribution of values in x (shown as N dots on the lower abscissa) is to be compared with a theoretical distribution whose cumulative probability distribution is plotted as P_x . A step-function cumulative probability distribution $S_N(x)$ is constructed, on each rise an equal amount at each measured point. D is the greatest distance between the two cumulative distributions. | 129 |
| C.1 | Idealized sketch of a complete radio event. | 133 |

LIST OF TABLES

| | <u>Pág.</u> |
|---|-------------|
| 4.1 Variation of parameters - turbulent regime | 68 |
| 4.2 Variation of parameters - laminar regime | 68 |
| 4.3 Variation of parameters (% 10) - turbulent regime | 68 |
| 4.4 Variation of parameters (% 10) - laminar regime | 69 |
| 4.5 Values of the computed final speed (in km/s) at 1 AU for an initial CME speed of 1000 km/s for the maximum, fixed and minimum values of each parameter, Table (4.1), and minimum and maximum percentage of variations values of speeds at 1 AU with respect of the fixed values, turbulent regime [(*) value out of range]. | 71 |
| 4.6 Values of the computed final speed (in km/s) at 1 AU for an initial CME speed of 1000 km/s for the maximum, fixed and minimum values of each parameter, Table (4.3), and minimum and maximum percentage of variations values of speed at 1 AU with respect to the fixed values, turbulent regime [(*) value out of range]. | 71 |
| 4.7 Values of the computed final speed (in km/s) at 1 AU for an initial CME speed of 1000 km/s for the maximum, fixed and minimum values of each parameter, Table (4.2), and minimum and maximum percentage of variation values of speed at 1 AU with respect to the fixed values, laminar regime [(*) value out of range]. | 75 |
| 4.8 Values of the computed final speed (in km/s) at 1 AU for an initial CME speed of 1000 km/s obtained for the maximum, fixed and minimum values of each parameters, Table (4.2), and minimum and maximum percentage of variation values of speed at 1 AU with respect to the fixed values, laminar regime [(*) value out of range]. | 75 |
| 5.1 CME and ICME events observed [(*) values not measured]. | 82 |
| 5.2 CME and ICME events observed at distances lower than 1 AU [(*) values not measured]. | 85 |
| 5.3 Calculated transit time, speed and parameters for ICMEs events at 1 AU. | 85 |
| 5.4 Calculated and observed transit time and speed for ICMEs events at 1 AU for laminar (first line for each number) and turbulent regime (second line for each number). | 87 |

| | | |
|-----|---|----|
| 5.5 | Calculated distance, transit time, speed and parameters for ICMEs events at distances lower than 1 AU. | 89 |
| 5.6 | Calculated and observed distance, transit time, and speed for ICMEs events at distance lower than 1 AU for laminar (first line for each number) and turbulent regime (second line for each number). | 90 |
| 5.7 | Type II burts events. | 91 |
| 5.8 | Calculated transit time, speed and parameters for Type II burst events. . | 93 |
| 5.9 | Calculated and observed transit time, speed for Type II bursts events for laminar (first line for each number) and turbulent regime (second line for each number). | 94 |

1 INTRODUCTION

The Sun is the nearest star. It is located in an outer part of one arm of the Milky way galaxy. Our planet, the Earth, among the other planets of the solar system is bounded in a closed orbit around it. When we study the Sun-Earth connection, it is common to introduce the term space weather, which refers to the conditions on the Sun, in the interplanetary medium, the solar wind, magnetosphere, ionosphere and thermosphere. These conditions, in principle, affect the performance of space and ground based technological systems and may have effects in the human life ([SCHWENN, 2006](#)). The modern technology is more vulnerable to the disturbances from the space environment specially to the explosive events on the Sun. This fact has been studied since the launch of the first satellites to the space ([LANZEROTTI, 2007](#)).

Different phenomena related to the Sun's activity can disturb the Earth's environment: solar flares, which release energetic particles and ionizing radiation; the variable solar wind; coronal mass ejections (CMEs); corotating interaction regions (CIRs); shocks; interplanetary remnants of CMEs, called ICMEs, among others. When these events arrive at the Earth's magnetosphere, they may cause geomagnetic storms. The transference of energy from the solar wind to the magnetosphere during magnetic storms is strongly related to the presence of southward component of the magnetic field that is carried out by the structures in the solar wind ([GONZALEZ; TSURUTANI; GONZALEZ, 1999](#); [ECHER et al., 2005](#)). CMEs together with solar flares are one of the main interplanetary events. They can drive shocks and are responsible for the strongest geomagnetic storms.

Another interesting characteristic in Sun-Earth relation is the well known solar cycle. The rise and fall of the number of sunspots on the Sun surface has been known since the mid-19th century. This solar cycle goes from a minimum number of sunspots (a solar minimum) to when the Sun has a maximum number of sunspots (a solar maximum) and goes back to a minimum. The interval between two minima is about 10.5 to 11 years ([EDDY, 1976](#)). Solar activity is related to the solar cycle, and this activity (such as coronal mass ejections and flares) is more frequent at solar maximum and less frequent at solar minimum, consequently geomagnetic activity also follows the solar cycle.

1.1 Coronal and Interplanetary Mass Ejections

Coronal mass ejections (CMEs) and the counterpart in the interplanetary medium (ICMEs), are one of the major forms of solar activity that inject mass and energy into the interplanetary space. They have their origin in the low corona, below 1 solar radius (R_{\odot}), where the plasma density is approximately 10^9 part/cm^3 and the temperature reaches values of the order of 10^6 K . On average CMEs have a mass of 10^{16} g (GOSLING, 2000) and cover a wide range of initial speeds, from $\sim 100 \text{ km/s}$ to $\sim 3000 \text{ km/s}$ (CYR et al., 1999). This region, between $30 R_{\odot}$ and $215 R_{\odot}$, is more tenuous compared to the solar corona; the density decreases as a function of the radial position as $1/x^2$ (LEBLANC; DULK; BOUGERET, 1996), where x is the position measured from the Sun.

Due to the interaction with the solar wind, fast ICMEs ($V_{cme} > 400 \text{ km/s}$) undergoes a deceleration process that takes place in the interplanetary medium. On the other hand, slow ICMEs ($V_{cme} < 400 \text{ km/s}$) are accelerated, increasing their speed from its initial value up to the ambient SW velocity ($\sim 400 \text{ km/s}$) (GOPALSWAMY et al., 2000; GOPALSWAMY et al., 2001). This process of acceleration or deceleration occurs in the ICME travel throughout the interplanetary medium.

CMEs are observed in the solar corona generally with coronagraphs in white light. Figure (1.1) shows an example of CME observation from the Large Angle Spectrometric Coronagraph (LASCO) on board the SOHO spacecraft (BRUECKNER et al., 1995). With this kind of instruments it is possible to obtain speed and acceleration profiles, since the first detection in the low solar atmosphere up to several solar radius in the interplanetary space.

It is also possible the observation in the ultraviolet spectrum, since these structures disturb the solar corona producing waves (EIT waves, for example) and dark regions in the solar corona, as a consequence of the propagation of these waves. Figure (1.2) is an example of this kind of observation. These perturbations are described as moving brilliant arcs with a dark region behind, that radially moves away from the origin of the perturbation. The velocity of propagation of these structures is in the range of 200 km/s to 600 km/s (DELANNÉE, 2000; WANG, 2000).

In the interplanetary space, observations done by the Advance Composition Explorer satellite (ACE), for example, (MCCOMAS et al., 1998; STONE et al., 1998) at 1 AU, give

records of velocity, density, temperature and magnetic field components of intensity of the solar wind and the ICMEs.

In the case of ICMEs associated with interplanetary shocks (CANE; SHEELEY; HOWARD, 1987), some of these shocks produce Type II radio emissions at the local plasma frequency and its first harmonic, $f_p(KHz) = 9 \cdot \sqrt{\rho(cm^{-3})}$, where f_p is the plasma frequency and ρ is the plasma (medium) density. These emissions are indicative of shock propagation in the solar corona and in the inner heliosphere. Due to its electromagnetic nature, these emissions arrive at the Earth in 8 minutes, and may be a warning signal that a perturbation is coming to the magnetosphere (GOPALSWAMY et al., 2005). The Type II data is presented as graphics of the emission intensity as function of frequency and time t . The frequency f_p may be seen as the emission region; due to the fact that the density in the interplanetary medium falls as $1/x^2$ (LEBLANC; DULK; BOUGERET, 1996), and in consequence this gives the place of the shock.

Another form to obtain information of the propagation of ICMEs is through the interplanetary scintillation (IPS) technique, where fast variations in the intensity of a radio signal are detected due to density inhomogeneities. When an ICME disturbs the medium, it is possible to detect fast variations in the intensity of the scintillation, in temporal scales of minutes to hours. These measurements give information about the velocity of the solar wind in the front of the structure. In this way, it offers a diagnostic about acceleration or deceleration of the ICMEs (MANOHARAN, 2006).

1.1.1 Geoeffectiveness of CMEs-ICMEs

The geoeffectiveness (i.e., the degree of disturbance in the Earth magnetosphere) of ICMEs depends on its speed, the strength and direction of the magnetic field, as well as the dynamic pressure (GONZALEZ; TSURUTANI; GONZALEZ, 1999; GONZALEZ; ECHER, 2005; ECHER et al., 2005). When a ICME arrives at 1 AU, it interacts with the magnetosphere and, if the component of the magnetic field of this structure is appropriated (south component), it will be possible to transfer energy from the ICME to the magnetosphere by the mechanism of magnetic reconnection (DUNGEY, 1961). Therefore, these parameters are important for space weather and magnetospheric physics. In terms of space weather prediction, a very important parameter

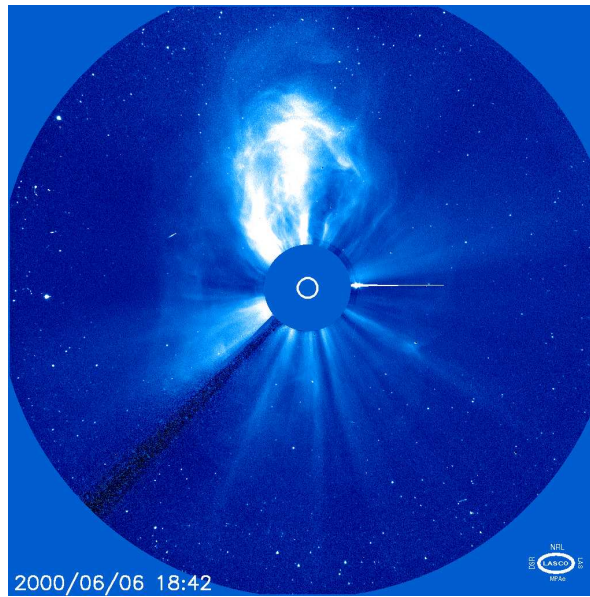


FIGURE 1.1 - CME observed by LASCO (C2), date: 6 June of 2000, 18:42 UT.

SOURCE: <http://sohowww.nascom.nasa.gov/data/realtime/c3/512/>

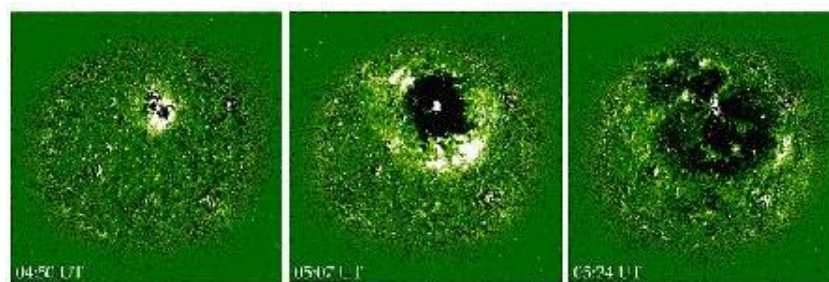


FIGURE 1.2 - Sequence of images in Fe XII (19.5 nm), with the method of running difference images. It is easy to see the dimming region in black. Event May 12 of 1997.

SOURCE: Borgazzi (2003)

is the ICME arrival time, or, in other words, the Sun-Earth ICME travel time. This travel time depends on the CME initial speed and on the ICME - solar wind (SW) interaction; (see (CARGILL, 2004) and references therein).

1.2 Transport models

In the description of the dynamic behavior of CMEs and ICMEs many attempts have been done to quantify the interaction with the solar wind. Different kinds of models have been proposed: theoretical, empirical and numerical simulations. As the aim of the present work is the study of the dynamics of the ICMEs in the interplanetary medium, it is presented in this section a brief outline of the models that have been proposed to explain the behavior of these structures in their propagation through the interplanetary space.

1.2.1 Theoretical models

A theoretical description of the interaction between ICMEs and the solar wind is, for example given by Canto et al. (2005). In that work is presented an analytic model for the evolution of a supersonic fluctuation that propagates in the ambient solar wind and is injected at the base of the corona to the interplanetary space. Canto et al. (2005) used kinematic considerations for this description. This perturbation results in the formation of a density and speed discontinuity in the ambient solar wind, named ‘working surface’. This working surface travels in the interplanetary medium and the initial parameters that characterized this structure, i.e., the speed and density jumps during the initial fluctuation. Assuming that this working surface can be related to an ICME, the authors described the evolution of the ICME and gave insight in some important parameters like: the velocity and the arrival time (travel time) at 1 AU.

1.2.2 Empirical models

The majority of empirical models are developed to forecast the arrival time and speed, at 1 AU, of ICMEs (GOPALSWAMY et al., 2000; GOPALSWAMY et al., 2001; GOPALSWAMY et al., 2005). Using observations of the initial CME speed, and ICME speeds in the interplanetary medium, the methodology used in these works consists in the establishment of relationships between the observed data, i.e., the measured velocities and the acceleration acting on the ICMEs. In the same branch are the works of Vrsnak (2002), Vrsnak et al. (2004), Vrsnak and Zic (2007). In the last case, the study contemplated these relations from the point of view of viscous forces acting on the ICME. There are other models which try to establish empirical relationships between observations at the Sun and parameters of importance in the vicinity of the

Earth, as the arriving time and velocity at 1 AU (DALLAGO et al., 2004; HOWARD et al., 2007; LINDSAY et al., 1999; SCHWENN; LAGO; GONZALEZ, 2005; WEBB et al., 2000b; WEBB et al., 2000a).

1.2.3 Numerical Simulations

In this group we can mention the works of Vandas et al. (1995), Cargill and Chen (1996), Odstrcil and Pizzo (1999a), Gonzalez-Esparza et al. (2003), Cargill (2004), Odstrcil and Pizzo (1999b) among others. These works generally confront the study of the evolution of some properties (temperature, density, speed) of the agent, (i.e. the ICMEs), in different forms (plasmoids, magnetic clouds) through their travel in the interplanetary space, from the point of view of the hydrodynamics (HD) or magnetohydrodynamic (MHD).

1.3 Scope of the present work

In view of the scenery presented and in order to have a better understanding of the ICME behavior from a theoretical point of view, this work approaches the study of the ICMEs dynamics using the hydrodynamics theory. The ICME - SW system is considered as two interacting fluids under the action of viscous forces, without taking into account microscopic details of this special case of interaction for low density plasmas.

The aim of the present thesis is the obtaining of analytic solutions that may describe the momentum transfer between the ICME and the solar wind. From a point of view of an energetic balance, we consider the kinematic and magnetic energies involved in transport process in the interplanetary medium. The kinematic energy variation (ΔE_k) for a typical ICME traveling between $30 R_\odot$ and $215 R_\odot$ is:

$$\Delta E_k = -2.6 \times 10^{24} \text{Joules.} \quad (1.1)$$

Whereas the variation of magnetic energy (ΔE_{mag}) in the same interval of distance is:

$$\Delta E_{mag} = -1.14 \times 10^{22} \text{Joules.} \quad (1.2)$$

Therefore the kinematic energy is two orders of magnitude higher than the magnetic energy involved in the process (see Appendix A for more details). For this reason we do not take into account the magnetic interactions in this first approach. In other

words, we do not consider an explicit term for the magnetic field in the transport equations.

This thesis is divided in two parts: the first is related principally with the development of the hydrodynamic model (chapter 2, 3, and 4) and the second part presents the validation of this model with observed data, in situ and remote (chapter 5). Finally the results and conclusions are presented in chapter 6 and 7.

2 CORONAL AND INTERPLANETARY MASS EJECTIONS

In this chapter we briefly present the most important models that describe the first stage of the CME, i.e., the models that describe the behavior in the low solar atmosphere of coronal mass ejections where the conditions are: large magnetic fields and high density plasma. The second stage considers ICMEs, i.e., the interplanetary coronal mass ejections and their behavior in the interplanetary space where the magnetic field magnitude and the plasma density are not as high as in the low solar atmosphere.

2.1 Coronal Mass Ejections (CMEs)

CMEs and ICMEs are, up to now, poorly understood structures. Ideally, the observation of CMEs and the first stages of ICMEs would take place in the innermost heliosphere, at a distance of few solar radii. The observations of these structures are remote (e.g., LASCO, SOHO, STEREO ([KAISER, 2005](#))) and in situ, the latter mainly at the vicinity of Earth, (at 1 AU), plus some observations at other heliocentric distances (e.g., Helios, Ulysses, Voyager, or Pioneer).

The dynamo activity in the solar interior creates the magnetic field which builds up the topological structure of the corona. Sometimes these fields erupt as a result of an instability or loss-equilibrium process, which is not identified yet. However, when a CME is underway, several additional processes are triggered, including magnetic reconnection, shock formation and particle acceleration. The main objective of this section is to give a brief view of the various physical process involved in the life cycle of CMEs.

In general, numerical or analytical models require specific initial state of the system. In the case of a MHD model, eight variables must be known prior to the CME onset: three components of the magnetic field, three components of the velocity, the density and temperature throughout the heliosphere. Among these variables, the most critical is the magnetic field, because only the magnetic field associated with the coronal currents is available. Unfortunately, this magnetic field is very difficult to measure. The more accurate way to estimate this field, up to now, is based on extrapolations of the vector fields at photospheric and chromospheric levels. For this reason, it is necessary to make an educated guess for the pre-eruptive field and then, evolve it in a way consistent with the observed surface field to see if it leads to a

CME-like eruption. In recent years many efforts have been done using numerical methods to solve the problem, as examples we have the works of Mikic, Barnes and Schnack (1988); Biskamp and Welter (1989); Chen, Shibata and Yokoyama (2001); Odstreil et al. (2002); Linker et al. (2003); Kusano et al. (2004). These models must cope with an enormous range of spatial and temporal scales involved in the CME phenomenon (FORBES et al., 2006). An additional problem exists for models of CME initiation: the physical mechanism that triggers the CMEs is still unknown. The analytical models cannot cope with the same level of complexity as numerical models. In the case of analytical models, they provide a deeper level of insight into the underlying physics, and they are often associated with numerical models to give a better understanding of the CME ignition.

In the past, the early models of CMEs, were based on principles different from the ones used nowadays. As an example, we mention the models that assumed that a CME is the result of a flare-generated blast wave. As we know today, only some CMEs are associated with a flare. In many cases, there is not a flare association, or the CME can precede the flare (WAGNER et al., 1981; HARRISON, 1986). When the CMEs are very slow (< 150 km/s) they undergo a weak acceleration over a period of approximately a day (SRIVASTAVA et al., 1971; ZHANG; HOWARD; VOURDILAS, 2004). For this class of CMEs, the observed flux emergence in the photosphere is of the same order as the one required by the flux injection model (KRALL; CHEN; SANTORO, 2000).

The major problem that the so called storage models have is to explain how it is possible to decrease the magnetic energy in the corona even through the ejection of the CME stretches the magnetic field as it moves outwards into the interplanetary space. The stretching of the magnetic field implies that the magnetic energy of the system is increasing, whereas models require it to decrease.

There are several models that describe the CME initiation: the flux rope model and flux cancellations (KUPERUS; RAADU, 1974); the breakout model (ANTIOCHOS; DEVORE; KLIMCHUK, 1999; DEVORE; ANTIOCHOS, 2005); and the flux injection model (CHEN, 1989).

2.1.1 Flux rope model and flux cancellation

Generally, the coronal mass ejections are associated with solar flares and prominence eruptions. The prominences are structures of the chromosphere with temperature $T \approx 10^4$ K and density $\rho \approx 10^{10} - 10^{11} \text{ part/cm}^{-3}$, surrounded by the tenuous corona. The magnetic field of these structures present ‘inverse polarity’, i.e., when the coronal magnetic field embedded in the prominence cross a neutral line, it points out in the opposite direction compared with the photospheric magnetic field polarity (LEROY; BOMMIER; SAHAL-BRECHOT, 1983). The idea that a flux rope explains the inverse polarity of a prominence was postulated first by Kuperus and Raadu (1974).

There are two possibilities about the formation of the flux rope: a) the flux rope emerges from below the photosphere (RUST; KUMAR, 1994; LITES et al., 1995), b) the flux rope is the result of the motion of material in the photosphere (FORBES et al., 2006).

In the first case, the flux rope could emerge from below the photosphere, or be formed as the result of motions at the photosphere or above. This process occurs as a result of the flux cancellation at the surface (the photosphere). Martin, Livi and Wang (1985) define flux cancellation as the mutual disappearance of magnetic fields of opposite polarity at the neutral line separating them. This term must be taken carefully. It is not a theoretical interpretation of the physical process; it must be interpreted as the flux elements being submerged, annihilated, or being expelled upward.

Observations show that at the time of the flux cancellation the filaments are frequently observed to form along the neutral line; after that they may disappear, presumably due to eruption and may be reformed in the same location later on. Associations of flux cancellation with solar flares have been observed (LIVI et al., 1989), and recently this phenomenon was associated with CMEs (LIN; RAYMOND; BALLEGOOIJEN, 2004). In all of these cases the flux cancellation is related to the annihilation of magnetic flux at the photosphere through reconnection.

2.1.2 The breakout model

The breakout model agrees with two properties of CMEs and eruptive flares that have proved to be very difficult to explain with previous models: (1) very low-lying magnetic field lines, down to the photospheric neutral line, that can open toward

infinity during an eruption; (2) the eruption is driven by the magnetic free energy stored in a closed, sheared arcade (ANTIOCHOS; DEVORE; KLIMCHUK, 1999). The feature of this model is that the CMEs occur in multipolar topologies in which reconnection between a sheared arcade and the neighboring flux systems triggers the eruption. In this ‘magnetic breakout’ model, the reconnection removes the unsheared field above the low-lying, sheared core flux near the neutral line, thereby allowing this core flux to open.

2.1.3 Flux injection model

According to Chen (1989), three-dimensional magnetic flux rope is the underlying magnetic field of a CME. The model assumes that this structure is in MHD equilibrium, and the eruption occurs in response to the ‘injection’ of poloidal magnetic flux into the flux rope. Then the model uses an approximated form of the MHD equation to calculate the evolution of the flux rope. Since the launch of SOHO, this model has been tested against EIT and LASCO data.

The direct comparison with data has shown that the model closely match with the observed height-profiles of CMEs within LASCO field of view (CHEN, 1997; WOOD et al., 1999; KRALL; CHEN; SANTORO, 2000). In addition, synthetic coronagraph images (CHEN et al., 2000) show that the 2-D projections of 3-D flux ropes exhibit the generic morphological features of the classic three parts of the CME, i.e., leading-edge, cavity and filament (ILLING; HUNDHAUSEN, 1986); and it was found too that the CME model evolves into the interplanetary medium as a resembling magnetic clouds observed at 1 AU (CHEN, 1996). These studies of flux ropes show that the hypothesis of the three part structure is quantitatively consistent with the observed CMEs.

2.2 Interplanetary coronal mass ejections (ICMEs)

After the eruption of the CME in the low solar corona, the ejecta propagates along the solar atmosphere and in the interplanetary medium. To describe the process of propagation in the interplanetary medium, it is possible to give three approaches: analytical formulation, numerical simulations and empirical descriptions. The analytical approach in this work describes the problem with the equations of motion of the structure in the medium, taking into account the variability of the solar wind.

The ICME is subjected to deformation forces and can be accelerated or decelerated

depending on the forces acting on it. By solving the equations of motion, we determine the position of the ICME and its geometry as a function of time. On the other hand, the MHD simulations, give the motion field and the force field acting on the ICME in every point of a simulation grid.

In the analytical approach, unlike simulation, the ICME is treated as an object that is explicitly interacting with forces that propel, expand, deform, and accelerate or decelerate it. In particular it is possible to study the drag force that couples it to the solar wind, and use the ‘virtual mass’, a concept based on the hydrodynamic theory, that allows one to express, by an appropriate increase in the mass of the body, the force needed to move the ambient medium out of the way as the body moves.

The relevant observations for the CME - ICME description are: the initial acceleration of the CME near the Sun, the acceleration or deceleration between the Sun and Earth, the rate of expansion of the ICME, the shape and cross section of the ICME, and the value of the magnetic field, density and temperature within the structure at 1 AU. According to Zhang (2005), after a statistical analysis of 24 CMEs, typical values for the acceleration and duration of this stage are 200 m/s^2 and 4 min, respectively. This information gives $0.82 R_{\odot}$ as a typical acceleration distance. In an analysis made by Gopalswamy et al. (2000) using 28 CMEs it was found that the speeds near the Sun are in the range of 124 km/s to 1056 km/s. In other cases, speeds higher than 1000 km/s have been observed (GOPALSWAMY,).

All these parameters are very important since they act as initial conditions when the CME goes from the Sun atmosphere to the interplanetary medium, approximately at $30 R_{\odot}$ (BORGAZZI et al., 2009). An important parameter is the size and expansion speed of ICMEs. The radial dimension of the ICME at 1 AU varies between 0.2 and 0.25 AU (DALLAGO et al., 2004; KLEIN; BURLAGA, 1982; HU; SONNERUP, 2002). Studying the radial speed expansion, in an analysis of 37 ICMEs, Owens et al. (2005) found an empirical relation between the rate by which a ICME radius increases (V_{EXP}) and the speed of the leading edge of the ICME (V_{LE}), this is:

$$V_{EXP}[km/s] = 0.266V_{LE}[km/s] - 70.61. \quad (2.1)$$

Another important parameter is the cross-sectional shape of an ICME. The cross section at the Sun, as seen by coronagraphs, is roughly circular, but at 1 AU the expectation to have the same geometry is practically zero. In the interplanetary

medium, forces acting on the ICMEs in the same direction of the motion are different than those acting in the perpendicular direction. Because of that, it is useful to consider an elliptical cross section as a first-order departure from circularity. Indirect methods suggest that the ratio of the major to minor axes of the cross section of an ICME at 1 AU is typically less than 2 (HU; SONNERUP, 2002); other analyses found typical values closer to 4 (MULLIGAN; RUSSELL, 2001). This quantity, the ratio of major to the minor ICME axes is very important in analytical models because it helps to compare the values of the magnetic field strength and mass density within the ICME at 1 AU. According to Lepping et al. (2003), and based on the study of 19 ICMEs, the magnetic field has a strength of approximately 13 nT and the proton number density is 11 *protons/cm*³.

The paradigm of the initial stage of the ICME establishes basically, the main idea that a coronal magnetic flux rope is anchored in the solar atmosphere and is in force-balance equilibrium. It can be destabilized by adding sufficient magnetic flux, circulating around the central axis of the flux rope. Once the flux rope is destabilized, it expands in cross section and moves away from the Sun (CHEN, 1996; CHEN, 1997). Under excess of external pressure (dynamic plus magnetic), pushing up on its lower surface over that pushing down on its upper surface, the flux tube accelerates away from the Sun against the force of gravity and the aerodynamics drag. In other words, as stated by Forbes et al. (2006) the equations that describes the expansion and propagation of the flux tube are :

Expansion:

‘(Ambient Mass Density)×(Rate of expansion)² = Pressure Inside - Pressure Outside’.

Acceleration:

‘(Mass of CME + Virtual Mass) × Acceleration = Force of Gravity + Outside Magnetic & Particle Pressure on Lower Area - Same on Upper Surface Area - Drag term’.

These two equations are coupled since the ‘Pressure Outside’ term in the first equation changes as the flux tube moves through the ambient medium as governed by the second equation, and the bottom-to-top pressure differences that propel the CME in the second equation are determined by the expansion of the flux tube as governed by the first equation.

3 HYDRODYNAMICS THEORY

In this chapter, we briefly develop the basic concepts of the hydrodynamics theory which are necessary to describe the interaction model of the ICME with the surrounding medium, through the action of two kind of drag forces, ‘laminar’ and ‘turbulent’.

3.1 Strain state of a body

When a body is immersed in a fluid it experiences forces that can produce deformations. One of the aspects of the study of the fluid dynamics involves the determination of these forces acting on the body. In the case of a fluid, the state of deformation is similar to the solid body and is classified as normal strain, defined as the change in length per unit length of a linear element. The shear strain is defined as the rate of decrease of the angle formed by two mutually perpendicular lines on the element. The basic difference with the solid is that it is defined strain rates in a fluid because it continues to deform.

3.1.1 Linear or normal strain rate of a fluid

Consider a fluid element moving in the \mathbf{x}_1 direction, as illustrated in Figure (3.1). The rate of change of length per unit length is defined as:

$$\frac{1}{\delta x_1} \frac{D}{Dt}(\delta x_1) = \frac{1}{dt} \frac{A'B' - AB}{AB}, \quad (3.1)$$

this is (see Figure (3.1)):

$$\frac{1}{\delta x_1} \frac{D}{Dt}(\delta x_1) = \frac{1}{dt} \frac{1}{\delta x_1} \left[\delta x_1 + \frac{\partial u_1}{\partial x_1} \delta x_1 dt - \delta x_1 \right] = \frac{\partial u_1}{\partial x_1}, \quad (3.2)$$

where \overline{AB} is the initial length of the fluid element and $\overline{A'B'}$ is the length of the fluid element after the elongation (KUNDU; COHEN, 2004).

In Equation (3.1) $D/Dt = \frac{\partial}{\partial t} + \mathbf{u} \cdot \nabla$. In a general way, we must define a linear strain rate in the δ direction as $\partial u_\delta / \partial x_\delta$. If we sum the linear strain rates in the three orthogonal directions we obtain the rate of change of volume per unit volume, called the volumetric strain rate or the bulk strain rate. For this analysis, it is

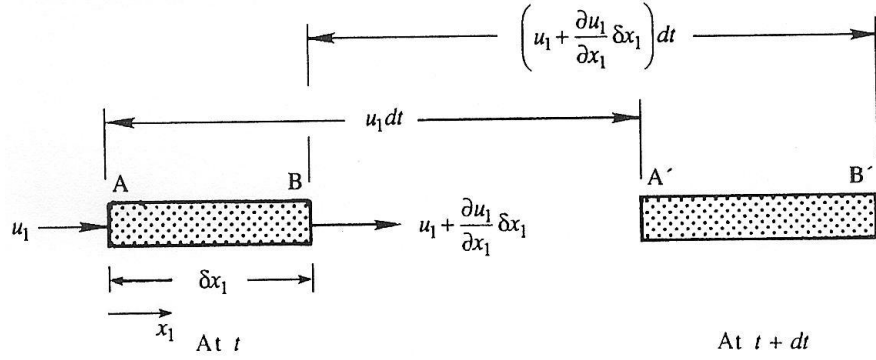


FIGURE 3.1 - Illustration of the linear strain rate in a fluid.

SOURCE: Kundu; Cohen (2004)

considered a fluid element of sides $\delta x_1, \delta x_2, \delta x_3$, where the volume δV is defined as $\delta V = \delta x_1 \delta x_2 \delta x_3$, and the volumetric strain rate is given by:

$$\begin{aligned} \frac{1}{\delta V} \frac{D(\delta V)}{Dt} &= \frac{1}{\delta x_1 \delta x_2 \delta x_3} \frac{D}{Dt} (\delta x_1 \delta x_2 \delta x_3), \\ &= \frac{1}{\delta x_1} \frac{D}{Dt} (\delta x_1) + \frac{1}{\delta x_2} \frac{D}{Dt} (\delta x_2) + \frac{1}{\delta x_3} \frac{D}{Dt} (\delta x_3). \end{aligned} \quad (3.3)$$

Then after some algebraic steps,

$$\frac{1}{\delta V} \frac{D}{Dt} (\delta V) = \frac{\partial u_1}{\partial x_1} + \frac{\partial u_2}{\partial x_2} + \frac{\partial u_3}{\partial x_3} = \frac{\partial u_i}{\partial x_i}. \quad (3.4)$$

3.1.2 Shear strain rate of a fluid

A fluid can also deform in shape. This kind of deformation can be defined as the rate of decrease of the angle formed by two mutually perpendicular lines on the element under deformation. Figure (3.2) shows the deformation under the shear strain. The rate of shear is given by (KUNDU; COHEN, 2004):

$$\begin{aligned}\frac{d\alpha + d\beta}{dt} &= \frac{1}{dt} \left[\frac{1}{\delta x_2} \left(\frac{\partial u_1}{\partial x_2} \delta x_2 dt \right) + \frac{1}{\delta x_1} \left(\frac{\partial u_2}{\partial x_1} \delta x_1 dt \right) \right] \\ &= \frac{\partial u_1}{\partial x_2} + \frac{\partial u_2}{\partial x_1},\end{aligned}\tag{3.5}$$

where α and β are the deformation angles.

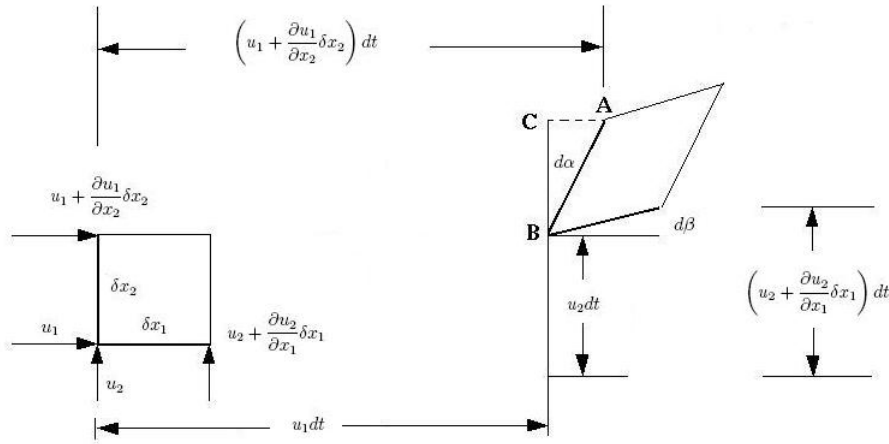


FIGURE 3.2 - Illustration of shear strain rate in a fluid.

SOURCE: Adapted from: Kundu; Cohen (2004)

Finally, it is possible to describe the total deformation of a fluid element using the strain rate tensor

$$e_{ij} = \frac{1}{2} \left(\frac{\partial u_i}{\partial x_j} + \frac{\partial u_j}{\partial x_i} \right),\tag{3.6}$$

where the diagonal terms of the matrix e are the normal strain and the off-diagonal terms are the shear strain.

3.2 Vorticity

A fluid element can rotate, and for this reason the fluid lines rotate by different amounts. To express this fact, the vorticity of the element around \mathbf{x}_3 is defined as

$$\omega_3 = \frac{1}{dt} \left[\frac{1}{\delta x_2} \left(-\frac{\partial u_1}{\partial x_2} \delta x_2 dt \right) + \frac{1}{\delta x_1} \left(\frac{\partial u_2}{\partial x_1} \delta x_1 dt \right) \right]. \quad (3.7)$$

We can relate this definition of vorticity component to the velocity vector using $\omega = \nabla \times \mathbf{u}$. When a fluid is irrotational, it means that $\omega = 0$, and the velocity vector can be written as the gradient of a scalar function $\phi(\mathbf{x}, t)$, as $u_i \equiv \frac{\partial \phi}{\partial x_i}$.

3.3 Conservation laws

In this section we briefly describe the basic equations of conservation in hydrodynamic fluids.

3.3.1 Control-volume formulations

To study the flow of mass, momentum, energy passing through a finite region, it is common to use the control-volume approach ([WHITE, 1986](#)). Let us consider the finite volume delimited for the streamlines and the two surfaces shown in continuous and dot lines of Figure (3.3).

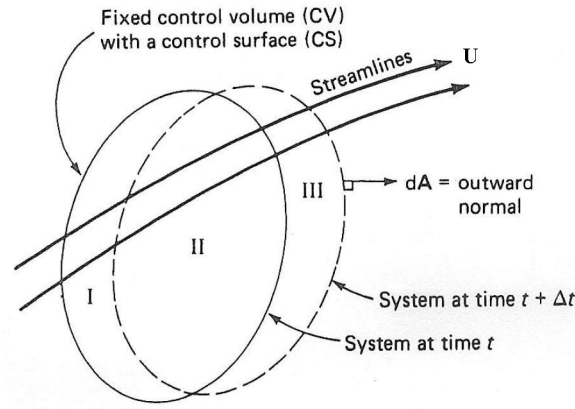


FIGURE 3.3 - Control volume.

SOURCE: Kundu; Cohen ([2004](#))

Consider that at an instant t , the region shown in Figure (3.3) is filled by the fluid, passing through the volume that is limited by the two surfaces (I and III). The purpose is to calculate the rate of change of the quantity dQ/dt (Q representing

mass, energy or momentum) when it passes through the control volume. For this, it is necessary to calculate a limit process passes, and the rate of change is given by :

$$\begin{aligned}\frac{dQ}{dt} &= \lim_{\Delta t \rightarrow 0} \frac{(Q_{II} + \Delta Q_{III})_{t+\Delta t} - (\Delta Q_I + Q_{II})_t}{\Delta t} \\ &= \lim_{\Delta t \rightarrow 0} \left[\frac{(Q_{II})_{t+\Delta t} - (Q_{II})_t}{\Delta t} + \frac{\Delta Q_{III}}{\Delta t} - \frac{\Delta Q_I}{\Delta t} \right].\end{aligned}\quad (3.8)$$

The region II is the control volume, and the first term in Equation (3.8) is the rate of change of Q within the control volume given by:

$$\lim_{\Delta t \rightarrow 0} \frac{(Q_{II})_{t+\Delta t} - (Q_{II})_t}{\Delta t} = \frac{\partial}{\partial t} \iiint_{CV} \frac{dQ}{dm} \rho dV, \quad (3.9)$$

where dQ/dm is the intensive property per unit mass. The other two terms in Equation (3.8) are the influx and outflux of Q across the control surface:

$$\lim_{\Delta t \rightarrow 0} \frac{\Delta Q_{III}}{\Delta t} = \text{rate of outflux of } Q, \text{ and} \quad (3.10)$$

$$\lim_{\Delta t \rightarrow 0} \frac{\Delta Q_I}{\Delta t} = \text{rate of influx of } Q. \quad (3.11)$$

From Equations (3.10) and (3.11) we can write

$$\lim_{\Delta t \rightarrow 0} \left(\frac{\Delta Q_{III}}{\Delta t} - \frac{\Delta Q_I}{\Delta t} \right) = \iint_{CS} \frac{dQ}{dm} \rho \mathbf{u} \cdot d\mathbf{A}. \quad (3.12)$$

Finally we can define the instantaneous time rate of change of a property Q like

$$\frac{dQ}{dt} = \iint_{CS} \frac{dQ}{dm} \rho \mathbf{u} \cdot \mathbf{A} + \frac{\partial}{\partial t} \iiint_{CV} \frac{dQ}{dm} \rho dV. \quad (3.13)$$

3.3.2 Conservation of mass

If the property of interest is the mass, then from Equation (3.13) $dm/dm = 1$ and we have:

$$\frac{dm}{dt} = 0 = \iint_{CS} \rho \mathbf{u} \cdot d\mathbf{A} + \frac{\partial}{\partial t} \iiint_{CV} \rho dV, \quad (3.14)$$

or:

$$\int_V \frac{\partial \rho}{\partial t} dV = - \int_A \rho \mathbf{u} \cdot d\mathbf{A}. \quad (3.15)$$

Using the divergence theorem, Equation (3.15) becomes

$$\int_A \rho \mathbf{u} \cdot d\mathbf{A} = \int_V \nabla \cdot (\rho \mathbf{u}) dV. \quad (3.16)$$

Using Equation (3.16), Equation (3.15) can be rewritten as

$$\int_V \left[\frac{\partial \rho}{\partial t} + \nabla \cdot (\rho \mathbf{u}) \right] dV = 0. \quad (3.17)$$

Equation (3.17) holds for any volume, which means:

$$\frac{\partial \rho}{\partial t} + \nabla \cdot (\rho \mathbf{u}) = 0. \quad (3.18)$$

Equation (3.18) is called the continuity equation, and it can be rewritten as

$$\frac{1}{\rho} \frac{D\rho}{Dt} + \nabla \cdot \mathbf{u} = 0. \quad (3.19)$$

3.3.3 Conservation of linear momentum

When the property is the linear momentum $m\mathbf{U}$, we have $d(m\mathbf{U})/dm = \mathbf{U}$, and it is possible to calculate the total force \mathbf{F} on the system using Equation (3.13) as:

$$\mathbf{F} = \frac{d}{dt}(m\mathbf{U}) = \iint_{CS} \mathbf{U}(\rho\mathbf{U} \cdot d\mathbf{A}) + \frac{\partial}{\partial t} \iiint_{CV} \mathbf{U}\rho dV. \quad (3.20)$$

Equation (3.20) holds for an inertial control volume and it can be written as

$$\mathbf{F} = \mathbf{F}_{surface} + \mathbf{F}_{body} = \iint_{CS} \frac{d\mathbf{F}_s}{dA} ds + \iiint_{CV} \frac{d\mathbf{F}_b}{dm} \rho dV. \quad (3.21)$$

In Equation (3.21), we have different kinds of forces that act on the fluid element. The forces can be divided into three classes: body forces, surface forces and line forces. The former, the body forces, act at a distance, without physical contact. It means that exists a force field that could be gravitational, magnetic or electrostatic. The case of gravitational force, the equivalent to the acceleration, is the most common. The term of surface forces is related to the stress component, and divided into normal and tangential component. They are exerted by direct contact with the surface body. They are proportional to the area and are expressed per unit area. The last one, surface tension forces or line forces, are named like that because they act on a line, and their magnitude is proportional to the extent of the line.

3.4 Newton's law

The law of conservation of momentum, expressed by Equation (3.21), will be written now in differential form by applying Newton law to an infinitesimal element of fluid, as illustrated in Figure (3.4). If we apply the Newton law on the element represented in Figure (3.4), the net force on the element must be equal to the mass times the acceleration of the element. The sum of the surface forces in the \mathbf{x}_1 direction is equal to:

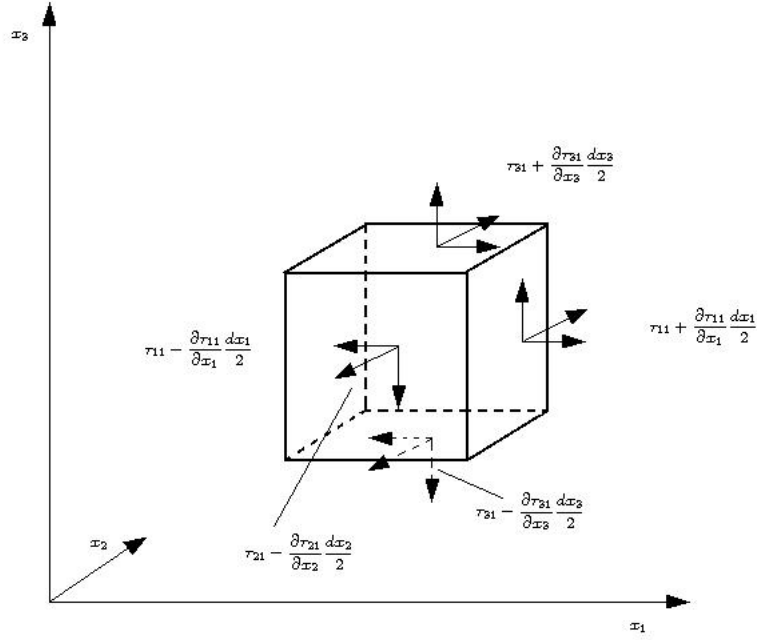


FIGURE 3.4 - Surface stress on a fluid element.

SOURCE: Adapted from: Kundu; Cohen (2004)

$$\begin{aligned}
 \sum F = & \left(\tau_{11} + \frac{\partial \tau_{11}}{\partial x_1} \frac{dx_1}{2} - \tau_{11} + \frac{\partial \tau_{11}}{\partial x_1} \frac{dx_1}{2} \right) dx_2 dx_3 + \\
 & \left(\tau_{21} + \frac{\partial \tau_{21}}{\partial x_2} \frac{dx_2}{2} - \tau_{21} + \frac{\partial \tau_{21}}{\partial x_2} \frac{dx_2}{2} \right) dx_1 dx_3 + \\
 & \left(\tau_{31} + \frac{\partial \tau_{31}}{\partial x_3} \frac{dx_3}{2} - \tau_{31} + \frac{\partial \tau_{31}}{\partial x_3} \frac{dx_3}{2} \right) dx_1 dx_2.
 \end{aligned} \tag{3.22}$$

If we consider \mathbf{g} the acceleration of gravity, so $\rho \mathbf{g}$ is the body force per unit volume, the Newton law is:

$$\rho \frac{Du_i}{Dt} = \rho g_i + \frac{\partial \tau_{ij}}{\partial x_j}. \tag{3.23}$$

This is the equation of motion for a volume element of the fluid. The stress tensor τ_{ij} is related to the deformation of the volume element and can be written for a

Newtonian incompressible fluid as:

$$\tau_{ij} = -p\delta_{ij} + 2\mu e_{ij}, \quad (3.24)$$

where e_{ij} is the strain rate tensor (Equation (3.6)) and μ is the viscosity of the fluid. This linear relation between τ and e is consistent with the Newton definition of viscosity coefficient in a parallel flow. All fluids that respond to this equation are called Newtonian fluids. The fluid property μ can depend only on the local thermodynamics state. The diagonal terms in Equation (3.24) correspond to the normal strain or pressure, and the nondiagonal terms are related to the shear strain on the body's surface.

Newton law for a material volume V requires that the rate of change of its momentum is equal to the sum of the body forces throughout the volume, plus the surface forces at the boundary:

$$\frac{D}{Dt} \int_V \rho u_i dV = \int_V \rho \frac{Du_i}{Dt} dV = \int_V \rho g_i dV + \int_A \tau_{ij} dA_j, \quad (3.25)$$

or:

$$\int \left[\rho \frac{Du_i}{Dt} - \rho g_i - \frac{\partial \tau_{ij}}{\partial x_j} \right] dV = 0. \quad (3.26)$$

Equation (3.26) holds for any volume, so we can write it as

$$\rho \frac{Du_i}{Dt} - \rho g_i - \frac{\partial \tau_{ij}}{\partial x_j} = 0. \quad (3.27)$$

3.5 Navier-Stokes equation

If we consider Equations (3.27), (3.6) and (3.24), we obtain the general equation for the behavior of a fluid or the Navier-Stokes equation:

$$\rho \frac{D\mathbf{u}}{Dt} = -\nabla p + \rho \mathbf{g} + \mu \nabla^2 \mathbf{u}. \quad (3.28)$$

3.6 Reynolds's number

The forces acting on a system of two immiscible liquids, like a drop of oil immersed in water, are due to the viscosity and the relative motion between the body and the fluid. In fluids dynamics the viscosity is a measure of the resistance to the shear or to the angular deformation, and is due to the momentum interchange between the components of the fluids (BACHELOR, 2000; KUNDU; COHEN, 2004). In this example, the drop has a representative linear dimension ‘ d ’ (diameter) and is in a steady translational motion with velocity ‘ U ’ in the medium. In this case, viscous forces are of order of $\mu U/d^2$, where μ is the viscosity of the medium. On the other hand, inertial forces in the fluid are of the order of $\rho U^2/d$, where ρ is the density of the medium. The ratio between these forces, viscosity and inertial, is given:

$$\frac{\rho d U}{\mu} = \Re, \quad (3.29)$$

defines the Reynold's number.

3.7 Derivation of Navier-Stokes equation for high and low Reynolds number

For a quantitative description of these forces we must take into account the equation of motion for incompressible fluids ($\nabla \cdot \mathbf{u} = 0$), and the Navier-Stokes equation. If we consider stationary conditions for the flow and neglect gravity effects, we can rewrite Equation (3.28) as

$$\rho \mathbf{u} \cdot \nabla \mathbf{u} = -\nabla p + \mu \nabla^2 \mathbf{u}. \quad (3.30)$$

In the case of high Reynolds number ($\Re \gg 1$) we assume that the viscosity is small, then the balance in the flow is between the pressure and the inertial forces (term in Equation (3.30), $\rho \mathbf{u} \cdot \nabla \mathbf{u}$). As the pressure changes are of order of ρU^2 , we can normalize Equation (3.30) using:

$$\mathbf{x}' = \frac{\mathbf{x}}{L}, \quad \mathbf{u}' = \frac{\mathbf{u}}{U}, \quad p' = \frac{p - p_\infty}{\rho U^2}, \quad (3.31)$$

and the Navier-Stokes equation takes the form:

$$\rho \mathbf{u}' \cdot \nabla \mathbf{u}' = -\nabla p' + \frac{1}{\Re} \nabla^2 \mathbf{u}'. \quad (3.32)$$

On the other hand, for low Reynolds number ($\Re \ll 1$), the pressure forces are of order of the viscous forces. In this case the new variables are:

$$\mathbf{x}' = \frac{\mathbf{x}}{L}, \quad \mathbf{u}' = \frac{\mathbf{u}}{U}, \quad p' = \frac{p - p_\infty}{\mu U / L}, \quad (3.33)$$

and the Navier-Stokes equation for low Reynolds number takes the form:

$$\Re \mathbf{u}' \cdot \nabla \mathbf{u}' = -\nabla p' + \nabla^2 \mathbf{u}'. \quad (3.34)$$

From these two Equations, (3.32), and (3.34), we can derive the expression for the force acting on a submersed body in a laminar regime (low Reynolds number) and in a turbulent regime (high Reynolds number). For the second case and to obtain the expression for the drag force, it is required to consider the conservation of momentum in the layer next to the body (laminar boundary layer), in a control volume next to the body. In this way we obtain an expression for the turbulent viscous force. In the first case of study, for low Reynolds numbers, it is necessary to know the stream function. Knowing that, it is possible to calculate the velocity and the stress tensor.

3.8 Derivation of laminar drag force

In the case of Equation (3.34) and in the limit of $\Re \rightarrow 0$ we can write the equation like:

$$\nabla p' = \nabla^2 \mathbf{u}'. \quad (3.35)$$

Using the condition that the velocity \mathbf{u} can be written as $\mathbf{u} = -\nabla \varphi \times \nabla \psi$, where φ and ψ are the potential and the stream functions for the fluid, respectively, we arrive at an equation for the stream function given by

$$\left[\frac{\partial^2}{\partial r^2} + \frac{\sin \theta}{r^2} \frac{\partial}{\partial \theta} \left(\frac{1}{\sin \theta} \frac{\partial}{\partial \theta} \right) \right]^2 \psi = 0. \quad (3.36)$$

With the proper boundary conditions, and considering spherical geometry for the

shape of the ICME, it is possible to arrive to a solution for the stream function of the form (KUNDU; COHEN, 2004),

$$\psi = Ur^2 \sin^2 \theta \left[\frac{1}{2} - \frac{3R}{4r} + \frac{R^3}{4r^3} \right]. \quad (3.37)$$

Using Equation (3.37) we can obtain the velocity components for a stream flow with a spherical body immersed in it, as:

$$u_r = U \cos \theta \left(1 - \frac{3R}{2r} + \frac{R^3}{2r^3} \right), \quad (3.38)$$

$$u_\theta = -U \sin \theta \left(1 - \frac{3R}{4r} - \frac{R^3}{4r^3} \right), \quad (3.39)$$

where R is the radius of the immersed body. In our model, R is the radius of the ICMEs. We can calculate the drag force component in the direction of the flow, as the surface integral of the total stress tensor τ_{ij} that acts on the body under study. For low Reynolds number we have:

$$F_i = \tau_{ij} n_j = -pn_i + \sigma_{ij} n_j, \quad (3.40)$$

where p is the normal component to the surface of the body, commonly known as pressure, and σ_{ij} is the stress tensor related to tangential stress for the body. The drag or Stokes force is obtained and the result is:

$$F_l = 6\pi\mu RU. \quad (3.41)$$

3.9 Derivation of turbulent drag force

3.9.1 Laminar boundary layers

When the Reynolds number (\Re) is large, the effects of viscosity become confined to a narrow region near the solid. Thus a thin boundary layer exists if the Reynolds number is in the range of $1000 < \Re < 10^6$, and in this case the boundary-layer flow is likely to be laminar. We can deduce an expression for the drag force using the flat-

plate integral analysis. We can obtain quantitative information about the boundary layer by doing an analysis of the flow of a viscous fluid, at high Reynolds number, passing a flat plate. In Figure (3.5), the edge of the plate is at $(x, y) = (0, 0)$, and the fluid with velocity U passes against the plate and causes a frictional drag force F_D . The velocity distribution $u(y)$ in the control volume is unknown; the only known condition is that on the plate the velocity is the same as in the first layer of fluid near the body, i.e., velocity is equal zero.

To satisfy the conservation of mass, the streamlines will be deflected away from the plate, and the pressure inside the control volume must remain constant. Taking into account these considerations, the streamlines outside this boundary layer will deflect an amount δ^* , called displacement thickness. The streamline in Figure (3.5) moves outward from $y = H$ at $x = 0$ to $Y = H + \delta^*$ at $x = x_1$ and the dashed lines denote the control volume for the analysis. We must have in mind that the only velocity distribution we know is at the beginning of the plate and at the end. The lower limit of this control volume is a streamline and the drag force is acting here. The other limit, the upper one, is also a streamline, but is outside the shear layer, so the viscous drag is zero along this line.

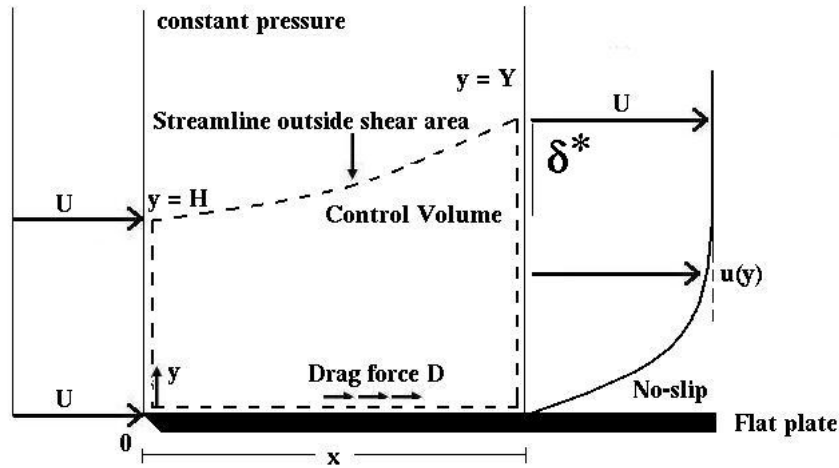


FIGURE 3.5 - Boundary layer for high \mathcal{R} number in a flat plate.

SOURCE: Adapted from: Kundu; Cohen (2004)

3.9.2 The displacement thickness

Using the conservation of mass in the control volume (Equation (3.14)), and assuming steady state gives:

$$\iint_{CS} \rho \mathbf{U} \cdot d\mathbf{A} = 0 = \int_0^Y \rho u dy - \int_0^H \rho U dy. \quad (3.42)$$

Considering constant density ρ and incompressible flow we have

$$UH = \int_0^Y u dy = \int_0^Y (U + u - U) dy = UY + \int_0^Y (u - U) dy. \quad (3.43)$$

Assuming that $Y = H + \delta^*$, it is possible to express Equation (3.43) as

$$U(Y - H) = U\delta^* = \int_0^Y (U - u) dy, \quad (3.44)$$

or:

$$\delta^* = \int_0^{Y \rightarrow \infty} \left(1 - \frac{u}{U}\right) dy. \quad (3.45)$$

The last expression is the definition of the boundary-layer displacement thickness δ^* . It is easy to see that δ^* is only a function of x , but depends strictly on the velocity distribution, u_y , in the boundary-layer.

3.9.3 Momentum thickness related to the flat plate drag

If we apply conservation of momentum to the control volume in the boundary-layer we have:

$$\sum F_x = -F_D = \iint_{CS} u(\rho \mathbf{U} \cdot d\mathbf{A}) = \int_0^Y u(\rho u dy) - \int_0^H U(\rho U dy), \quad (3.46)$$

or:

$$F_D = \rho U^2 H - \int_0^Y \rho u^2 dy. \quad (3.47)$$

If we assume constant density ρ and introducing

$$H = \int_0^Y \frac{u}{U} dy, \quad (3.48)$$

we have the turbulent drag force as

$$F_D = \rho \int_0^Y u(U - u) dy, \quad (3.49)$$

or

$$\frac{F_D}{\rho U^2} = \int_0^{Y \rightarrow \infty} \frac{u}{U} \left(1 - \frac{u}{U}\right) dy. \quad (3.50)$$

Equation (3.50) is the value of the momentum in the boundary-layer where the drag force is present when the Reynolds number is $\gg 1$. The evaluation of this expression needs also the knowledge of the velocity distribution in this layer. It is possible to obtain, from the derivation made in this section, an expression for the drag force in a turbulent regime given by

$$F_t = \frac{C_d A \rho U^2}{2}. \quad (3.51)$$

In Equation (3.51), A and R are the area and radius of the (spherical) drop, ρ is the ambient density. C_d is a common dimensionless parameter that describes the intensity of the drag force and depends, mainly, on the shape of the body, and could be defined as $C_d = F_t / (\frac{1}{2} \rho U^2 A)$, i. e., the rate between the drag force and the kinetic energy density times the transversal area of the body (LANDAU; LIFSHITZ, 1987). It is useful to describe the C_d parameter as a function of the Reynolds number (Eq. (3.29)). For example, for a spherical body, in the high Reynolds number range (between 10^3 and 10^5) the drag coefficient is between 0.4 and 0.6. For a low Reynolds number (2×10^{-1}), C_d is $\sim 10^2$ (see Figure 10.10 of Daugherty; Franzini

and Finnemore (1989). Therefore, the value of C_d depends on the system variables and it is difficult to give absolute numbers.

4 HYDRODYNAMICS MODEL FOR THE TRANSPORT IN THE INTERPLANETARY MEDIUM OF CORONAL MASS EJECTIONS

In this chapter, we develop the fluid dynamics theory to model the ICME transport in the interplanetary medium. In particular, we study the deceleration process for the fast ICMEs as a function of two kinds of drag force, depending on the speed U , (U and U^2), named laminar and turbulent viscous interaction, respectively.

4.1 ICME - SW interaction - Time dependence

4.1.1 Variability of ICME radius

For this approximation, we consider the ICME as a fluid moving inside other fluid (the SW) and affected by two viscous forces, laminar (Equation (3.41)) and turbulent (Equation (3.51)). The laminar or turbulent regime may apply depending on the difference of velocities, on the global ICME structure and/or magnetic field configuration. The laminar case may apply when an ICME smoothly opens the current sheet and travels inside it, or in the case of a quasi-parallel shock (with respect to the ambient SW magnetic field).

The turbulent case may apply to a quasi-perpendicular shock. In either case, laminar or turbulent, we assume that the magnetic effects are enclosed in microscopic process. We assume a spherical shape for the ICME with radius R , which changes as a function of the traveled distance as $R = x^{0.78}$ (LIU; RICHARDSON; BELCHER, 2005), and $A = \pi R^2$ is the ICME effective section. In a reference system where the fluid (in our case the SW) is at rest, the ICME velocity is $U = U_{cme} - U_{sw}$, where U_{sw} represents the solar wind speed.

The interchange of momentum may be due to waves or other collective microscopic plasma processes. We model the friction or drag force under which the ICME is affected using the Newton's Second Law (see Figure (4.1)) and considering the separate effects of laminar and turbulent viscous forces. This leads us to the following time differential equations

Laminar case

$$-L_1(U - U_{sw}) = m_{cme} \frac{d(U - U_{sw})}{dt}, \quad (4.1)$$

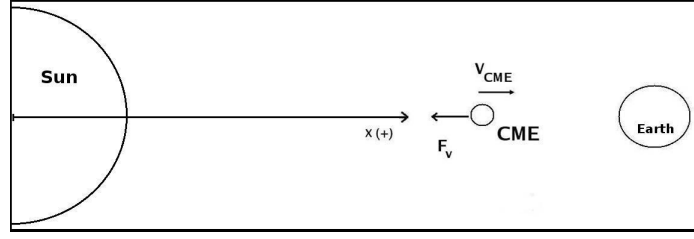


FIGURE 4.1 - Schematic representation of the total viscous force F_v which decelerates the ICME during the travel in the interplanetary space.

where $L_1 = 6\pi R\mu$.

Turbulent case

$$-\frac{T_1(U - U_{sw})^2}{2} = m_{cme} \frac{d(U - U_{sw})}{dt}, \quad (4.2)$$

where $T_1 = C_d A \rho_{sw}$.

The actual value of the Reynolds number in the interplanetary space is unknown, which allows us to explore the dynamics of the ICME through a total force constructed as the superposition of both laminar and turbulent effects given by

Turbulent+Laminar case

$$-L_1(U - U_{sw}) - \frac{T_1(U - U_{sw})^2}{2} = m_{cme} \frac{d(U - U_{sw})}{dt}. \quad (4.3)$$

A direct integration of these equations gives the time dependent solutions:

$$U = U_{sw} + (U_{cme}^0 - U_{sw})e^{-\frac{L_1 t}{m_{cme}}}, \quad (4.4)$$

$$U = U_{sw} + \frac{2m_{cme}(U_{cme}^0 - U_{sw})}{T_1(U_{cme}^0 - U_{sw})t + 2m_{cme}}, \quad (4.5)$$

$$U = U_{sw} + \frac{2L_1(U_{cme}^0 - U_{sw})}{[T_1(U_{cme}^0 - U_{sw}) + 2L_1] e^{\frac{L_1 t}{m_{cme}}} - T_1(U_{cme}^0 - U_{sw})}. \quad (4.6)$$

These three time differential equations (Equations (4.1), (4.2) and (4.3)) and their respective solutions, Equations (4.4), (4.5), and (4.6) are considering the radial expansion of the ICME in the interplanetary medium as Liu; Richardson and Belcher (2005) proposed in their work.

4.2 ICME - SW interaction - Position dependence

4.2.1 ICME Initial conditions

In this work we concentrate on the ICME dynamics, from ~ 30 to $\sim 215 R_\odot$. As the initial point is far enough from the solar surface, we assume the following considerations, presented by Chen (1996) and Sheeley et al. (1997):

- **The gravity force is negligible.** For example, in Figure 7 of Chen (1996), the gravity force tends to zero at approximately 110 min after the CME initiation, corresponding to a distance of the expanding loop apex of $\sim 2 R_\odot$ (see Figure 5 of the same paper).
- **The Lorentz force is negligible.** In Figure 9 of (CHEN, 1996), after 200 min of the CME initiation the Lorentz force is practically zero; this time corresponds to an apex height of $\sim 6 R_\odot$.
- **The solar wind speed is constant.** At $30 R_\odot$ the solar wind is already formed; we assume a constant speed of 400 km/s. Observationally, Sheeley et al. (1997) found that this constant speed begins at approximately $30 R_\odot$. Some models assume a speed profile of the form $v_{sw} = a_0 \tanh(x/b_0)$ and adjust the constants a_0 and b_0 to obtain a constant speed (400 km/s) at a given distance, for example at $35 R_\odot$ (CHEN; GARREN, 1993) and $40 R_\odot$ (CHEN, 1996).
- After the initial point, $30 R_\odot$ **the drag force is the only force acting on the system.**
- We do not consider the magnetic properties of ICMEs.

We plot in Figure (4.2) a typical speed profile (continuous line), $v_{sw} = a_0 \tanh(x/b_0)$, the complete Leblanc density model (diamonds), and the density profile using only the first term in the Leblanc density model $(a/x^2)^1$ (dotted line) (LEBLANC; DULK; BOUGERET, 1996). It is evident from this figure, that the proposed model reaches a constant speed at distances $\approx 30 R_\odot$. In the case of the Leblanc's model, we are interested in the density variation from $30 R_\odot$ to 1 AU. By inspection of Figure (4.2) it is evident that the density variations using all the terms in the Leblanc's model (diamonds curve) and using only the first term (dotted line curve) are similar after $15 R_\odot$. For this reason, and as our model explore the behavior of the ICME in the interplanetary medium, we choose a density profile equal to a/x^2 . The other two terms have importance only in the low solar atmosphere (below $15 R_\odot$).

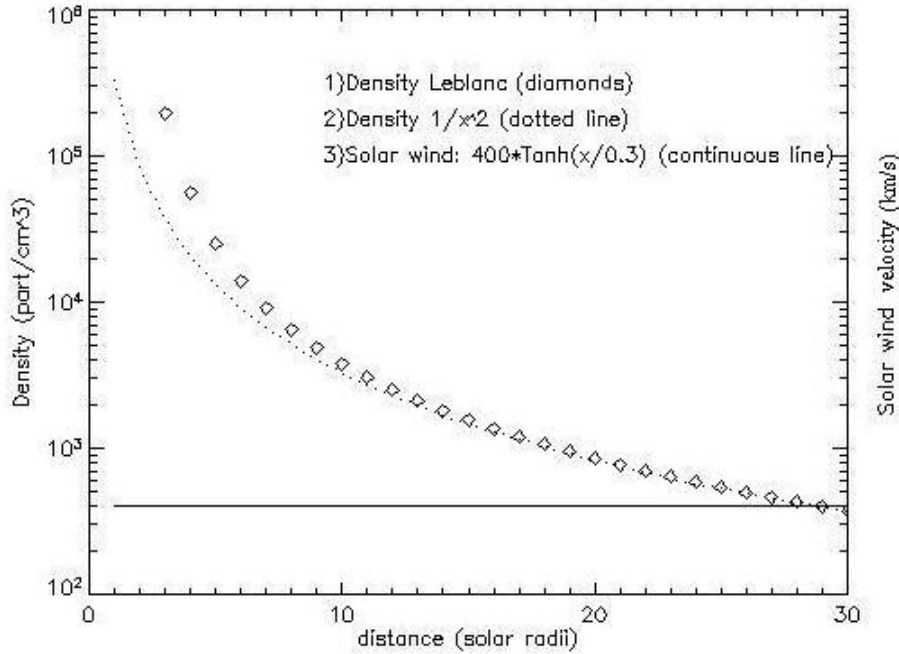


FIGURE 4.2 - Solar wind speed versus distance (continuous line), Leblanc density model versus distance (diamonds line) and density profile $1/x^2$ (dotted line) versus distance (distance in R_\odot).

4.2.2 Variability of ICME radius

We use the expressions for the drag forces (Equation (3.41) and (3.51)) in the equation of motion. We also consider that the ICME radius (R) varies with the distance

¹Leblanc coefficient a , see Section (4.2.3)

as $R = x^p$. We use a system of reference where the ambient SW is at rest. We obtain the following differential equations for laminar and turbulent regimes, respectively (BORGAZZI et al., 2009):

$$-6\pi\mu x^p(U - U_{sw}) = m_{cme}U \frac{dU}{dx} \quad (4.7)$$

and

$$-\frac{C_d\pi\rho_{sw}x^{2p}}{2}(U - U_{sw})^2 = m_{cme}U \frac{dU}{dx}. \quad (4.8)$$

Solutions of Equations (4.7) and (4.8) are given, respectively:

$$x^{(p+1)} - x_0^{(p+1)} = -\frac{m_{cme}(p+1)}{6\pi\mu} \left(U - U_0 + U_{sw} \ln \left[\frac{(U - U_{sw})}{(U_0 - U_{sw})} \right] \right) \quad (4.9)$$

and

$$x^{(2p+1)} - x_0^{(2p+1)} = -2\frac{m_{cme}(2p+1)}{C_d\pi\rho_{sw}} \times \left[\frac{U_{sw}}{(U_0 - U_{sw})} - \frac{U_{sw}}{(U - U_{sw})} + \ln \left[\frac{(U - U_{sw})}{(U_0 - U_{sw})} \right] \right]. \quad (4.10)$$

In Equations (4.9) and (4.10), U_0 and x_0 are the initial CME speed and position, respectively (as measured at the coronagraph field of view).

4.2.3 ICME interplanetary medium density and radius variable

In order to improve the analysis, we use the Leblanc et al. (1996) model to account for the variation of the SW density with the distance, given by:

$$\rho(x) = \frac{a}{x^2} + \frac{b}{x^4} + \frac{c}{x^6}, \quad (4.11)$$

where $a = 7.2$, $b = 1.95 \times 10^{-3}$ and $c = 8.1 \times 10^{-7}$ are empirical coefficients (in AU units). The quadratic term represents the density variation in the interplanetary space, whereas the high order terms represent the density variation in the low corona. In this way, the parameter a is computed using the density measured at 1 AU. As we

are interested only on the density variation in the interplanetary medium (from 30 R_\odot at 215 R_\odot), we only take into account the quadratic term in Equation (4.11).

4.2.3.1 Turbulent Regime

The turbulent regime, (Equation (3.51)), has an explicit dependence with the density, therefore, by using $\rho_{sw} = a/x^2$ we obtain the following equation:

$$-\frac{C_d \pi a x^{(2p-2)}}{2} (U - U_{sw})^2 = m_{cme} U \cdot \frac{dU}{dx}, \quad (4.12)$$

which has a solution given by:

$$-\frac{C_d \pi a}{2 m_{cme} (2p-1)} [x^{(2p-1)} - x_0^{(2p-1)}] = \frac{U_{sw}}{(U_0 - U_{sw})} - \frac{U_{sw}}{(U - U_{sw})} + \ln \left[\frac{(U - U_{sw})}{(U_0 - U_{sw})} \right]. \quad (4.13)$$

4.2.3.2 Laminar Regime

To describe the motion of ICMEs considering the laminar regime it is necessary to express the laminar force as a function of the density of the medium (in this case the SW density). Therefore, we use the relationship between the dynamic viscous coefficient μ and the kinematic viscous coefficient ν (KUNDU; COHEN, 2004), as:

$$\nu = \frac{\mu}{\rho_{sw}}. \quad (4.14)$$

With this consideration, the equation of motion is:

$$-6\pi\nu a x^{(p-2)} (U - U_{sw}) = m_{cme} U \cdot \frac{dU}{dx}, \quad (4.15)$$

and the solution is:

$$-\frac{6\pi\nu a}{m_{cme} (p-1)} [x^{p-1} - x_0^{p-1}] = U + U_{sw} \ln \frac{(U - U_{sw})}{(U_0 - U_{sw})} - U_0. \quad (4.16)$$

4.3 Results

In this Section we present the solutions for the hydrodynamics model explained in Sections (4.1), (BORGAZZI et al., 2008), and (4.2), (BORGAZZI et al., 2009). The following figures represent the behavior of the speed versus time and distance respectively, considering radius of the ICME and density of the solar wind variable with distance.

4.3.1 ICME - SW interaction - Time dependence

Upon inspection of solutions given by Equations (4.4) and (4.5) and comparing with experimental observations of the phenomena (GOPALSWAMY et al., 2000) we have identified extreme values for the viscosity and drag coefficient, μ and C_d , respectively. Such comparison was meant to recover the fast CME speeds near the Sun, around 400 km/s to almost 3000 km/s and near the Earth (i.e. at a distance of 1 AU), where the ICME speeds decrease to a range of 400 to 1000 km/s. In this way, the computed values for the viscosity and drag coefficient are $\mu_1 = 0.002$ kg/m.s and $C_{d_1} = 200$ for the minimum case; and $\mu_2 = 0.02$ kg/m.s and $C_{d_2} = 2000$ for the maximum drag effect. To analyze the motion described by our solutions (Equation (4.4) and (4.5)) we have plotted the resulting speed versus time, for the two extreme cases previously mentioned. Our results are plotted in Figures (4.3), for a laminar (a) and turbulent (b) ICME - SW interactions.

Continuous lines in Figure (4.3 a) represent the ICME dynamics in the laminar regime using μ_2 and dotted lines represent the same behavior, but with μ_1 . At time equal to $t_0 = 0$, the speed is the CME speed near the Sun. The stars and triangles are the ICME arrival time at 1 AU obtained using our solutions and considering μ_2 and μ_1 respectively. In Figure (4.3 b) the continuous lines are the solutions of Equation (4.5) under a drag coefficient C_{d_2} whereas the dotted lines are the solutions with C_{d_1} . In all cases we have used average values for the solar wind density, $\rho_{sw} = 10 \text{ part/cm}^3$ for the CME mass, $M_{cme} = 10^{15} \text{ g}$ and for the SW speed, $V_{sw} = 400 \text{ km/s}$.

Each line is the solution of the respective equation with different initial speed (U_{cme}) ranging from 400 km/s to 2000 km/s. Stars and triangles represent, again, the ICME arrival time at 1 AU, using our solutions. In order to analyze the simultaneous effect of laminar and turbulent forces over the ICME speed, we plot in Figure (4.4) a family of solutions of Equation (4.6) for different initial velocity conditions. Notice should be made on the emphasized damping effect occurring for the continuous line with

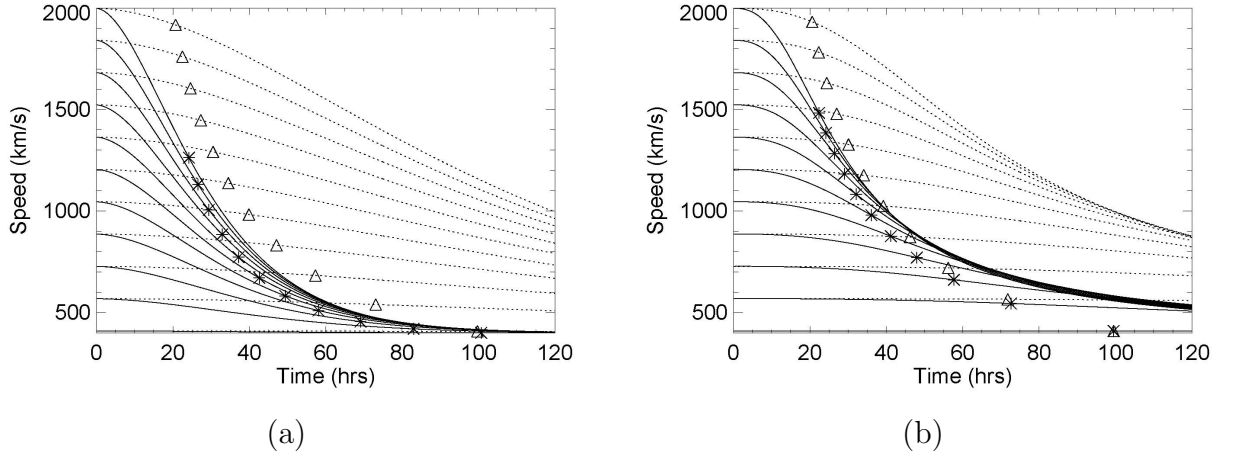


FIGURE 4.3 - a) Evolution of the ICME speed in terms of the initial CME speed under the laminar drag force. The dotted lines correspond to a viscous coefficient of 0.002 kg/m.s and the continuous lines to 0.02 kg/m.s. The stars and triangles represent the travel time from the Sun to 1 AU. b) Temporal behavior of the ICME speed under a turbulent drag force. The dotted lines correspond to a drag coefficient of 200 and the continuous lines to a value of 2000.

SOURCE: Borgazzi et al. (2008)

respect to the dotted lines. We use the same convention of the stars and triangles as in previous plots.

4.3.2 ICME - SW interaction - Distance dependence (case a)

Other interesting analysis of the CME speed behavior would be plotting Equations (4.4), (4.5) and (4.6) as a function of the traveled distance. In this way, we are able to compare our results with observations made at 1 AU. To compute the ICME speed as a function of distance, we evaluate Equations (4.4), (4.5) and (4.6) in 2400 time points from 0 to 431820 sec (5 days), i.e., $\Delta = 180$ sec. Then we compute the distance assuming constant speed during each interval.

Figures (4.5), and (4.6) represent the behavior of the speed as a function of distance for the ICMEs under the action of laminar, turbulent and coupled viscous forces, respectively.

Here the difference between parameters is evident. For example, an ICME with an initial speed of 2000 km/s will arrive at 1 AU with a speed of 1900 km/s and 1250 km/s using μ_1 and μ_2 , respectively. If the initial speed is 900 km/s, the speeds at 1

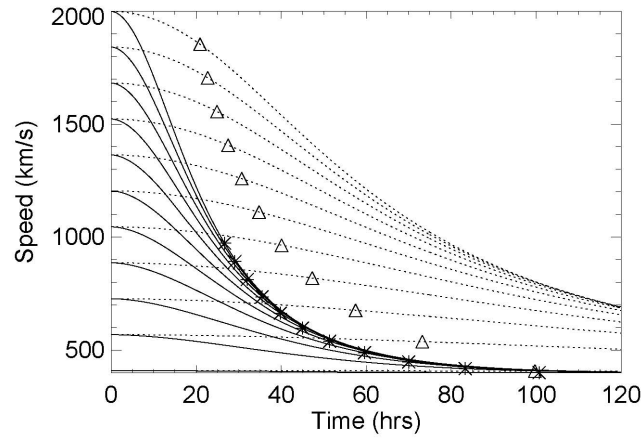


FIGURE 4.4 - ICME speed in terms of time, for laminar plus turbulent forces. Dotted lines represent a drag and viscous coefficient of 200 and 0.002 kg/m.s respectively, and continuous lines a drag coefficient of 2000 and a viscous coefficient of 0.02 kg/m.s.

SOURCE: Borgazzi et al. (2008)

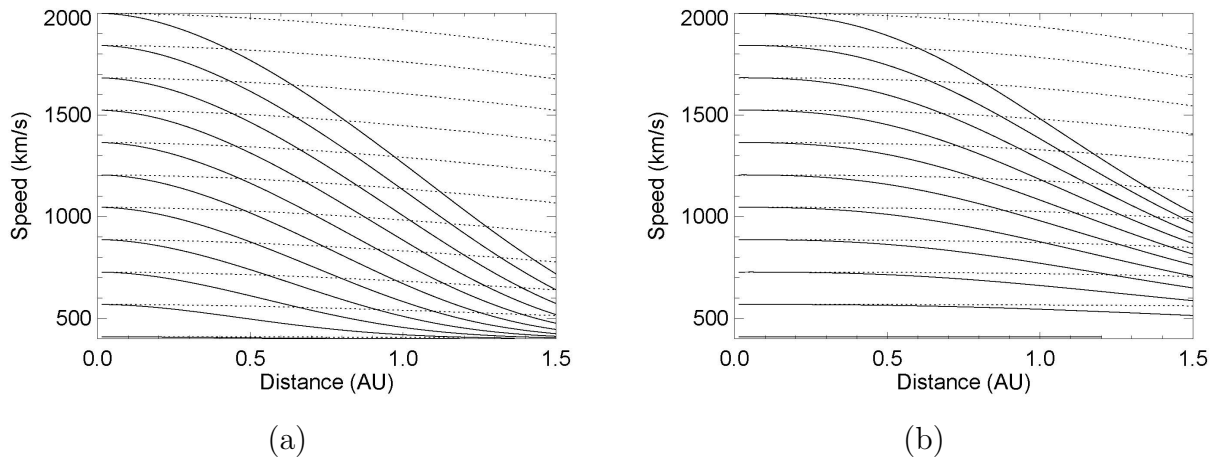


FIGURE 4.5 - a) ICME speed in terms of the distance to the Sun for the laminar interaction. Two cases are shown: the dotted lines represent the behavior using a viscous coefficient of 0.002 kg/m.s, and the continuous lines with a coefficient of 0.02 kg/m.s. b) Similar to Figure (4.5 a) but for the turbulent force. Dotted lines represent the behavior under a drag coefficient of 200, and the continuous lines with a coefficient of 2000.

SOURCE: Borgazzi et al. (2008)

AU are 820 km/s and 510 km/s, respectively.

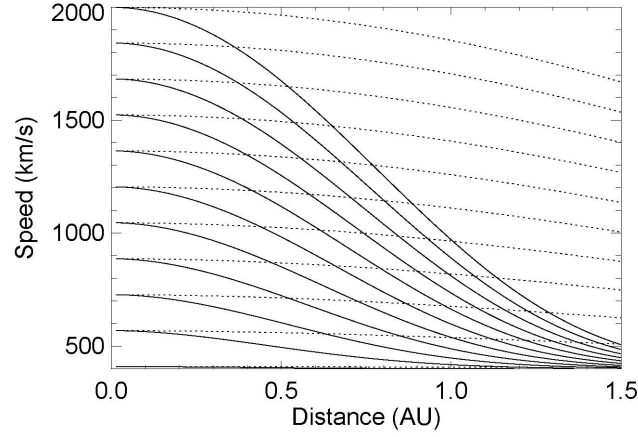


FIGURE 4.6 - Similar to Figure (4.5) but for the laminar plus turbulent forces. Dotted lines represent the ICME behavior under a drag coefficient of 200 and a viscous coefficient of 0.002 kg/m.s, and the continuous lines with a coefficient of 2000 and a viscous coefficient equal to 0.02 kg/m.s.

SOURCE: Borgazzi et al. (2008)

In the turbulent case, the speed at 1 AU is 1950 km/s using C_{d1} and 1500 km/s using C_{d2} for an initial speed of 2000 km/s. If the initial speed is 900 km/s, the speeds at 1 AU are 800 km/s and 550 km/s, respectively.

In the coupled case, using μ_1 and C_{d1} , the speed at 1 AU is 1880 km/s if the initial speed is 2000 km/s, and 870 km/s if the initial speed is 900 km/s. On the other hand, using μ_2 and C_{d2} , the arrival speed at 1 AU is 1000 km/s for an initial speed of 2000 km/s and 550 km/s when the initial speed is 900 km/s.

The minimum drag effect is reached when the force is laminar and $\mu = \mu_1$. An intermediate drag effect corresponds to the turbulent force and $C_d = C_{d2}$. The maximum drag effect is reached using the coupled force with $\mu = \mu_2$ and $C_d = C_{d2}$.

4.3.3 ICME - SW interaction - Distance dependence (case b)

To analyze the motion described by Equation (4.9) and (4.10), we present in Figure (4.7) the resultant speed as a function of the position, for different initial speeds, considering $U_{sw} = 400$ km/s. The plots are for two different values of μ , 0.1 g/cm.s (continuous lines) and 0.25 g/cm.s (dotted lines), and for C_d , 6×10^4 (continuous lines) and 1.6×10^5 (dotted lines). In all cases, we have chosen the parameters (μ

and C_d) in such a way that the ICME speed at 1 AU fall in a range similar to the observed.

The behavior of the speed versus position, given by Equation (4.13), can be seen in Figure (4.8), where we have plotted the solutions for different initial speeds and using two drag coefficients, 2×10^4 (continuous lines) and 8×10^4 (dotted lines).

The behavior of the speed versus position for the laminar case with density and radius variable can be seen in Figure (4.8), where we have plotted the solution (Equation (4.16)) for different initial speeds and using a value of $5 \times 10^{20} \text{ cm}^2 \cdot \text{s}$ (continuous lines) and $1.25 \times 10^{21} \text{ cm}^2 \cdot \text{s}$ (dotted lines) for the kinematic viscosity (ν).

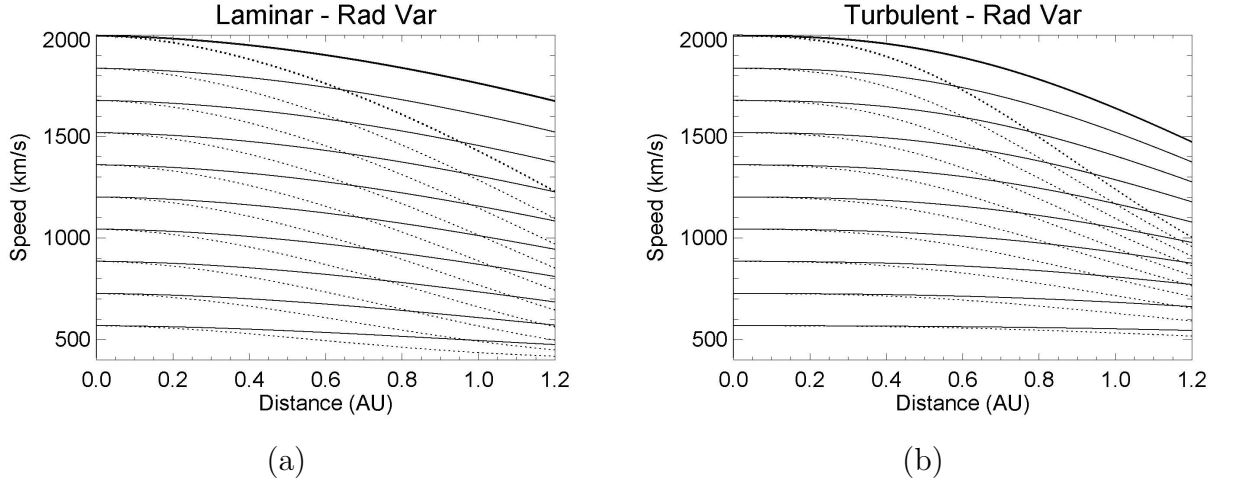


FIGURE 4.7 - a) ICME speed versus distance for laminar regime, showing a weak ($\mu = 0.1 \text{ g/cm.s}$ in continuous lines) and strong ($\mu = 0.25 \text{ g/cm.s}$ in dotted lines) ICME-SW interaction. Here and in the following figures, the y-axis at distance equal to zero, indicates the initial CME speed used to obtain the curves. b) ICME speed versus distance for turbulent regime, showing a weak ($C_d = 6 \times 10^4$ in continuous lines) and strong ($C_d = 1.6 \times 10^5$ in dotted lines) ICME-SW interaction.

SOURCE: Borgazzi et al. (2009)

4.4 Variation of parameters

Our major interest is the knowledge of the speed of the ICME versus distance in the interplanetary medium (Section (4.2.3)). In order to know how these solutions

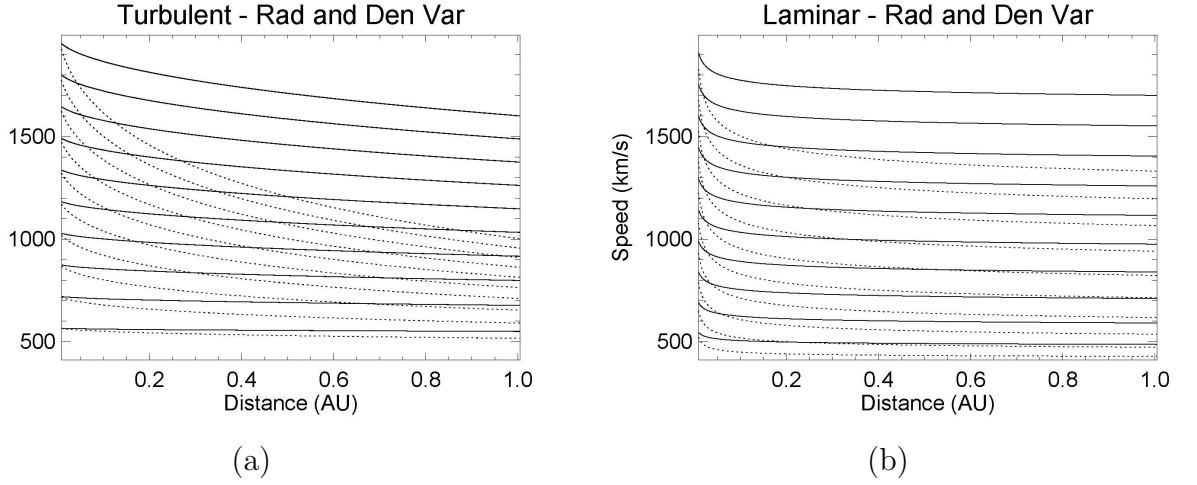


FIGURE 4.8 - a) ICME speed versus distance for turbulent regime considering ICME radius and SW density variable. The ICME-SW interaction is weak for a drag coefficient $C_d = 2 \times 10^4$ (continuous lines) and strong for $C_d = 8 \times 10^4$ (dotted lines). b) ICME speed versus distance for laminar regime considering ICME radius and SW density variable, in this case the value of the kinematic viscosity is $5 \times 10^{20} \text{ cm}^2/\text{s}$ for the weak ICME-SW interaction (continuous lines) and $1.25 \times 10^{21} \text{ cm}^2/\text{s}$ for the strong interaction (dotted lines).

SOURCE: Borgazzi et al. (2009)

depend on the physical medium it is necessary to determine first the weight of each parameter in the solution that characterize the interaction between the ICME and the solar wind and therefore, the changes in the ICME behavior. The main idea is to found which parameter (and in which range) may produce significant variations of the solutions. This will help us to know more about the interrelation between the ICME and the ambient medium.

In the laminar case, the relevant parameters are ICME mass (m_{cme}), solar wind velocity (V_{sw}), Leblanc density coefficient (a), (here a is defined as $a = \rho_{1AU} \cdot (1.5 \times 10^{13})^2 \cdot m_p$; ρ_{1AU} is de density of particles at 1 AU in $part/cm^3$, and m_p is the proton mass in g), exponent of radial expansion of the ICME (p), and kinematics viscous coefficient (ν).

Whereas in the turbulent case, the kinematic viscous coefficient is replaced by the drag coefficient (C_d); the other parameters are kept the same as in the laminar case.

Using these five parameters and the Kolmogorov-Smirnov test (K-S test, see Apendix (B)), it is possible to determine how the solutions vary when the parameters are

modified.

In other words, we are looking for a range of validity for each parameter, where the solutions behave as the observed ICMEs. In this way, we use the K-S test to know which parameter has more influence on the behavior of the solutions. The next section gives a brief summary of the steps followed to obtain the results of this exercise.

4.4.1 Methodology

- Select an initial CME speed equal to 1000 km/s.
- Select a fixed value for each parameter in such a way that the final speed is approximately 700 km/s.
- Select a (physically) valid range of variation for each parameter, taking care that the fixed value corresponds to the middle part of this range, Tables (4.1) and (4.2)
- Solve numerically Equations (4.13) and (4.16) in the range of variation of each parameter.
- Use the K-S test statistics (Appendix (B)) to ‘evaluate’ the difference between the solution using the fixed parameter and the solutions using the range of variation.
- Analyze the K-S difference, Figures (4.21) and (4.22), and select a minimum range of variation equal to 10 %, around the fixed parameters, Tables (4.3) and (4.4).
- Solve numerically Equation (4.13) and (4.16) for the minimum range of the variation of each parameter, 10 (%).
- Use the K-S test statistics to measure the difference between the solutions using the fixed parameters and the solutions using a 10 % of variation.
- Finally, by analysing the K-S test, find the weight of each parameter on the Equations (4.13) and (4.16).

Tables (4.1) and (4.2) show the fixed values, the range and percentage of variation of parameters for the two regimes. For the construction of these tables we take

into account that, at 1 AU, it is necessary to obtain speed values comparable to observations, i.e., if we have initial speed of 1000 km/s (data input), at 1 AU it is reasonable to obtain values of speed in the range of 700 km/s. Tables (4.3) and (4.4) show, for each regime and for each parameter, the range of variation, but using now a fixed percentage of 10 % with respect to the fixed values.

TABLE 4.1 - Variation of parameters - turbulent regime

| Parameter | Minimum | Fixed | Maximum | % variation |
|--|--------------------|--------------------|----------------------|-------------|
| Drag coefficient (C_d) | 20000 | 50000 | 80000 | 60 |
| Mass (m_{cme} , g) | 5×10^{15} | 1×10^{16} | 1.5×10^{16} | 50 |
| Density ($particle/cm^3$) | 5.4 | 7.2 | 9 | 25 |
| Exponent (p) | 0.59 | 0.79 | 0.99 | 25 |
| Solar wind velocity (V_{sw} , km/s) | 200 | 400 | 600 | 50 |

TABLE 4.2 - Variation of parameters - laminar regime

| Parameter | Minimum | Fixed | Maximum | % variation |
|--|--------------------|--------------------|----------------------|-------------|
| Kinematic vis. coeff. (ν , cm^2/s) | 5×10^{20} | 1×10^{21} | 1.5×10^{21} | 50 |
| Mass (m_{cme} , g) | 5×10^{15} | 1×10^{16} | 1.5×10^{16} | 50 |
| Density ($particle/cm^3$) | 5.4 | 7.2 | 9 | 25 |
| Exponent (p) | 0.59 | 0.79 | 0.99 | 25 |
| Solar wind velocity (V_{sw} , km/s) | 200 | 400 | 600 | 50 |

TABLE 4.3 - Variation of parameters (% 10) - turbulent regime

| Parameter | Minimum | Fixed | Maximum |
|--|--------------------|--------------------|----------------------|
| Drag coefficient (C_d) | 45000 | 50000 | 55000 |
| Mass (m_{cme} , g) | 9×10^{15} | 1×10^{16} | 1.1×10^{16} |
| Density ($particle/cm^3$) | 6.48 | 7.2 | 7.92 |
| Exponent (p) | 0.73 | 0.79 | 0.9 |
| Solar wind velocity (V_{sw} , km/s) | 360 | 400 | 440 |

TABLE 4.4 - Variation of parameters (% 10) - laminar regime

| Parameter | Minimum | Fixed | Maximum |
|---|--------------------|--------------------|----------------------|
| Kinematic vis. coeff. ($\nu, cm^2/s$) | 9×10^{20} | 1×10^{21} | 1.1×10^{21} |
| Mass (m_{cme}, g) | 9×10^{15} | 1×10^{16} | 1.1×10^{16} |
| Density ($particle/cm^3$) | 6.48 | 7.2 | 7.92 |
| Exponent (p) | 0.73 | 0.79 | 0.9 |
| Solar wind velocity ($V_{sw}, km/s$) | 360 | 400 | 440 |

4.4.2 Results - Variation of parameters

Using the parameters in the range of variation showed in Tables (4.1), (4.2), (4.3), and (4.4) solving the equations (4.13) and (4.16), of speed versus distance, and the corresponding K-S test results for both regimes as follows:

When we consider the mass variations, for example, we choose a suitable variation range for this parameter (values in Tables (4.1), (4.2), (4.3) and (4.4)), while the other 5 parameters are fixed (using the fixed value). When we consider the exponent variation, we choose a suitable variation range for the exponent p , and the other are fixed. Similar procedure is used for the analysis of the other parameters.

4.4.2.1 Turbulent regime

Figures (4.9), (4.10), (4.11) show the plots of the family of solutions in the case of turbulent regime, with the parameter variations of Table (4.1). In these plots the thick black line is obtained using the fixed values (second column in Table (4.1)).

Figures (4.9), (4.10), and (4.11) show the behavior for the speed versus distance of the ICME (turbulent regime), Section (4.2.3), using the five parameters considered, i.e., mass (m_{cme}); solar wind speed (V_{sw}); density; exponent (p); and drag coefficient (C_d) according to Table (4.1).

In Table (4.5) are presented the values of the computed final speed at 1 AU obtained with the maximum, fixed and minimum values of each parameter. The percentage of variation of the speed at 1 AU with respect of the fixed values is also presented. In Figures (4.12), (4.13) and (4.14) are plotted the family of curves for the turbulent regime using the values of Table (4.3). In these plots the thick black line is obtained using the values of the second column in Table (4.3), i.e., the solution found using the fixed values for each parameter.

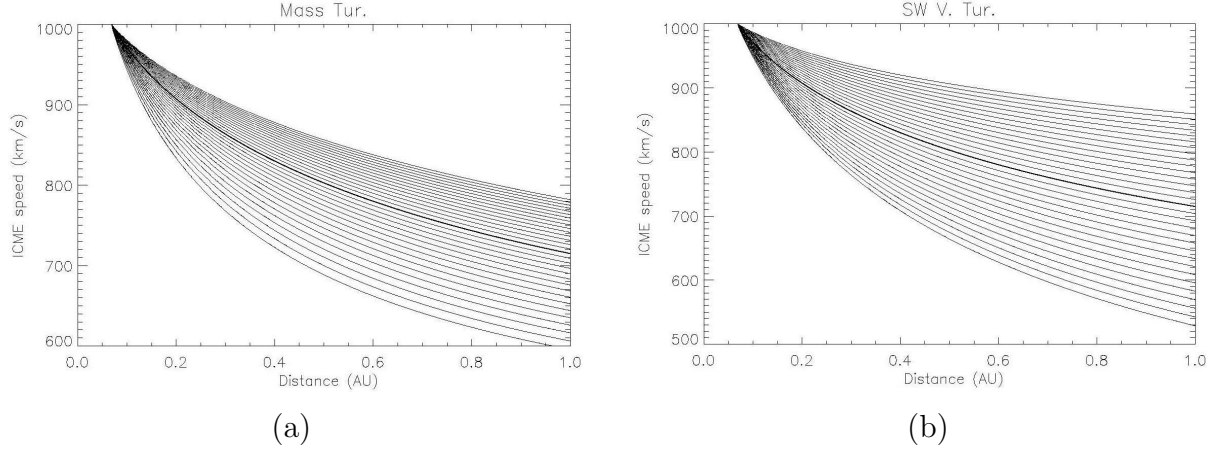


FIGURE 4.9 - a) Speed versus distance family solutions for the turbulent regime with the variation of mass (m_{cme}) parameter presented in Table (4.1) (second line). b) Speed versus distance family solutions for the turbulent regime with the variation of solar wind velocity (V_{sw}) parameter presented in Table (4.1) (fifth line).

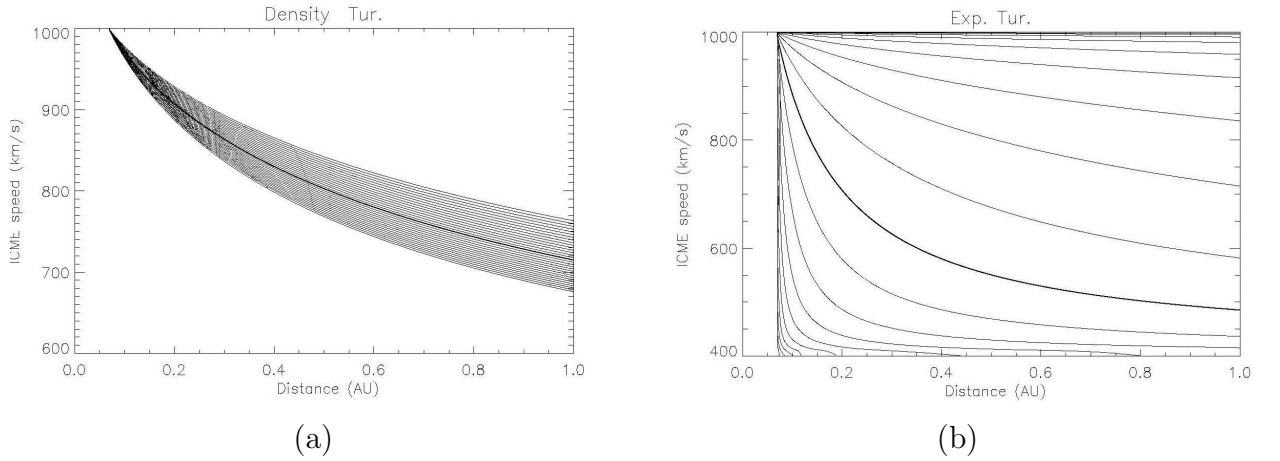


FIGURE 4.10 - a) Speed versus distance family solutions for the turbulent regime with the variation of density parameter presented in Table (4.1) (third line). b) Speed versus distance family solutions for the turbulent regime with the variation of exponent (p) parameter presented in Table (4.1) (fourth line).

Figures (4.12), (4.13), and (4.14) show the behavior for the speed versus distance of the ICME in the turbulent regime, with the same five parameters and conditions considered as in the previous example, but now using the values of Table (4.3), i.e., 10 % of variation.

In Table (4.6) are presented the values of the final speed at 1 AU obtained for an

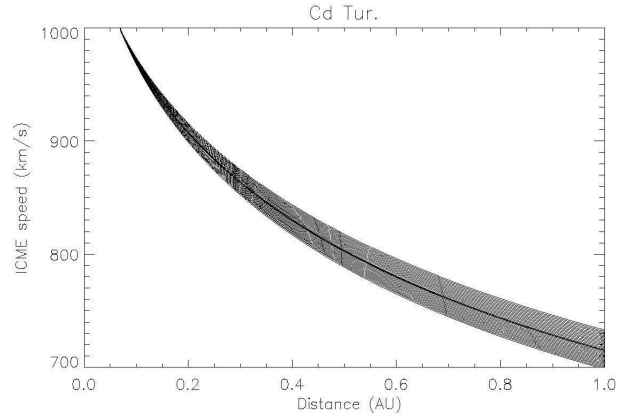


FIGURE 4.11 - Speed versus distance family solutions for the turbulent regime with the variation of drag coefficient (C_d) parameter presented in Table (4.1) (first line).

TABLE 4.5 - Values of the computed final speed (in km/s) at 1 AU for an initial CME speed of 1000 km/s for the maximum, fixed and minimum values of each parameter, Table (4.1), and minimum and maximum percentage of variations values of speeds at 1 AU with respect of the fixed values, turbulent regime [(*) value out of range].

| | Minimum | Fixed | Maximum | % min. | % max. |
|----------------------------|---------|--------|---------|--------|--------|
| mass (m_{cme}) | 584.82 | 702.88 | 771.97 | -16.80 | 9.70 |
| solar wind (V_{sw}) | 511.05 | 702.88 | 852.40 | -27.29 | 21.27 |
| density | 751.95 | 702.82 | 663.71 | 6.98 | -5.57 |
| exponent (p) | 997.91 | 479.07 | —* | 108.30 | —* |
| drag coefficient (C_d) | 844.07 | 702.88 | 621.14 | 20.09 | -11.63 |

initial CME speed of 1000 km/s and varying by 10 % the input parameters..

TABLE 4.6 - Values of the computed final speed (in km/s) at 1 AU for an initial CME speed of 1000 km/s for the maximum, fixed and minimum values of each parameter, Table (4.3), and minimum and maximum percentage of variations values of speed at 1 AU with respect to the fixed values, turbulent regime [(*) value out of range].

| | Minimum | Fixed | Maximum | % min. | % max. |
|----------------------------|---------|--------|---------|--------|--------|
| mass (m_{cme}) | 684.39 | 702.88 | 719.39 | -2.63 | 2.34 |
| solar wind (V_{sw}) | 667.98 | 702.88 | 736.07 | -4.97 | 4.72 |
| density | 721.16 | 702.88 | 686.19 | 2.60 | -1.58 |
| exponent (p) | 968.02 | 487.64 | —* | 102.20 | —* |
| drag coefficient (C_d) | 721.13 | 702.84 | 686.19 | 2.60 | -2.37 |

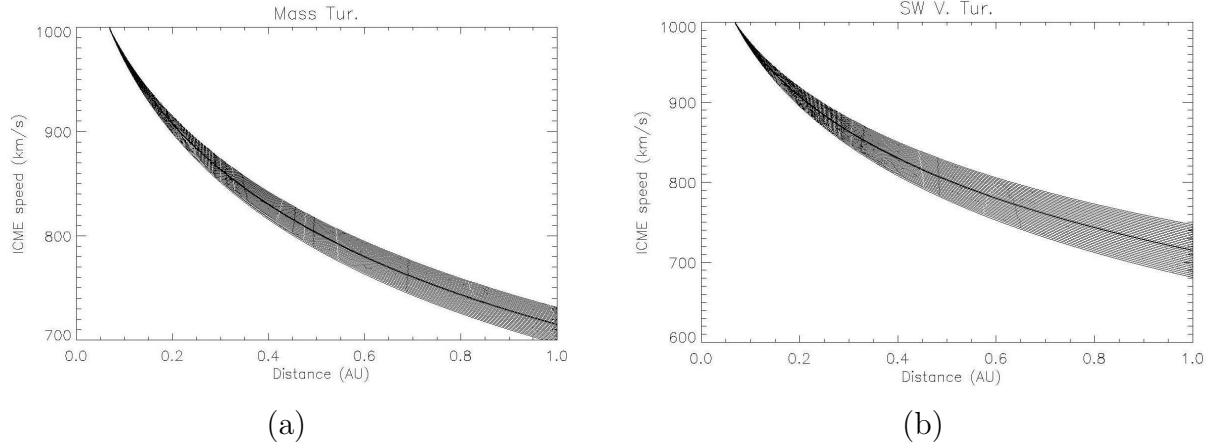


FIGURE 4.12 - a) Speed versus distance family solutions for the turbulent regime with the variation of mass (m_{cme}) parameter presented in Table (4.3) (second line). b) Speed versus distance family solutions for the turbulent regime with the variation of solar wind velocity (V_{sw}) parameter presented in Table (4.3) (fifth line).

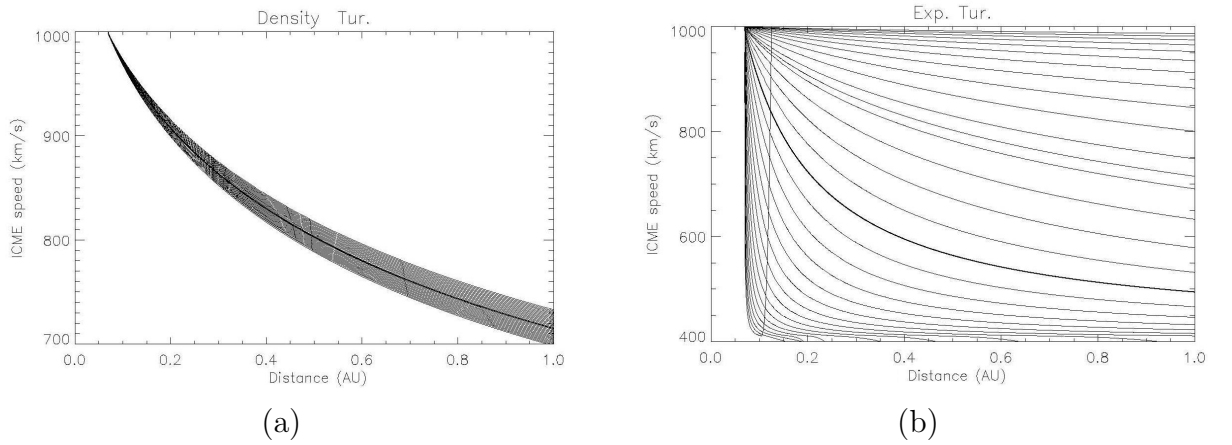


FIGURE 4.13 - a) Speed versus distance family solutions for the turbulent regime with the variation of density parameter presented in Table (4.3) (third line). b) Speed versus distance family solutions for the turbulent regime with the variation of exponent (p) parameter presented in Table (4.3) (fourth line).

4.4.2.2 Laminar regime

For the laminar regime, Figures (4.15), (4.16), and (4.17) show the behavior of the solutions using the values of Table (4.2). In these plots, the thick black line is obtained using the values of the second column in Table (4.2), i.e., the fixed values for each parameter. Figures (4.15), (4.16), and (4.17) show the behavior for the speed versus distance of the ICME in laminar regime, using the five parameters

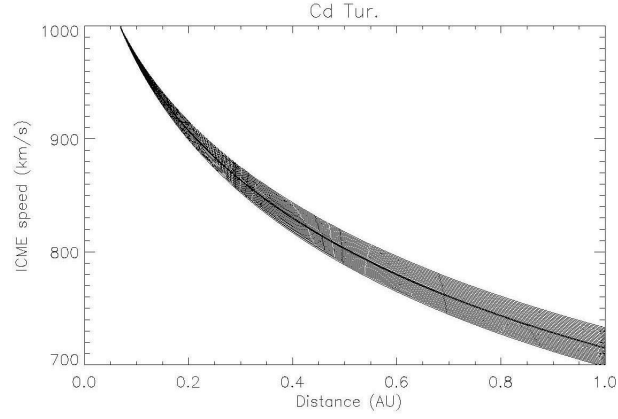


FIGURE 4.14 - Speed versus distance family solutions for the turbulent regime with the variation of drag coefficient (C_d) parameter presented in Table (4.3) (first line).

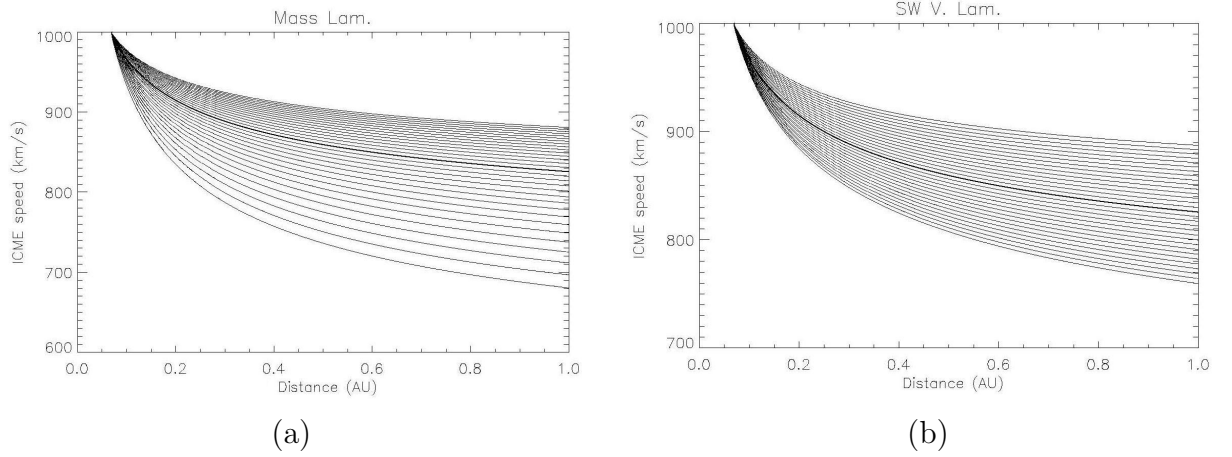
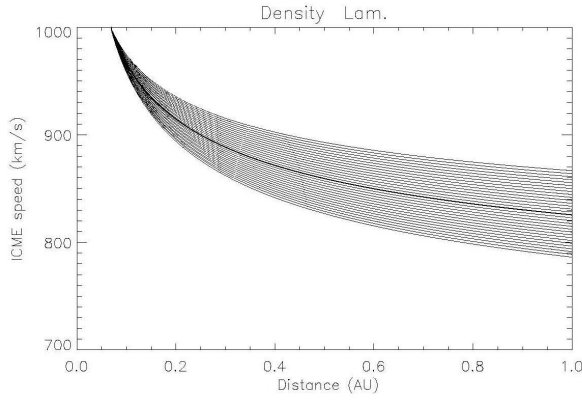


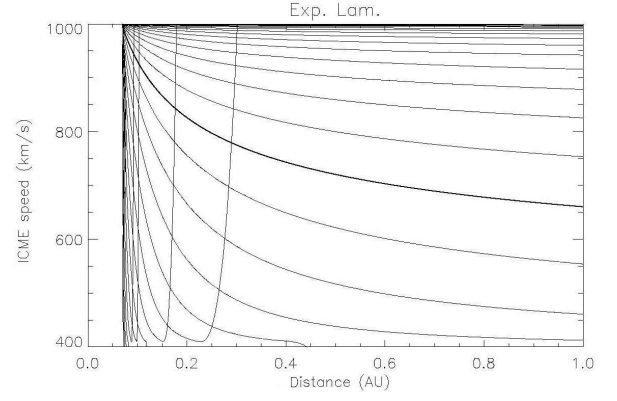
FIGURE 4.15 - a) Speed versus distance family solutions for the laminar regime with the variation of mass (m_{cme}) parameter presented in Table (4.2) (second line). b) Speed versus distance family solutions for the laminar regime with the variation of solar wind (V_{sw}) parameter presented in Table (4.2) (fifth line).

according to Table (4.2).

The same procedure used in the turbulent case is used here, including the fact that the initial speed of the CME is 1000 km/s, when analyzing the variation of the other parameters. In Table (4.7) are presented the values of the final speed at 1 AU obtained for the maximum, fixed and minimum values of the related parameters, and the percentage of variation of the speed at 1 AU with respect to the fixed values of the table. For the case of the same regime but using the values of Table (4.4),



(a)



(b)

FIGURE 4.16 - a) Speed versus distance family solutions for the laminar regime with the variation of density parameter presented in Table (4.2) (third line). b) Speed versus distance family solutions for the laminar regime with the variation of exponent (p) parameter presented in Table (4.2) (fourth line).

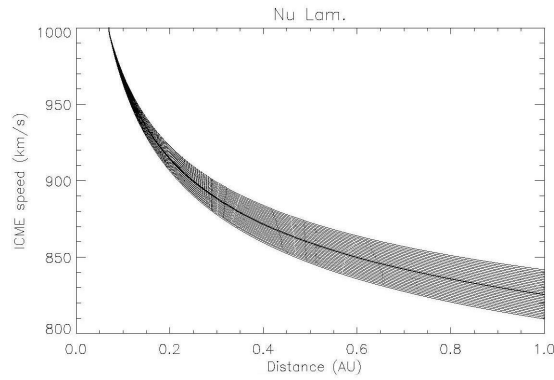


FIGURE 4.17 - Speed versus distance family solutions for the laminar regime with the variation of kinematic viscous coefficient (ν) parameter presented in Table (4.2) (first line).

(variation of 10 %), the results are plotted in Figures: (4.18), (4.19), and (4.20). In these plots the thick black line is obtained using the values of the second column in Table (4.4), i.e., the fixed values for each parameter.

In Table (4.8) are presented the values of the computed final speed (at 1 AU) and the percentage of variation, for an initial CME speed of 1000 km/s and using the maximum, fixed and minimum values of the parameters in Table (4.2). In the case of the behavior of the p parameter, there is a singular point in the solution for the speed versus distance, Equations (4.16) and (4.13); when $p = 1$ for the laminar and

TABLE 4.7 - Values of the computed final speed (in km/s) at 1 AU for an initial CME speed of 1000 km/s for the maximum, fixed and minimum values of each parameter, Table (4.2), and minimum and maximum percentage of variation values of speed at 1 AU with respect to the fixed values, laminar regime [(*) value out of range].

| | Minimum | Fixed | Maximum | % min. | % max. |
|-------------------------|---------|--------|---------|--------|--------|
| mass (m_{cme}) | 673.82 | 821.37 | 877.77 | -17.96 | 6.87 |
| solar wind (V_{sw}) | 753.63 | 821.37 | 884.48 | -8.25 | 7.68 |
| density | 863.36 | 821.26 | 8781.82 | 5.11 | -4.87 |
| exponent (p) | 997.73 | 653.27 | —* | 52.73 | —* |
| kin. vis. coeff. | 907.20 | 821.37 | 743.33 | 10.45 | -9.50 |

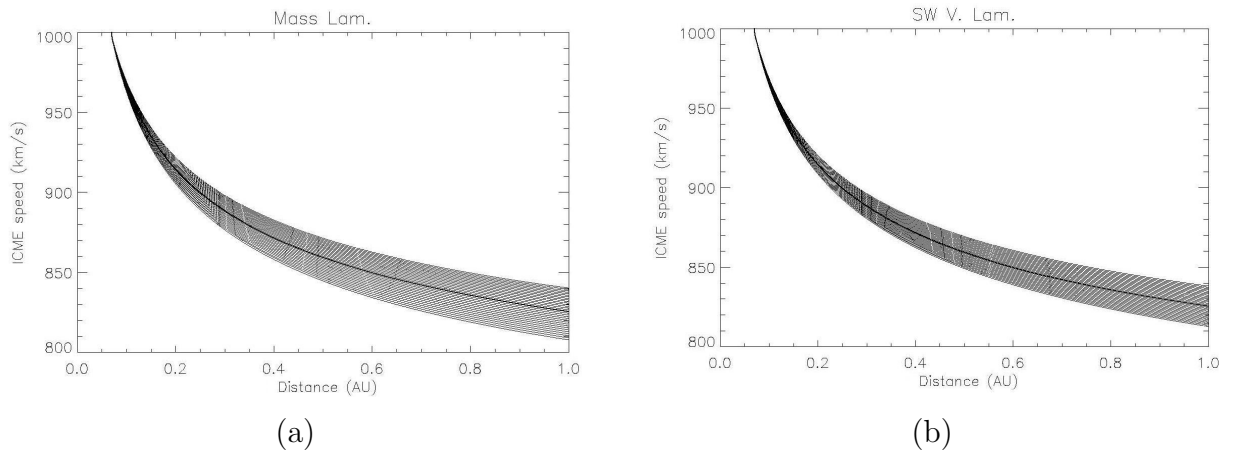


FIGURE 4.18 - a) Speed versus distance family solutions for the laminar regime with the variation of mass (m_{cme}) parameter presented in Table (4.4) (second line). b) Speed versus distance family solutions for the laminar regime with the variation of solar wind (V_{sw}) parameter presented in Table (4.4) (fifth line).

TABLE 4.8 - Values of the computed final speed (in km/s) at 1 AU for an initial CME speed of 1000 km/s obtained for the maximum, fixed and minimum values of each parameters, Table (4.2), and minimum and maximum percentage of variation values of speed at 1 AU with respect to the fixed values, laminar regime [(*) value out of range].

| | Minimum | Fixed | Maximum | % min. | % max. |
|-------------------------|---------|--------|---------|--------|--------|
| mass (m_{cme}) | 803.37 | 821.37 | 836.43 | -2.19 | 1.83 |
| solar wind (V_{sw}) | 808.21 | 821.37 | 834.33 | -1.60 | 1.57 |
| density | 837.95 | 821.37 | 805.12 | 2.02 | -1.97 |
| exponent (p) | 966.44 | 666.09 | —* | 45.09 | —* |
| kin. vis. coeff. | 837.95 | 821.37 | 805.12 | 2.02 | -1.98 |

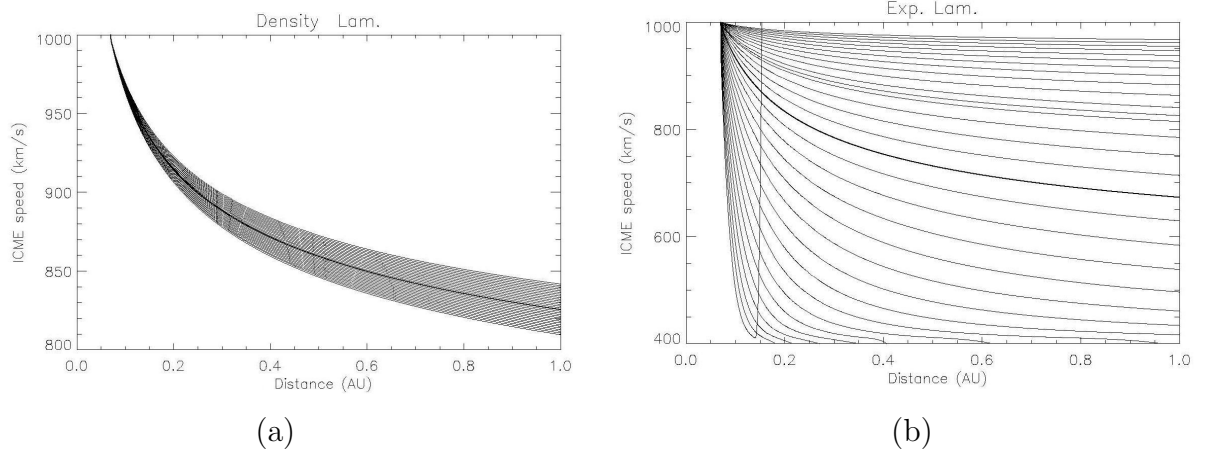


FIGURE 4.19 - a) Speed versus distance family solutions for the laminar regime with the variation of density parameter presented in Table (4.4) (third line). b) Speed versus distance family solutions for the laminar regime with the variation of exponent (p) parameter presented in Table (4.4) (fourth line).

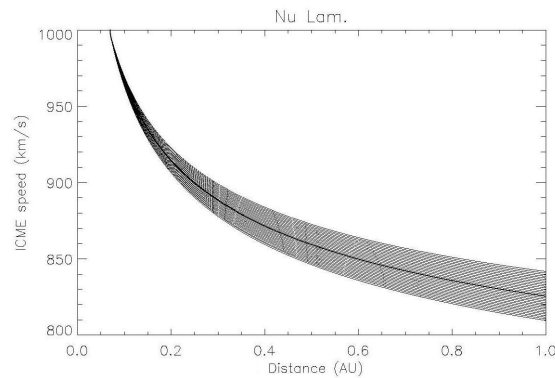


FIGURE 4.20 - Speed versus distance family solutions for the laminar regime with the variation of kinematic viscous coefficient (ν) parameter presented in Table (4.4) (first line).

$p = 0.5$ for the turbulent regime. The extreme behavior of the solutions in these cases, for speeds near the solar wind velocity (400 km/s), can be seen in Figures (4.19 b) and (4.16 b), for example.

To understand the behavior of the solution, we use the Kolmogorov-Smirnov test, as shown in Figures (4.21), for the laminar case, and (4.22), for the turbulent case. In these figures we have plotted the K-S statistics for the five parameters. The line code is: m_{cme} (dash line), V_{sw} (dash-dot-dot-dot line), density (dash-dot line), p (dot line) and ν or C_d (continuous line) for the regime (laminar/turbulent). In these figures

we plot the K-S statistics, which is equivalent to the distance ‘D’ between curves (see Appendix B), versus the percentage of variation. The K-S statistics shows how far are the solutions constructed using the values of the range for each parameter from the solution constructed using the fixed values. In all cases the zero point in the x axis corresponds to the comparison between the same curve, i.e., using the fixed value of each parameter.

4.4.2.3 K - S test result, laminar regime

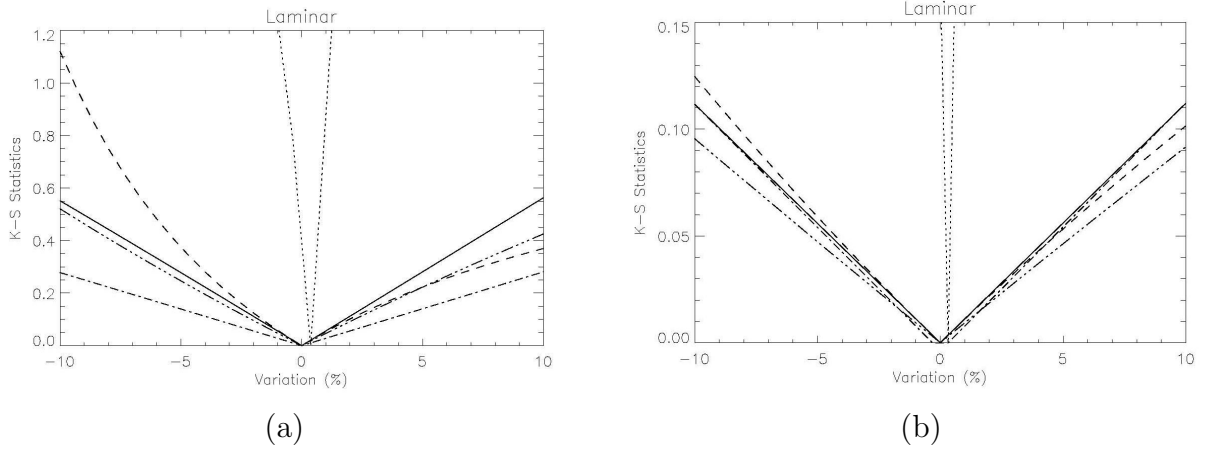


FIGURE 4.21 - a) Result of the K-S test for the laminar case using the five parameters: Mass (m_{cme}) (dash line), Solar wind velocity (V_{sw}) (dash-dot-dot-dot line), Density (dash-dot line), Exponent (p) (dot line), and Kinematic viscous coefficient (ν) (continuous line). As presented in Table (4.2). b) Result of the K-S test for the laminar using the five parameters: Mass (m_{cme}) (dash line), Solar wind velocity (V_{sw}) (dash-dot-dot-dot line), Density (a) (dash-dot line), Exponent (p) (dot line), and Kinematic viscous coefficient (ν) (continuous line). As presented in Table (4.4).

As can be seen in Figure (4.21 a), for the laminar regime, the largest variation is reached when the exponent (p) parameter is varied, followed by the kinematic viscous coefficient (ν), the solar wind variation (V_{sw}), the mass (m_{cme}) and finally the density. This is looking in the positive side of the x axis. There is an asymmetric behavior with respect to the zero point. In the negative x axis: the largest variation is for the exponent (p) instead of the kinematic viscous coefficient (ν). In this case the second parameter is the mass (m_{cme}), after that the kinematic viscous coefficient (ν), the solar wind (V_{sw}), and the last is the density.

For Figure (4.21 b), laminar regime but with 10 % parameter variation, the largest

distance on (right side of the x axis) is for the exponent (p) parameter followed by the kinematic viscous coefficient (ν), density, mass (m_{cme}) and finally the solar wind velocity (V_{sw}). In the case of the left side of the x axis the order change to: exponent (p) parameter, mass (m_{cme}), kinematic viscous coefficient (ν), density and finally solar wind velocity (V_{sw}).

4.4.2.4 K - S test result, turbulent regime

Figures (4.22 a) and (4.22 b) show the behavior of the K-S statistics when the 5 parameters are varied, m_{cme} (dash line), V_{sw} (dash-dot-dot-dot line), density (dash-dot line), p (dot line) and ν or C_d (continuous line), using the values of Tables (4.1) and (4.3). For Figure (4.22 a), turbulent regime, using variations of table, the

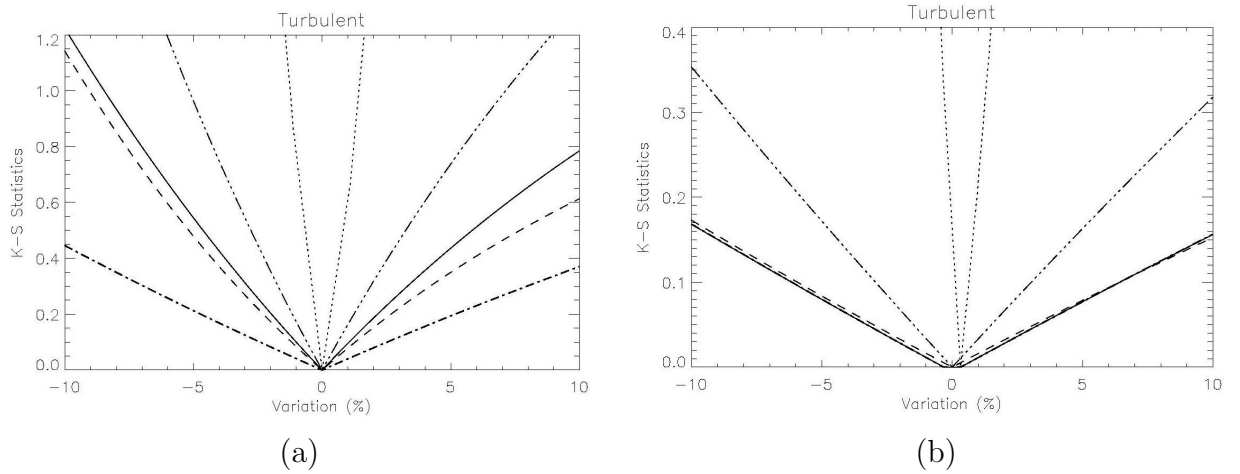


FIGURE 4.22 - a) Result of the K-S test for the turbulent case using the five parameters: Mass (m_{cme}) (dash line), Solar wind velocity (V_{sw}) (dash-dot-dot-dot line), Density (dash-dot line), Exponent (p) (dot line), and Drag Coefficient (C_d)(continuous line). Table (4.1). b) Result of the K-S test for the turbulent using the five parameters: Mass (m_{cme}) (dash line), Solar wind velocity (V_{sw}) (dash-dot-dot-dot line), Density (dash-dot line), Exponent (p) (dot line), and Drag Coefficient (C_d)(continuous line). Variation parameter of 10 %. Table (4.3).

largest distance is reached when varying the exponent (p) parameter followed by the solar wind velocity (V_{sw}), the drag coefficient (C_d), the mass (m_{cme}), and finally the kinematic viscous coefficient (ν). As in the previous example it is possible to observe an asymmetric behavior.

For Figure (4.22 b), turbulent regime but with 10 %, the largest variation is for

the exponent (p) parameter followed for the solar wind velocity (V_{sw}), the mass (m_{cme}), the drag coefficient (C_d), and the density. As in the previous example it is possible to observe that the behavior with respect to the zero point in the x axis is asymmetric. A last comment about the behavior of the p parameter: As it is very sensitive to changes in its values (what can be seen in Figures (4.21 a), (4.21 b), (4.22 a), and (4.22 b), the solutions take extreme values very quickly, and they must not be taken into account.

5 DATA

Any physical model must be confronted against observations to proof its validity. This chapter presents the analysis of the observation used to compare with the ICME analytic model (chapter (4), section (4.2.3)). For this purpose two kinds of data were selected: insitu satellite data with plasma parameters, and remote Type II burst radio data.

5.1 Data Analysis

For clarity, we present a summary of the analysis:

1) Selection of events. We choose:

- 43 geoeffective events, in this way we have the most complete (and published) information about each event.
- 15 events (a subset of the 43 geoeffectives events) which have Type II bursts associated.
- 7 events observed at distances less than 1 AU, we want to validate the model at these distances.

2) Input parameters of the model.

- Fixed:
The observed initial velocity of the CME and the final velocity of the ICME.
- Known variables with physically plausible ranges:
Mass (m_{cme}), solar wind velocity (v_{sw}) and density of the interplanetary medium. We selected the proper variation ranges within the observed values.
- Unknown variables:
For ν , C_d and p parameters we choose ranges where the solution were valid.

3) Iterative solutions.

- We fixed the middle part of the range of variation of each parameter.

- We solved equations (4.13) and (4.16) using the fixed values except for one of the parameters.
- We vary iteratively this parameter until it is found an acceptable solution, this is when the final velocity of the model is equal to the observed velocity.
- When an acceptable solution is found, the corresponding parameter is fixed and used in the following steps.
- The iterative process continues for the rest of the parameters.

4) Analysis of the results.

From the previous steps, we obtained:

- The best solution for each event in terms of the initial and final speeds.
- The best range of values for each parameter which result in valid solutions.

5.2 Satellite data

5.2.1 Data - At 1 AU

We have selected 43 full or partial halo CMEs and the respective ICMEs events registered by SOHO-LASCO since 1998 to 2005, (MANOHARAN, 2007). These events were selected because we have insitu data of the ICMEs at 1 AU, and it is possible the CME-ICME relationship. The data are presented in Table (5.1). The first column represents the date and the followings, the time of occurrence in universal time (UT) and the initial velocity of the CME (km/s). The other columns represent similar data, but in this case for the ICMEs. Finally, is the ambient solar wind density in $particles/cm^3$ at 1 AU (ρ_{1AU}) and the ICME transit time (time to arrive at 1 AU) ($t.t.$) in hours.

TABLE 5.1 - CME and ICME events observed [(*) values not measured].

| CME | | | | ICME | | | | |
|-----|------------|-------|-------|------------|-------|-------|--------------|------------|
| | Date | Time | V_0 | Date | Time | V_f | ρ_{1AU} | t.t. |
| 1 | 1998/04/29 | 19:59 | 1374 | 1998/05/02 | 05:00 | 621 | 10 | 57:01 |
| | | | | | | | | (continue) |

TABLE 5.1 - Continuation

| | Date | Time | V_0 | Date | Time | V_f | ρ_{1AU} | t.t. |
|----|------------|-------|-------|------------|-------|-------|--------------|------------|
| 2 | 1998/11/05 | 20:44 | 1119 | 1998/11/09 | 04:00 | 620 | 5 | 79:16 |
| 3 | 1999/09/20 | 06:06 | 604 | 1999/09/22 | 19:00 | 500 | 10 | 60:54 |
| 4 | 2000/02/10 | 02:30 | 944 | 2000/02/12 | 09:00 | 425 | 10 | 54:30 |
| 5 | 2000/04/04 | 16:32 | 1188 | 2000/04/06 | 04:00 | 570 | 5 | 39:28 |
| 6 | 2000/05/22 | 01:50 | 649 | 2000/05/24 | 12:00 | 620 | 5 | 58:10 |
| 7 | 2000/07/14 | 10:54 | 1674 | 2000/07/15 | 19:00 | 990 | 5 | 32:06 |
| 8 | 2000/08/08 | 15:54 | 867 | 2000/08/10 | 19:00 | 400 | 4 | 51:06 |
| 9 | 2000/08/09 | 16:30 | 702 | 2000/08/12 | 05:00 | 567 | 5 | 60:30 |
| 10 | 2000/09/16 | 05:18 | 1215 | 2000/09/17 | 21:00 | 760 | 4 | 39:32 |
| 11 | 2000/10/01 | 17:50 | 586 | 2000/10/05 | 13:00 | 510 | 2 | 91:10 |
| 12 | 2000/10/09 | 23:50 | 770 | 2000/10/13 | 12:00 | 395 | —* | 84:10 |
| 13 | 2000/10/25 | 08:26 | 770 | 2000/10/28 | 21:00 | 400 | 4 | 84:34 |
| 14 | 2000/11/26 | 17:06 | 980 | 2000/11/28 | 16:00 | 590 | 5 | 46:54 |
| 15 | 2001/03/29 | 10:26 | 942 | 2001/03/31 | 05:00 | 650 | 2 | 42:34 |
| 16 | 2001/04/10 | 05:30 | 2411 | 2001/04/11 | 22:00 | 670 | 2 | 40:30 |
| 17 | 2001/04/15 | 14:06 | 1199 | 2001/04/18 | 12:00 | 520 | 5 | 69:54 |
| 18 | 2001/08/14 | 16:01 | 618 | 2001/08/17 | 20:00 | 550 | 5 | 75:59 |
| 19 | 2001/09/28 | 08:54 | 846 | 2001/10/01 | 08:00 | 530 | 5 | 71:06 |
| 20 | 2001/10/19 | 16:50 | 901 | 2001/10/21 | 20:00 | 660 | 10 | 51:10 |
| 21 | 2001/11/04 | 16:35 | 1810 | 2001/11/06 | 13:00 | 700 | —* | 44:25 |
| 22 | 2001/11/22 | 23:30 | 1443 | 2001/11/24 | 14:00 | 730 | 10 | 38:30 |
| 23 | 2002/03/19 | 11:54 | 860 | 2002/03/23 | 21:00 | 440 | 15 | 105:06 |
| 24 | 2002/04/15 | 03:50 | 720 | 2002/04/17 | 16:00 | 600 | 15 | 66:10 |
| 25 | 2002/04/17 | 08:26 | 1240 | 2002/04/20 | 00:00 | 510 | 5 | 63:34 |
| 26 | 2002/05/08 | 13:50 | 614 | 2002/05/11 | 16:00 | 500 | 10 | 74:10 |
| 27 | 2002/05/22 | 00:06 | 1246 | 2002/05/23 | 20:00 | 730 | 17 | 38:00 |
| 28 | 2002/07/29 | 12:07 | 562 | 2002/08/01 | 09:00 | 454 | 10 | 68:53 |
| 29 | 2002/08/16 | 12:30 | 1585 | 2002/08/20 | 15:00 | 465 | 5 | 98:30 |
| 30 | 2002/09/05 | 16:54 | 1748 | 2002/09/08 | 04:00 | 500 | —* | 59:06 |
| 31 | 2003/05/28 | 00:50 | 1366 | 2003/05/29 | 13:00 | 650 | 5 | 36:10 |
| 32 | 2003/06/14 | 01:54 | 875 | 2003/06/17 | 07:00 | 480 | 8 | 77:06 |
| 33 | 2003/10/28 | 11:30 | 2459 | 2003/10/29 | 11:00 | 1300 | —* | 33:30 |
| | | | | | | | | (continue) |

TABLE 5.1 - Continuation

| | Date | Time | V_0 | Date | Time | V_f | ρ_{1AU} | t.t. |
|----|------------|-------|-------|------------|-------|-------|--------------|-------|
| 34 | 2003/10/29 | 20:54 | 2029 | 2003/10/31 | 02:00 | 1200 | 5 | 29:06 |
| 35 | 2003/11/18 | 08:50 | 1660 | 2003/11/20 | 10:00 | 700 | 6 | 49:10 |
| 36 | 2004/01/20 | 00:06 | 965 | 2004/01/22 | 08:00 | 560 | 4 | 56:00 |
| 37 | 2004/07/20 | 13:31 | 710 | 2004/07/22 | 18:00 | 560 | 5 | 52:29 |
| 38 | 2004/07/22 | 08:30 | 899 | 2004/07/24 | 14:00 | 580 | 5 | 53:30 |
| 39 | 2004/07/25 | 14:54 | 1333 | 2004/07/27 | 02:00 | 870 | 5 | 35:06 |
| 40 | 2004/11/04 | 23:30 | 1055 | 2004/11/07 | 22:00 | 630 | 10 | 70:30 |
| 41 | 2004/11/07 | 16:54 | 1759 | 2004/11/09 | 20:00 | 640 | 10 | 51:06 |
| 42 | 2005/01/20 | 06:54 | 882 | 2005/01/21 | 20:00 | 810 | —* | 37:06 |
| 43 | 2005/05/13 | 17:12 | 1128 | 2005/05/15 | 06:00 | 680 | 5 | 36:48 |

SOURCE: Manoharan (2007)

5.2.2 Insitu data - at distances lower than 1 AU

Some events have been selected where the ICME is detected at distances lower than 1 AU, (GOPALSWAMY et al., 2001) from the period between 1979 to 1984. In Table (5.2) the 7 events are described, where the columns give the date, time of occurrence (in universal time (UT)), initial velocity in km/s , (V_0). The ICME, final position where it is detected (X_f), the solar wind density (ρ_{1AU}) in $particles/cm^3$, the solar wind density at distance less than 1 AU (ρ_{xf}) in $particles/cm^3$ the ICME transit time ($t.t.$) in hours (see (GOPALSWAMY et al., 2001)).

5.2.3 Results - Satellite data

In this Section we present the results from the insitu data. We solved the model equations (Equations (4.13) and (4.16) giving as input the initial CME speed and changing iteratively the related parameters until the final speed (at 1 AU) were similar to the observed ICME speed. Table (5.3) shows the calculated transit time (t.t., in universal time (UT)), the final speed (km/s); and the parameters used to compute such speed. Each event has two rows one for laminar and one for turbulent solutions, subindex l and t , respectively.

TABLE 5.2 - CME and ICME events observed at distances lower than 1 AU [(*) values not measured].

| Date(CME) | Time | V_0 | Date(ICME) | Time | V_f | X_f | ρ_{X_f} | ρ_{1AU} | t.t. | Satellite |
|--------------------|-------|-------|---------------------|-------|-------|-------|--------------|--------------|-------|-----------|
| 1979/07/03 | 01:56 | 582 | 1979/07/05 | 15:00 | 470 | 0.84 | 5 | 3.5 | 61:04 | He |
| 1979/07/19 | 10:10 | 530 | 1979/07/21 | 22:00 | 362 | 0.72 | 15 | 7.7 | 59:50 | PVO |
| 1980/07/29 | 13:31 | 705 | 1980/08/01 | 16:00 | 409 | 0.91 | —* | —* | 74:29 | He |
| 1981/05/10 | 12:39 | 1420 | 1981/05/11 | 15:00 | 818 | 0.66 | —* | —* | 26:21 | He |
| 1981/05/13 | 04:15 | 1504 | 1981/05/14 | 12:00 | 702 | 0.63 | —* | —* | 31:45 | He |
| 1981/10/12 | 05:33 | 1002 | 1981/10/13 | 20:00 | 650 | 0.73 | 13 | 6.9 | 38:27 | PVO |
| 1984/02/16 | 09:36 | 1200 | 1984/02/17 | 13:00 | 798 | 0.73 | 15 | 7.9 | 27:24 | PVO |

SOURCE: Gopalswamy et al. (2001)

TABLE 5.3 - Calculated transit time, speed and parameters for ICMEs events at 1 AU.

| Values | | | Parameters | | | | |
|--------|------------|------------|----------------------|------|----------------------------|---------|---------------|
| | Calculated | Calculated | ν/C_d | p | Mass ($\times 10^{15}$)g | Density | V_{sw} km/s |
| | t.t. | Speed | | | | | |
| 1_l | 42:16 | 806 | 3.2×10^{21} | 0.78 | 9.5 | 10.9 | 600 |
| 1_t | 48:04 | 630 | 2.6×10^4 | 0.80 | 9.6 | 9.4 | 373 |
| 2_l | 45:39 | 774 | 3.2×10^{21} | 0.80 | 9.3 | 5.0 | 600 |
| 2_t | 50:26 | 631 | 2.8×10^4 | 0.81 | 9.8 | 10.2 | 400 |
| 3_l | 73:44 | 499 | 3.2×10^{21} | 0.74 | 9.8 | 10.2 | 400 |
| 3_t | 71:59 | 500 | 2.4×10^4 | 0.81 | 9.8 | 9.8 | 386 |
| 4_l | 60:18 | 608 | 3.2×10^{21} | 0.79 | 6.6 | 5.5 | 600 |
| 4_t | 79:46 | 425 | 1.9×10^4 | 0.84 | 9.6 | 9.6 | 386 |
| 5_l | 46:12 | 752 | 3.4×10^{21} | 0.80 | 9.8 | 5.4 | 600 |
| 5_t | 53:25 | 580 | 2.7×10^4 | 0.82 | 9.6 | 4.6 | 373 |
| 6_l | 61:25 | 619 | 3.2×10^{21} | 0.71 | 5.0 | 5.0 | 666 |
| 6_t | 60:50 | 621 | 2.6×10^4 | 0.78 | 7.0 | 3.6 | 386 |
| 8_l | 88:59 | 371 | 2.9×10^{21} | 0.82 | 8.3 | 4.4 | 380 |
| 8_t | 89:39 | 405 | 1.7×10^4 | 0.85 | 10 | 3.7 | 656 |
| 9_l | 64:38 | 565 | 3.2×10^{21} | 0.76 | 9.5 | 5.4 | 400 |
| 9_t | 62:17 | 572 | 2.5×10^4 | 0.80 | 9.6 | 4.6 | 360 |
| | | | | | | | (continue) |

TABLE 5.3 - Continuation

| | Calculated | Calculated | ν/C_d | p | Mass($\times 10^{15}$)g | Density | V_{sw} km/s |
|-----------------|------------|------------|----------------------|------|---------------------------|---------|---------------|
| 11 _l | 78:01 | 509 | 3.8×10^{21} | 0.79 | 9.8 | 1.7 | 400 |
| 11 _t | 70:59 | 516 | 2.4×10^4 | 0.83 | 9.6 | 1.7 | 386 |
| 12 _l | 91:09 | 360 | 3.4×10^{21} | 0.81 | 8.5 | 4.8 | 371 |
| 12 _t | 85:19 | 403 | 2.7×10^4 | 0.84 | 1.0 | 4.8 | 279 |
| 13 _l | 79:22 | 438 | 3.2×10^{21} | 0.80 | 9.5 | 3.9 | 440 |
| 13 _t | 85:26 | 407 | 2.1×10^4 | 0.90 | 7.0 | 0.9 | 377 |
| 14 _l | 48:48 | 740 | 3.2×10^{21} | 0.79 | 9.5 | 5.0 | 600 |
| 14 _t | 54:45 | 598 | 2.6×10^4 | 0.82 | 9.8 | 4.6 | 386 |
| 18 _l | 62:39 | 612 | 3.4×10^{21} | 0.74 | 9.8 | 5.4 | 600 |
| 18 _t | 66:37 | 553 | 2.5×10^4 | 0.80 | 9.8 | 4.6 | 386 |
| 19 _l | 53:55 | 681 | 3.4×10^{21} | 0.79 | 9.5 | 4.6 | 600 |
| 19 _t | 62:01 | 536 | 2.5×10^4 | 0.82 | 9.6 | 4.6 | 373 |
| 23 _l | 57:30 | 636 | 3.2×10^{21} | 0.77 | 9.8 | 15.4 | 600 |
| 23 _t | 76:40 | 441 | 2.3×10^4 | 0.82 | 9.6 | 14.6 | 386 |
| 24 _l | 56:03 | 676 | 3.2×10^{21} | 0.72 | 9.5 | 16.3 | 600 |
| 24 _t | 59:54 | 600 | 2.7×10^4 | 0.79 | 9.8 | 14.6 | 386 |
| 26 _l | 63:12 | 606 | 3.2×10^{21} | 0.74 | 9.8 | 11.0 | 600 |
| 26 _t | 71:44 | 500 | 2.5×10^4 | 0.81 | 9.8 | 14.6 | 386 |
| 27 _l | 40:42 | 868 | 3.2×10^{21} | 0.75 | 9.5 | 17.2 | 600 |
| 27 _t | 43:43 | 733 | 2.8×10^4 | 0.79 | 9.8 | 16.6 | 373 |
| 28 _l | 81:15 | 453 | 3.2×10^{21} | 0.70 | 9.5 | 10.2 | 400 |
| 28 _t | 79:03 | 456 | 2.1×10^4 | 0.82 | 9.8 | 9.5 | 386 |
| 32 _l | 55:16 | 659 | 3.2×10^{21} | 0.78 | 9.5 | 9.1 | 600 |
| 32 _t | 68:57 | 480 | 2.5×10^4 | 0.82 | 9.8 | 7.9 | 386 |
| 35 _l | 36:59 | 894 | 3.2×10^{21} | 0.81 | 9.8 | 6.1 | 600 |
| 35 _t | 41:06 | 711 | 2.7×10^4 | 0.81 | 9.8 | 5.8 | 360 |
| 36 _l | 50:16 | 716 | 3.4×10^{21} | 0.80 | 9.5 | 3.9 | 600 |
| 36 _t | 57:51 | 560 | 2.5×10^4 | 0.82 | 9.6 | 3.9 | 373 |
| 37 _l | 57:22 | 659 | 3.4×10^{21} | 0.77 | 9.8 | 5.0 | 600 |
| 37 _t | 62:41 | 565 | 2.5×10^4 | 0.81 | 9.8 | 4.6 | 386 |
| 38 _l | 51:03 | 716 | 3.2×10^{21} | 0.79 | 9.2 | 5.0 | 600 |
| 38 _t | 56:42 | 587 | 2.6×10^4 | 0.81 | 9.6 | 4.6 | 373 |
| | | | | | | | (continue) |

TABLE 5.3 - Continuation

| | Calculated | Calculated | ν/C_d | p | Mass($\times 10^{15}$)g | Density | V_{sw} km/s |
|--------|------------|------------|----------------------|------|---------------------------|---------|---------------|
| 39_l | 36:24 | 978 | 3.4×10^{21} | 0.79 | 9.8 | 5.0 | 600 |
| 39_t | 37:10 | 887 | 2.7×10^4 | 0.80 | 9.8 | 4.6 | 346 |
| 40_l | 46:18 | 775 | 3.2×10^{21} | 0.77 | 9.5 | 10.5 | 600 |
| 40_t | 51:22 | 631 | 2.7×10^4 | 0.80 | 9.8 | 9.8 | 373 |
| 42_l | 46:39 | 809 | 3.2×10^{21} | 0.73 | 9.5 | 5.4 | 400 |
| 42_t | 45:44 | 814 | 2.6×10^4 | 0.78 | 9.3 | 4.6 | 386 |
| 43_l | 43:34 | 818 | 3.2×10^{21} | 0.79 | 9.5 | 5.0 | 600 |
| 43_t | 46:49 | 694 | 2.6×10^4 | 0.80 | 9.8 | 4.6 | 386 |

For a better comparison we present in Table (5.4) the values of transit time and ICME speed obtained with the model and the observed values for ICMEs events at 1 AU:

TABLE 5.4 - Calculated and observed transit time and speed for ICMEs events at 1 AU for laminar (first line for each number) and turbulent regime (second line for each number).

| Values | | | | |
|--------|------------|----------|--------------|------------|
| | Calculated | Observed | Calculated | Observed |
| | t.t. (UT) | | Speed (km/s) | |
| 1 | 42:16 | 57:01 | 806 | 621 |
| | 48:04 | | 630 | |
| 2 | 45:39 | 79:16 | 774 | 620 |
| | 50:26 | | 631 | |
| 3 | 73:44 | 60:54 | 499 | 500 |
| | 71:59 | | 500 | |
| 4 | 60:18 | 54:30 | 608 | 425 |
| | 79:46 | | 425 | |
| 5 | 46:12 | 39:28 | 752 | 570 |
| | 53:25 | | 580 | |
| 6 | 61:25 | 58:10 | 619 | 620 |
| | 60:50 | | 621 | |
| 8 | 88:59 | 51:06 | 371 | 400 |
| | 89:39 | | 405 | |
| | | | | (continue) |

TABLE 5.4 - Continuation

| | Calculated | Observed | Calculated | Observed |
|----|------------|----------|------------|------------|
| 9 | 64:38 | 60:30 | 565 | 567 |
| | 62:17 | | 572 | |
| 11 | 78:01 | 91:10 | 509 | 510 |
| | 70:59 | | 516 | |
| 12 | 91:09 | 84:10 | 360 | 395 |
| | 85:19 | | 403 | |
| 13 | 79:22 | 84:34 | 438 | 400 |
| | 85:26 | | 407 | |
| 14 | 48:48 | 46:54 | 740 | 590 |
| | 54:45 | | 598 | |
| 18 | 62:39 | 75:59 | 612 | 550 |
| | 66:37 | | 553 | |
| 19 | 53:55 | 71:06 | 681 | 530 |
| | 62:01 | | 536 | |
| 23 | 57:30 | 105:06 | 636 | 440 |
| | 76:40 | | 441 | |
| 24 | 56:03 | 66:10 | 676 | 600 |
| | 59:54 | | 600 | |
| 26 | 63:12 | 74:10 | 606 | 500 |
| | 71:44 | | 500 | |
| 27 | 40:42 | 38:00 | 868 | 730 |
| | 43:43 | | 733 | |
| 28 | 81:15 | 68:53 | 453 | 454 |
| | 79:03 | | 456 | |
| 32 | 55:16 | 77:06 | 659 | 480 |
| | 68:57 | | 480 | |
| 35 | 36:59 | 49:10 | 894 | 700 |
| | 41:06 | | 711 | |
| 36 | 50:16 | 56:00 | 716 | 560 |
| | 57:51 | | 560 | |
| 37 | 57:22 | 52:29 | 659 | 560 |
| | 62:41 | | 565 | |
| | | | | (continue) |

TABLE 5.4 - Continuation

| | Calculated | Observed | Calculated | Observed |
|----|------------|----------|------------|----------|
| 38 | 51:03 | 53:30 | 716 | 580 |
| | 56:42 | | 587 | |
| 39 | 36:24 | 35:06 | 978 | 870 |
| | 37:10 | | 887 | |
| 40 | 46:18 | 70:30 | 775 | 630 |
| | 51:22 | | 631 | |
| 42 | 46:39 | 37:06 | 809 | 810 |
| | 45:44 | | 814 | |
| 43 | 43:34 | 36:48 | 818 | 680 |
| | 46:49 | | 694 | |

In a similar way, Table (5.5) shows the calculated distance (in AU), transit time (t.t., in universal time (UT)), speed (km/s) and parameters for the ICMEs events observed at distances lower than 1 AU.

TABLE 5.5 - Calculated distance, transit time, speed and parameters for ICMEs events at distances lower than 1 AU.

| Values | | | | Parameters | | | | |
|--------|------------|------------|------------|----------------------|------|----------------------------|-------|---------------|
| | Calculated | Calculated | Calculated | C_d/ν | p | Mass ($\times 10^{15}$)g | Dens. | V_{sw} km/s |
| | Distance | t.t. | Speed | | | | | |
| 1_t | 0.84 | 63:07 | 470 | 2.2×10^4 | 0.83 | 9.6 | 4.8 | 386 |
| 1_l | 0.84 | 65:09 | 464 | 3.3×10^{21} | 0.77 | 9.7 | 5.0 | 392 |
| 2_t | 0.72 | 61:13 | 374 | 1.5×10^4 | 0.82 | 5.3 | 7.9 | 333 |
| 2_l | 0.72 | 66:43 | 352 | 2.8×10^{21} | 0.75 | 9.2 | 14.3 | 320 |
| 3_t | 0.91 | 75:15 | 412 | 6.2×10^4 | 0.86 | 5.2 | 3.7 | 368 |
| 3_l | 0.66 | 78:32 | 407 | 3.4×10^{21} | 0.79 | 9.8 | 7.4 | 392 |
| 4_t | 0.66 | 23:58 | 836 | 2.7×10^4 | 0.80 | 9.8 | 6.7 | 352 |
| 4_l | 0.66 | 25:33 | 811 | 3.4×10^{21} | 0.79 | 9.8 | 7.4 | 392 |
| 5_t | 0.63 | 25:36 | 704 | 2.7×10^4 | 0.80 | 9.8 | 7.1 | 384 |
| 5_l | 0.63 | 26:40 | 694 | 3.4×10^{21} | 0.80 | 9.9 | 7.4 | 392 |
| 6_t | 0.73 | 36:01 | 652 | 2.7×10^4 | 0.79 | 9.8 | 12.8 | 376 |
| 6_l | 0.73 | 37:42 | 644 | 3.3×10^{21} | 0.76 | 9.7 | 12.6 | 392 |
| 7_t | 0.73 | 29:21 | 800 | 2.7×10^4 | 0.80 | 9.8 | 14.7 | 368 |
| 7_l | 0.73 | 30:46 | 791 | 3.2×10^{21} | 0.75 | 9.6 | 14.9 | 392 |

For a better comparison we present in Table (5.6) the values of transit time and ICME speed obtained with the model and the observed values for ICMEs events at distances lower than 1 AU:

TABLE 5.6 - Calculated and observed distance, transit time, and speed for ICMEs events at distance lower than 1 AU for laminar (first line for each number) and turbulent regime (second line for each number).

| Values | | | | |
|--------|------------|----------|--------------|----------|
| | Calculated | Observed | Calculated | Observed |
| | t.t. (UT) | | Speed (km/s) | |
| 1 | 63:07 | 61:04 | 470 | 470 |
| | 65:09 | | 464 | |
| 2 | 61:13 | 59:50 | 374 | 362 |
| | 66:43 | | 352 | |
| 3 | 75:15 | 74:29 | 412 | 409 |
| | 78:32 | | 407 | |
| 4 | 23:58 | 26:21 | 836 | 818 |
| | 25:33 | | 811 | |
| 5 | 25:36 | 31:45 | 704 | 702 |
| | 26:40 | | 694 | |
| 6 | 36:01 | 38:27 | 652 | 650 |
| | 37:42 | | 644 | |
| 7 | 29:21 | 27:24 | 800 | 798 |
| | 30:46 | | 791 | |

5.3 Type II burst data

Type II bursts are produced when a disturbing agent is traveling, at relatively moderate speeds, through the solar atmosphere. This agent disturbs the ambient plasma which radiates electromagnetic emission at the plasma frequency. The agent may be a blast wave produced by a flare or a shock wave driven by a CME. At metric wavelengths, both mechanisms are plausible. Although at hectometric-decimetric and kilometric wavelengths, it is generally accepted that the agent is a shock wave driven by an ICME (LARA; BORGAZZI, 2008) (see Appendix (C)) for more details).

The WAVE/WIND (BOUGERET et al., 1995) radio receivers provide, since 1998, observations on both decametric (DH) and kilometric (km) type II burst. The list of DH Type II burst, given in Table (5.7), was obtained from the online catalog of

the Wind/WAVES experiment, for more details see (GOPALSWAMY et al., 2005). The DH and km Type II burst were observed by the RAD2 (1.075 - 13.825 MHz) and RAD1 (20 - 1040 KHz). The RAD2 spectral range correspond to 21.7 to 279 m (decametric, hectometric and metric or DH wavelength range). The spectral range of the RAD1 receiver starts in the hectometric range (288.5 m) and ends in the km domain (15 km).

Table (5.7) shows the Type II events selected in the 2000 to 2004 period, based on Zhang et al. (2007). All of these 15 events are related with CME/ICME events, presented in Table (5.1). The first column represents the associated number of each event given in Table (5.1), the second and third columns represent the date and time of occurrence (in UT) for the decametric-kilometric Type II burst, and in the last column F_s (in MHz) are the observed frequency ranges. For all the 15 events we have considered the origin of the system located at $2 R_{\odot}$ from the Sun surface, distance that corresponds with the place where the DH Type II bursts start.

As was mentioned in chapter (4), the model developed assumes an origin or range of validity that starts at about $30 R_{\odot}$. In this case and as the Type II data are obtained at $2 R_{\odot}$, we consider an extrapolation of the model to low distances. In this way it is possible to compare the curves of the model with the Type II burst data.

TABLE 5.7 - Type II burts events.

| | Date | Time | F_s |
|----|------------|-------|---------|
| 7 | 2000/07/14 | 10:30 | 14-0.08 |
| 10 | 2000/09/16 | 04:30 | 14-0.4 |
| 15 | 2001/03/29 | 10:12 | 4-0.06 |
| 16 | 2001/04/10 | 05:24 | 14-0.1 |
| 17 | 2001/04/15 | 14:05 | 14-0.04 |
| 20 | 2001/10/19 | 16:45 | 14-1.3 |
| 21 | 2001/11/04 | 16:30 | 14-0.07 |
| 22 | 2001/11/22 | 22:40 | 14-0.04 |
| 25 | 2002/04/17 | 08:30 | 5-0.04 |
| 29 | 2002/08/16 | 12:20 | 14-0.06 |
| 30 | 2002/09/05 | 16:55 | 16-0.03 |
| 31 | 2003/05/28 | 01:00 | 1-0.2 |
| 33 | 2003/10/28 | 11:10 | 14-0.04 |
| 34 | 2003/10/29 | 20:55 | 11-0.05 |
| 41 | 2004/11/07 | 16:25 | 14-0.06 |

5.4 Method: Type II burst-ICME speed versus position

Equations (4.13) and (4.16) give the ICME instantaneous speed as a function of position. To get the ICME position as a function of time, we have divided the interval (1 AU) in 4096 equally spaced sectors, computed the mean speed in each sector and then, computed the time assuming constant speed in each sector. Once we had the ICME position as a function of time, we were able to obtain the density by assuming Leblanc's density model, Equation (4.11). And then, the plasma frequency ($f \sim \sqrt{\rho}$) as a function of time. In this way, we can compare our results against the observed Type II behavior.

5.4.1 Results - Type II burst data

Using the methodology presented in Section (5.4), we are able to trace the ICME trajectory in a frequency-time diagram. In this section we show the plots of frequency versus time for the 15 Type II burst events in the kilometric and decametric frequency range. The 15 Type II burst events were classified in three categories (good, regular, and questionable) depending on the quality of the results obtained. In Figure (5.1 a) is presented, as an example, the event of September 5, 2000 (good event, in the kilometric range). The Type II burst structure is denoted by the arrows in the figure.

The comparison with our model is denoted by the continuous lines for the laminar regime and the dotted line for the turbulent regime, the bottom pair of lines correspond to the fundamental frequency and the upper pair correspond to the first harmonic. We observed that the theoretical curves of our model have a similar drift to the Type II burst drift. It is possible to see two Type III burst structures (denoted by arrows in the same figure). The difference between the Type II and the Type III bursts is basically that the frequencies in the Type III burst have an abrupt drift in time; on the other hand the frequencies in the Type II burst have a more slow drift in time, (see Figure (5.1 a)).

The same description can be made for the other events in the kilometric and decametric frequency range. Figure (5.1 b) presents the same event (September 5, 2002) but for the decametric frequency range. Figures (5.2a) and (5.2 b) show an example for a regular event, in this case November 4, 2001. Figures (5.3 a) and (5.3 b) show, an example of a questionable event (May 28, 2003). In all the figures the title denotes

the date and start times for each event.

Table (5.8) shows the calculated transit time (t.t., in universal time (UT)), speed (km/s) and parameters for the ICMEs events in the case of Type II burst.

TABLE 5.8 - Calculated transit time, speed and parameters for Type II burst events.

| | t.t. | Speed | ν/C_d | p | Mass ($\times 10^{15}$)g | Density | V_{sw} km/s |
|--------|-------|-------|----------------------|------|----------------------------|---------|---------------|
| 7_l | 38:33 | 982 | 3.3×10^{21} | 0.77 | 9.6 | 5.1 | 400 |
| 7_t | 34:25 | 995 | 2.7×10^4 | 0.80 | 9.6 | 4.8 | 346 |
| 10_l | 50:51 | 753 | 3.3×10^{21} | 0.77 | 9.3 | 3.9 | 400 |
| 10_t | 46:07 | 760 | 2.8×10^4 | 0.80 | 9.6 | 3.9 | 373 |
| 15_l | 52:09 | 765 | 3.4×10^{21} | 0.78 | 9.8 | 2.1 | 600 |
| 15_t | 54:28 | 670 | 2.7×10^4 | 0.82 | 9.8 | 1.7 | 386 |
| 16_l | 39:14 | 899 | 3.8×10^{21} | 0.84 | 9.8 | 1.7 | 600 |
| 16_t | 39:30 | 733 | 2.7×10^4 | 0.83 | 9.8 | 1.7 | 360 |
| 17_l | 54:03 | 716 | 3.2×10^{21} | 0.78 | 9.3 | 5.0 | 600 |
| 17_t | 63:35 | 529 | 2.5×10^4 | 0.83 | 9.8 | 4.6 | 386 |
| 20_l | 52:48 | 761 | 3.2×10^{21} | 0.72 | 9.5 | 10.9 | 600 |
| 20_t | 55:55 | 662 | 2.7×10^4 | 0.79 | 9.8 | 9.8 | 373 |
| 21_l | 41:15 | 905 | 3.2×10^{21} | 0.78 | 9.8 | 7.2 | 600 |
| 21_t | 43:45 | 711 | 2.7×10^4 | 0.80 | 9.8 | 6.9 | 346 |
| 22_l | 43:09 | 894 | 3.2×10^{21} | 0.75 | 9.8 | 11.3 | 600 |
| 22_t | 45:39 | 732 | 2.6×10^4 | 0.79 | 9.6 | 9.8 | 386 |
| 25_l | 54:11 | 712 | 3.2×10^{21} | 0.78 | 9.3 | 5.4 | 600 |
| 25_t | 64:43 | 518 | 2.8×10^4 | 0.82 | 9.8 | 4.6 | 386 |
| 29_l | 54:07 | 695 | 3.2×10^{21} | 0.80 | 9.6 | 5.4 | 600 |
| 29_t | 70:34 | 471 | 2.4×10^4 | 0.84 | 9.8 | 4.6 | 386 |
| 30_l | 50:58 | 729 | 3.2×10^{21} | 0.79 | 9.6 | 7.2 | 600 |
| 30_t | 63:51 | 505 | 2.7×10^4 | 0.82 | 9.6 | 6.9 | 386 |
| 31_l | 46:27 | 828 | 3.4×10^{21} | 0.78 | 9.8 | 5.0 | 600 |
| 31_t | 50:04 | 662 | 2.7×10^4 | 0.81 | 9.8 | 4.6 | 386 |
| 33_l | 26:31 | 1425 | 3.7×10^{21} | 0.77 | 9.8 | 7.2 | 600 |
| 33_t | 25:29 | 1291 | 2.8×10^4 | 0.79 | 9.8 | 7.2 | 373 |
| 34_l | 37:27 | 988 | 3.4×10^{21} | 0.79 | 9.6 | 5.4 | 600 |
| 34_t | 37:36 | 830 | 2.7×10^4 | 0.81 | 9.8 | 4.6 | 386 |
| 41_l | 44:09 | 846 | 3.2×10^{21} | 0.77 | 9.4 | 9.8 | 600 |
| 41_t | 48:37 | 641 | 2.7×10^4 | 0.80 | 9.6 | 9.8 | 360 |

For a better comparison we presente in Table (5.9) the values of transit time and ICME speed obtained with the model and the observed values for Type II burst:

TABLE 5.9 - Calculated and observed transit time, speed for Type II bursts events for laminar (first line for each number) and turbulent regime (second line for each number).

| | t.t. (Calculated) | Observed | Speed (Calculated) | Observed |
|----|-------------------|----------|--------------------|----------|
| 7 | 38:33 | 32:06 | 982 | 990 |
| | 34:25 | | 995 | |
| 10 | 50:51 | 39:32 | 753 | 760 |
| | 46:07 | | 760 | |
| 15 | 52:09 | 42:34 | 765 | 650 |
| | 54:28 | | 670 | |
| 16 | 39:14 | 40:30 | 899 | 670 |
| | 39:30 | | 733 | |
| 17 | 54:03 | 69:54 | 716 | 520 |
| | 63:35 | | 529 | |
| 20 | 52:48 | 51:10 | 761 | 660 |
| | 55:55 | | 662 | |
| 21 | 41:15 | 44:25 | 905 | 700 |
| | 43:45 | | 711 | |
| 22 | 43:09 | 38:30 | 894 | 730 |
| | 45:39 | | 732 | |
| 25 | 54:11 | 63:34 | 712 | 510 |
| | 64:43 | | 518 | |
| 29 | 54:07 | 98:30 | 695 | 465 |
| | 70:34 | | 471 | |
| 30 | 50:58 | 59:06 | 729 | 500 |
| | 63:51 | | 505 | |
| 31 | 46:27 | 36:10 | 828 | 650 |
| | 50:04 | | 662 | |
| 33 | 26:31 | 33:30 | 1425 | 1300 |
| | 25:29 | | 1291 | |
| 34 | 37:27 | 29:06 | 988 | 1200 |
| | 37:36 | | 830 | |
| 41 | 44:09 | 51:06 | 846 | 640 |
| | 48:37 | | 641 | |

Figures (5.4) and (5.5) show in the different panels (a) November 22, 2001, b) October 19, 2001, c) November 7, 2004, d) April 17, 2002, e) September 16, 2000) the cases for good events in the kilometric and decametric frequency range respectively.

Regular events are showed in Figures (5.6) and (5.7) for the kilometric and decametric frequency range; panels are: a) August 16, 2002, b) March 29, 2001, c) April

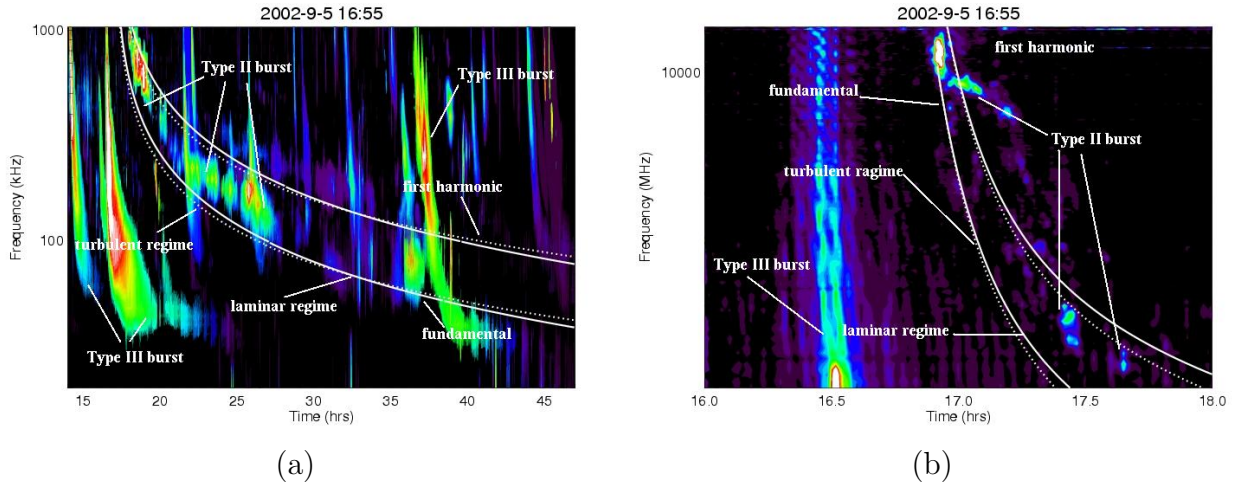


FIGURE 5.1 - a) Kilometric (km) type II bursts event (good), September 5, 2002. Model: Turbulent regime (dotted line, fundamental and first harmonic), Laminar regime (continuous line, fundamental and first harmonic). b) Decametric (DH) type II bursts event (good), September 5, 2002. Model: Turbulent regime (dotted line, fundamental and first harmonic), Laminar regime (continuous line, fundamental and first harmonic).

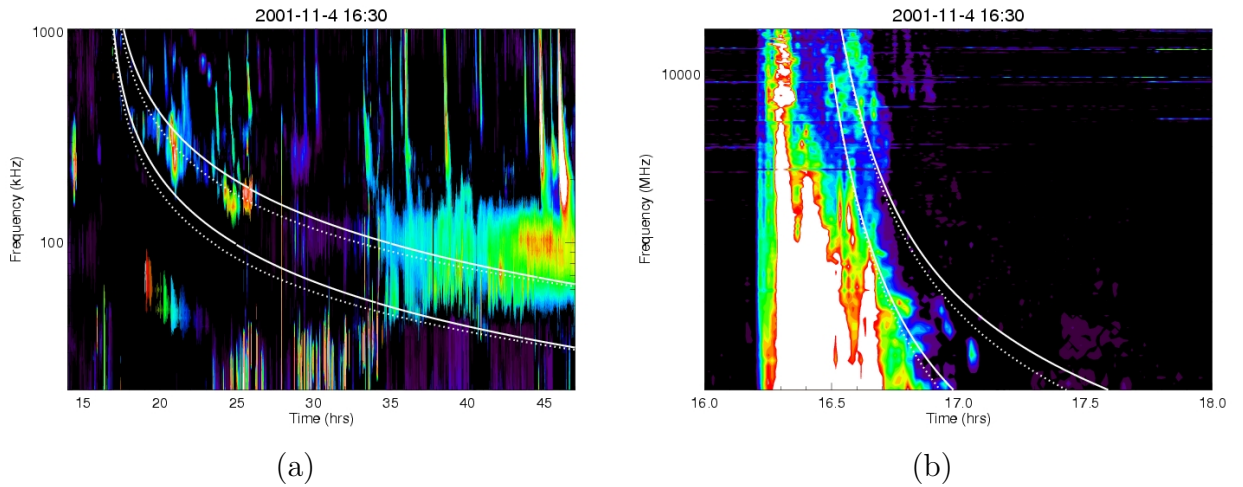
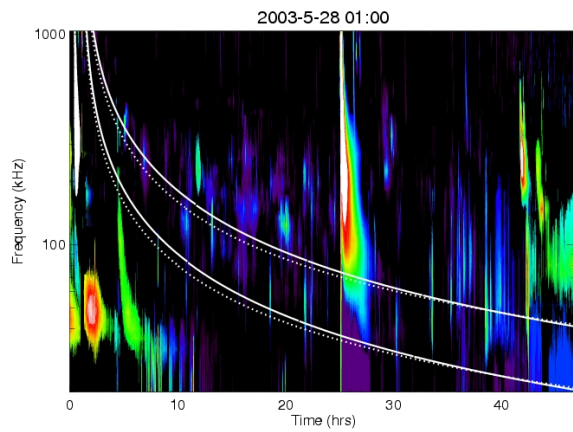


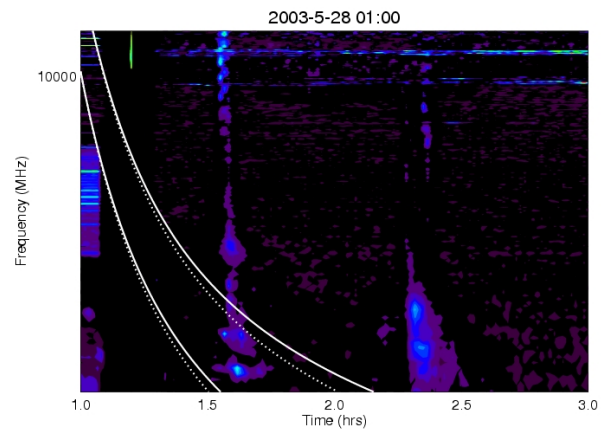
FIGURE 5.2 - a) Kilometric (km) type II bursts event (regular), November 4, 2001. Model: Turbulent regime (dotted line, fundamental and first harmonic), Laminar regime (continuous line, fundamental and first harmonic). b) Decametric (DH) type II bursts event (regular), November 4, 2001. Model: Turbulent regime (dotted line, fundamental and first harmonic), Laminar regime (continuous line, fundamental and first harmonic).

15, 2001, d) July 14, 2000, e) October 29, 2000.

Figures (5.8) and (5.9) show questionable events in panels: a) October 28, 2003, b) April 10, 2001, examples in the kilometric and decametric frequency range.



(a)



(b)

FIGURE 5.3 - a) Kilometric (km) type II burts event (questionable), May 28, 2003. Model: Turbulent regime (dotted line, fundamental and first harmonic), Laminar regime (continuous line, fundamental and first harmonic). b) Decametric (DH) type II burts event (questionable), May 28, 2003. Model: Turbulent regime (dotted line, fundamental and first harmonic), Laminar regime (continuous line, fundamental and first harmonic).

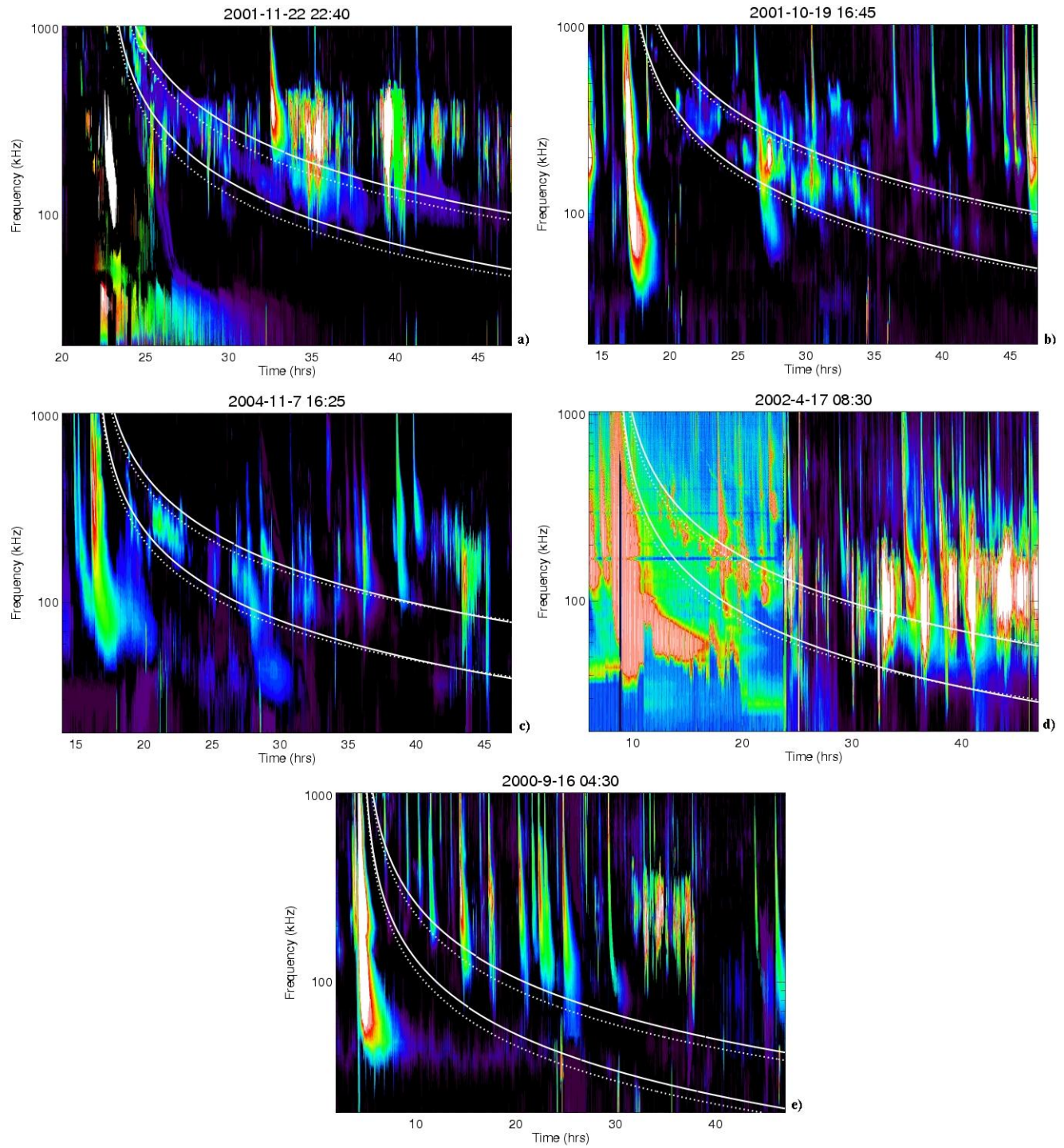


FIGURE 5.4 - Kilometric (km) type II burts event (good), a) November 22, 2001, b) October 19, 2001, c) November 7, 2004, d) April 17, 2002, e) September 16, 2000. Model: Turbulent regime (dotted line, fundamental and first harmonic), Laminar regime (continuous line, fundamental and first harmonic).

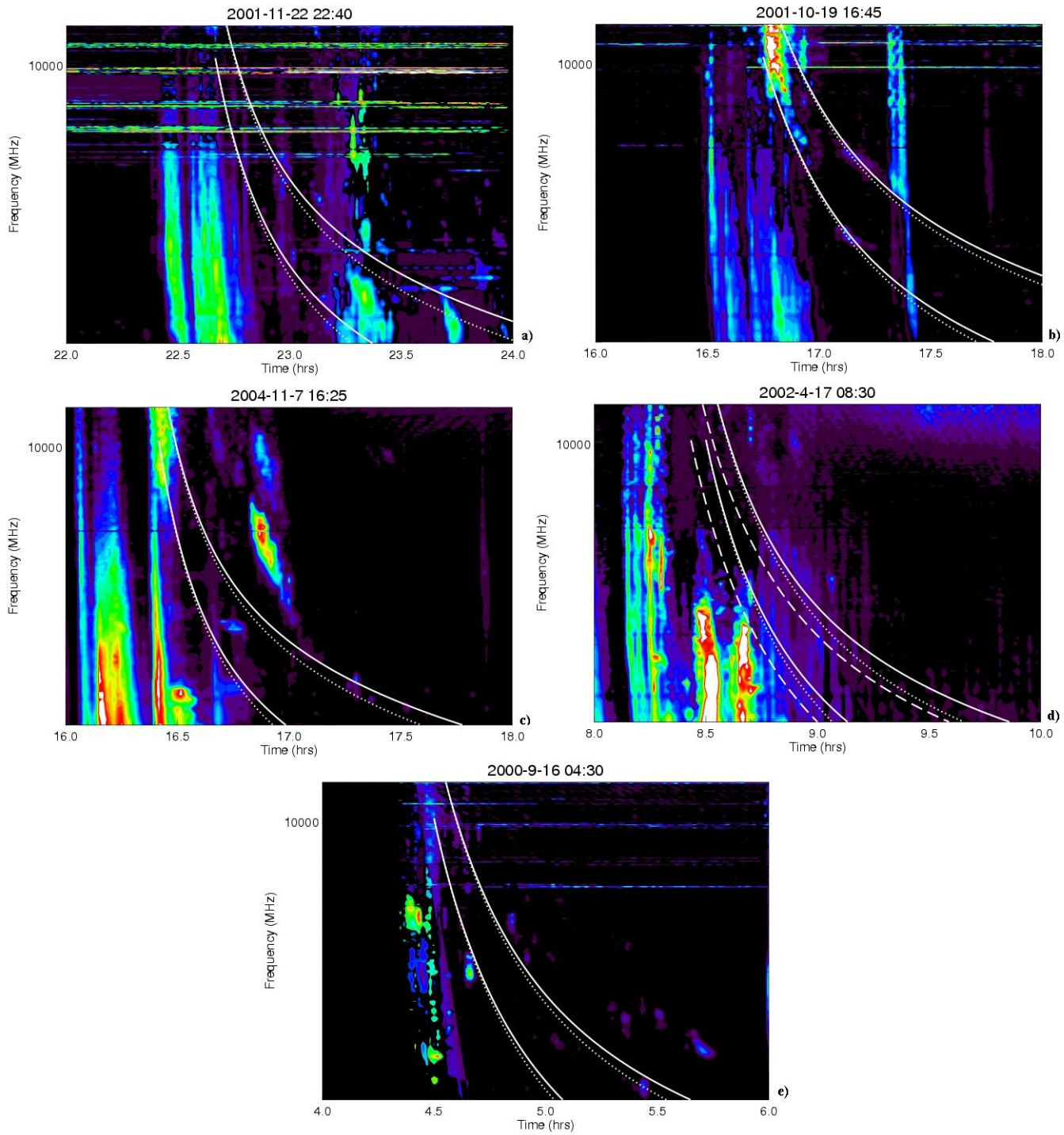


FIGURE 5.5 - Decametric (DH) type II bursters event (good), a) November 22, 2001, b) October 19, 2001, c) November 7, 2004, d) April 17, 2002, e) September 16, 2000. Model: Turbulent regime (dotted line, fundamental and first harmonic), Laminar regime (continuous line, fundamental and first harmonic).

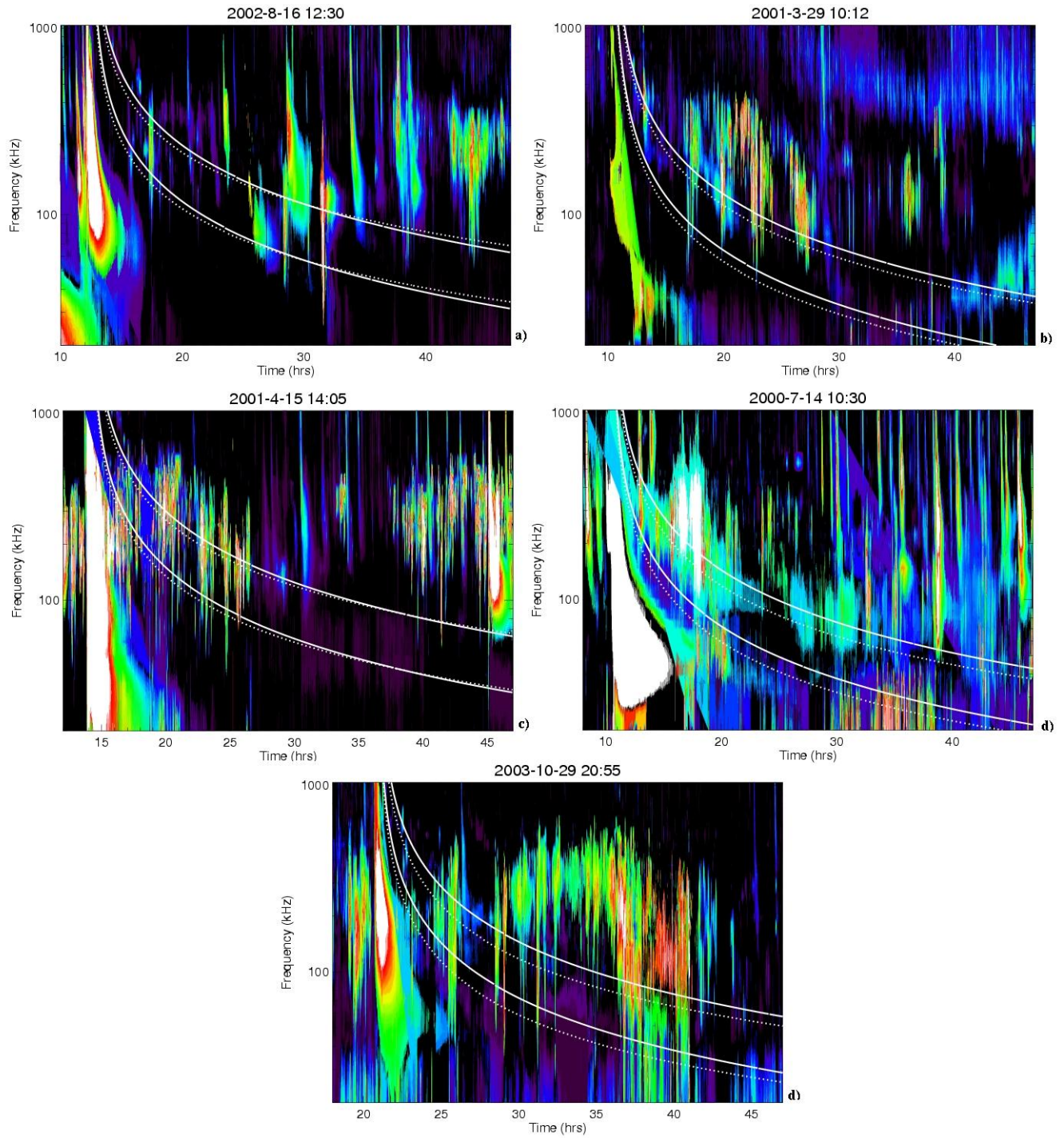


FIGURE 5.6 - Kilometric (km) type II burts event (regulars), a) August 16, 2002, b) March 29, 2001, c) April 15, 2001, d) July 14, 2000, e) October 29, 2003. Model: Turbulent regime (dotted line, fundamental and first harmonic), Laminar regime (continuous line, fundamental and first harmonic).

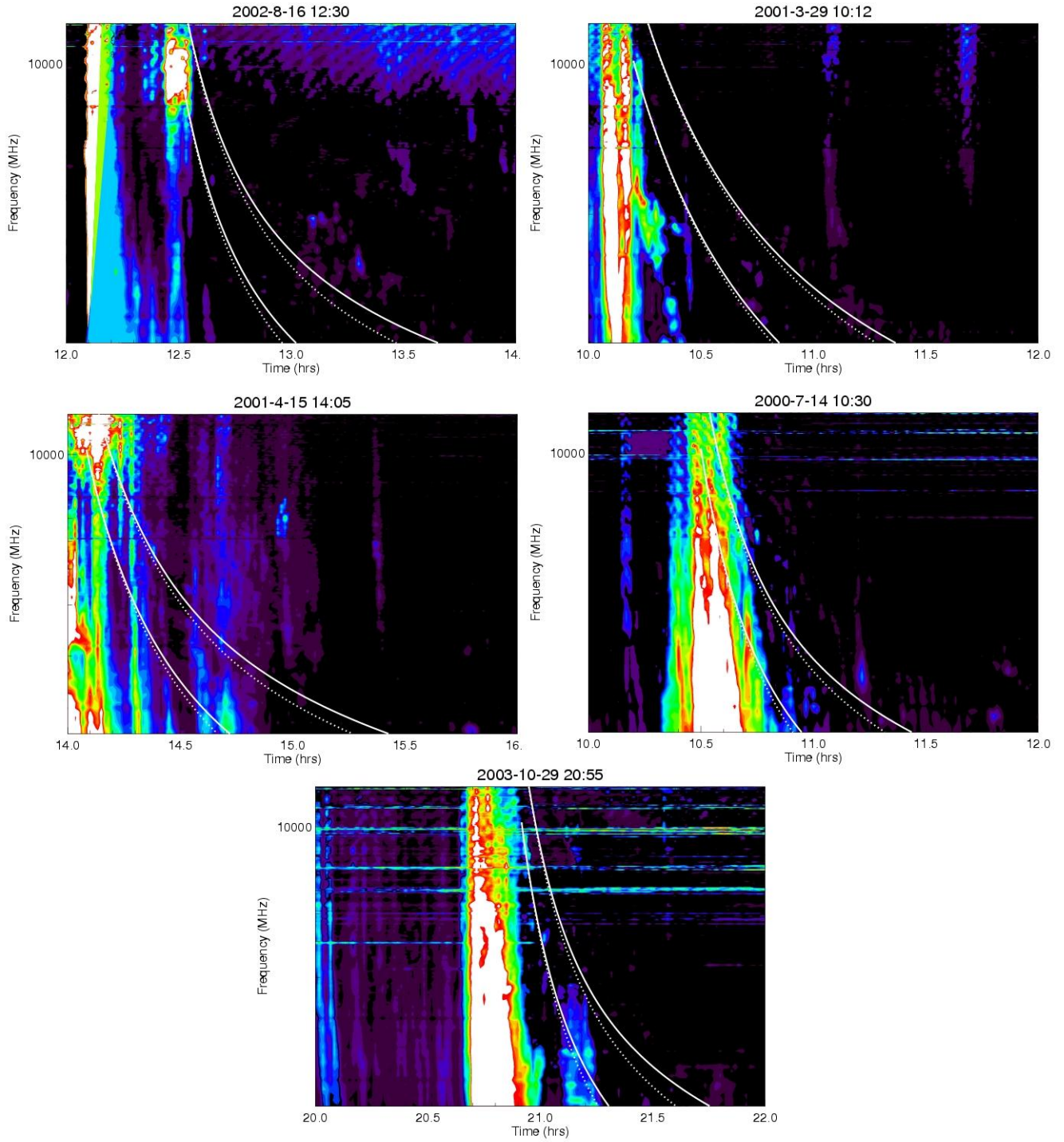


FIGURE 5.7 - Decametric (DH) type II burts event (regulars), a) August 16, 2002, b) March 29, 2001, c) April 15, 2001, d) July 14, 2000, e) October 29, 2003. Model: Turbulent regime (dotted line, fundamental and first harmonic), Laminar regime (continuous line, fundamental and first harmonic).

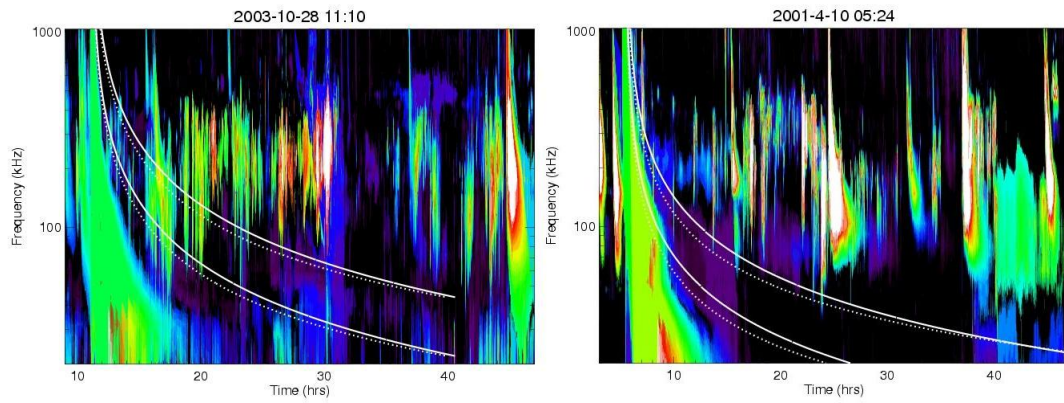


FIGURE 5.8 - Kilometric (km) type II burts event (questionables), a) October 28, 2003, b) April 10, 2001. Model: Turbulent regime (dotted line, fundamental and first harmonic), Laminar regime (continuous line, fundamental and first harmonic).

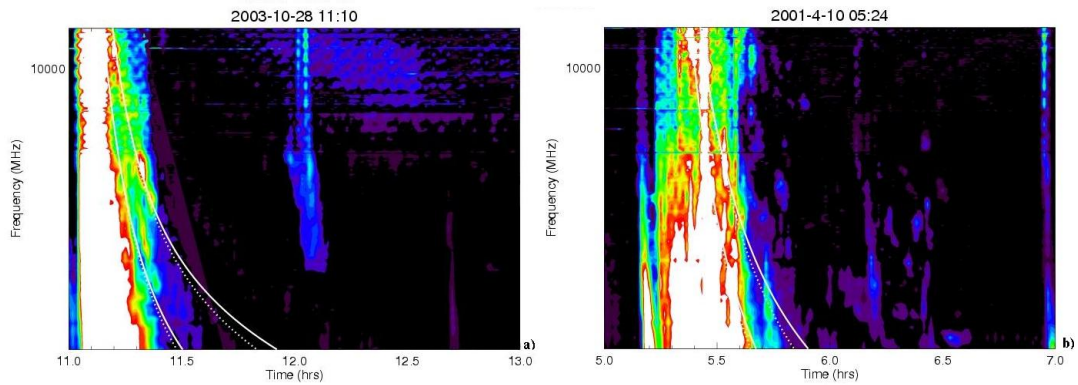


FIGURE 5.9 - Decametric (DH) type II burts event (questionables), a) October 28, 2003, b) April 10, 2001. Model: Turbulent regime (dotted line, fundamental and first harmonic), Laminar regime (continuous line, fundamental and first harmonic).

6 RESULTS AND DISCUSSION

In this chapter we present the discussion of the results obtained in the analysis of chapters (4) and (5). The discussion is divided in sections depending on the topic.

6.1 Results for the events detected by satellites at 1 AU

Given an initial CME speed we iteratively adjust the parameters of the model, in order to obtain the observed final ICME speed. We are able to study the statistical behavior of these parameters.

Figures (6.1), (6.2), (6.3), (6.4), and (6.5) show the histograms for the coefficients ν , C_d , radial exponent p , mass m_{cme} , density, and solar wind velocity V_{sw} using the values of Table (5.3) for satellites at 1 AU.

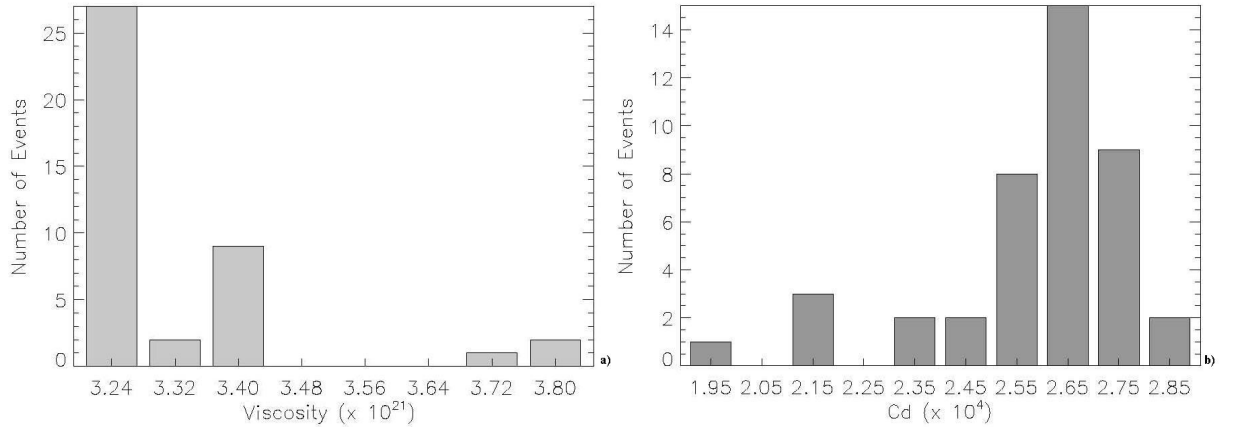


FIGURE 6.1 - Histograms for coefficients ν and C_d . Case: Satellite at 1 AU, Table (5.3). a) Laminar regime, b) Turbulent regime.

Figure (6.6) shows the behavior of the ICME speed versus distance using the model in the case of laminar and turbulent regime, for satellite at 1 AU.

6.2 Results for the events detected by satellites at distances lower than 1 AU

Figures (6.7), (6.8), (6.9), (6.10), and (6.11) show the histograms for the coefficients ν , C_d , radial exponent p , mass m_{cme} , density, and solar wind velocity V_{sw} using the values of Table (5.5) for satellites at distances lower than 1 AU.

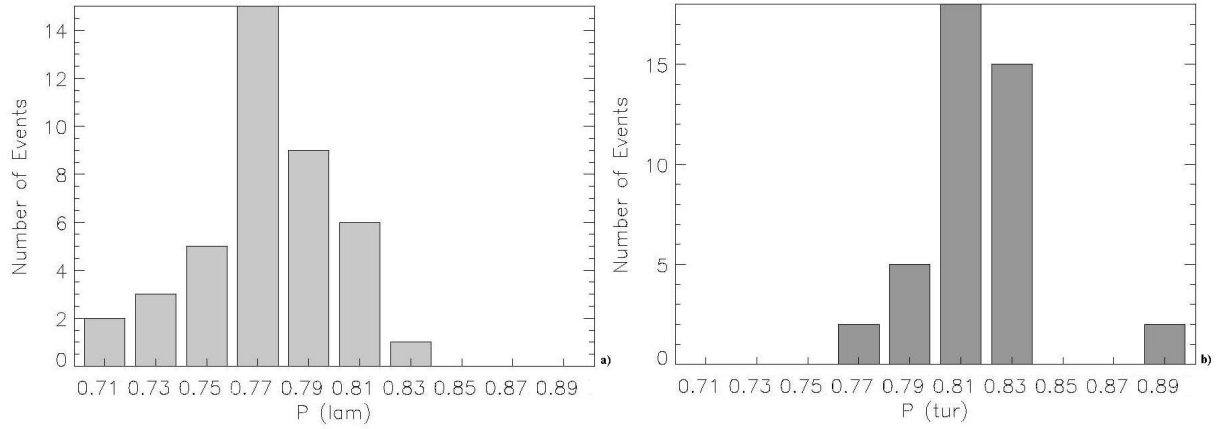


FIGURE 6.2 - Histograms for radial exponent p . Case: Satellite at 1 AU, Table (5.3). a) Laminar regime, b) Turbulent regime.

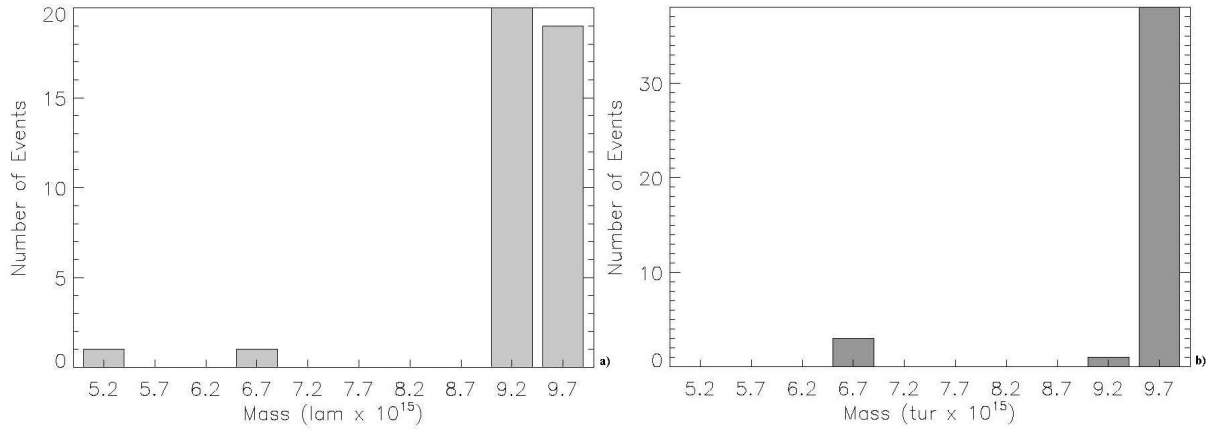


FIGURE 6.3 - Histograms for mass m_{cme} . Case: Satellite at 1 AU, Table (5.3). a) Laminar regime, b) Turbulent regime.

Figure (6.12) shows the behavior of the ICME speed versus distance using the models in the case of laminar and turbulent regimes respectively, for satellite at distances lower than 1 AU. The diamonds in the figure correspond to the position of the satellite and the ICME velocity.

6.3 Type II burst

Figures (6.13), (6.14), (6.15), (6.16), and (6.17) show the histograms for the coefficients ν , C_d , radial exponent p , mass m_{cme} , density, and solar wind velocity V_{sw} using the values of Table (5.8) for Type II burst.

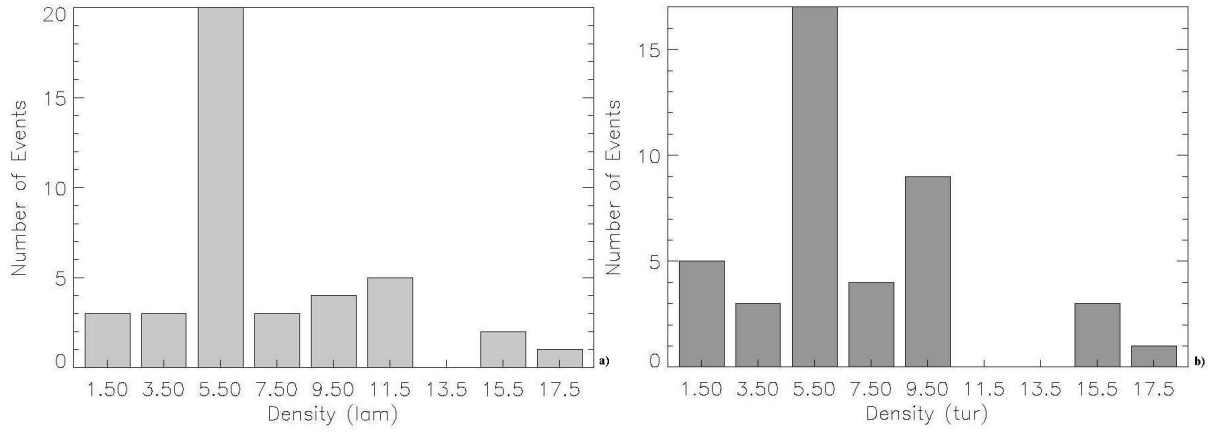


FIGURE 6.4 - Histograms for density. Case: Satellite at 1 AU, Table (5.3). a) Laminar regime, b) Turbulent regime.

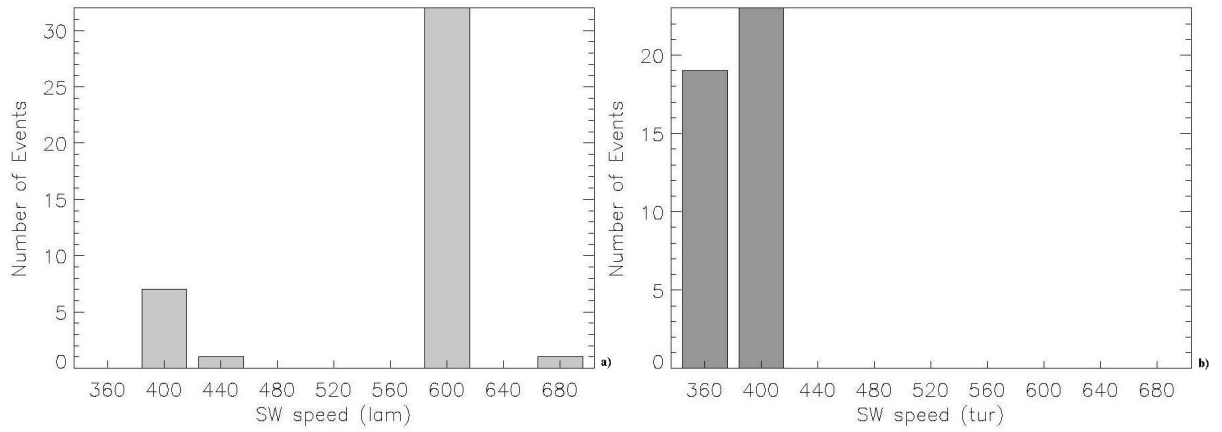


FIGURE 6.5 - Histograms for solar wind velocity V_{sw} . Case: Satellite at 1 AU, Table (5.3). a) Laminar regime, b) Turbulent regime.

Figure (6.18) shows the behavior of the ICME speed versus distance using the model in the case of laminar and turbulent regimes, respectively, for Type II burst.

The histograms in the Figures (6.1), (6.7) and (6.13) present the values calculated for the kinematic viscosity and drag coefficient. In the case of laminar regime the values are between $2.84 \times 10^{21} - 3.80 \times 10^{21} \text{ cm}^2/\text{s}$ range, with the maximum value for ν equal to $3.24 \times 10^{21} \text{ cm}^2/\text{s}$. In the turbulent regime the values are between $1.75 \times 10^4 - 6.25 \times 10^4$ range, with the maximum value for the drag coefficient C_d equal to 2.65×10^4 .

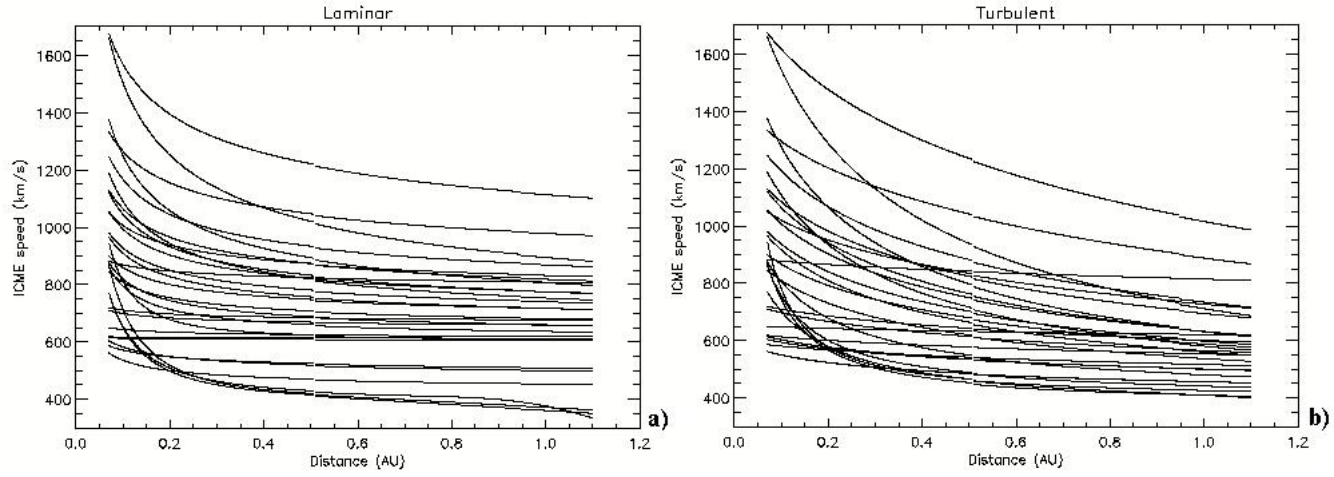


FIGURE 6.6 - Model ICME speed versus distance. Case: Satellite at 1 AU, a) Laminar regime, b) Turbulent.

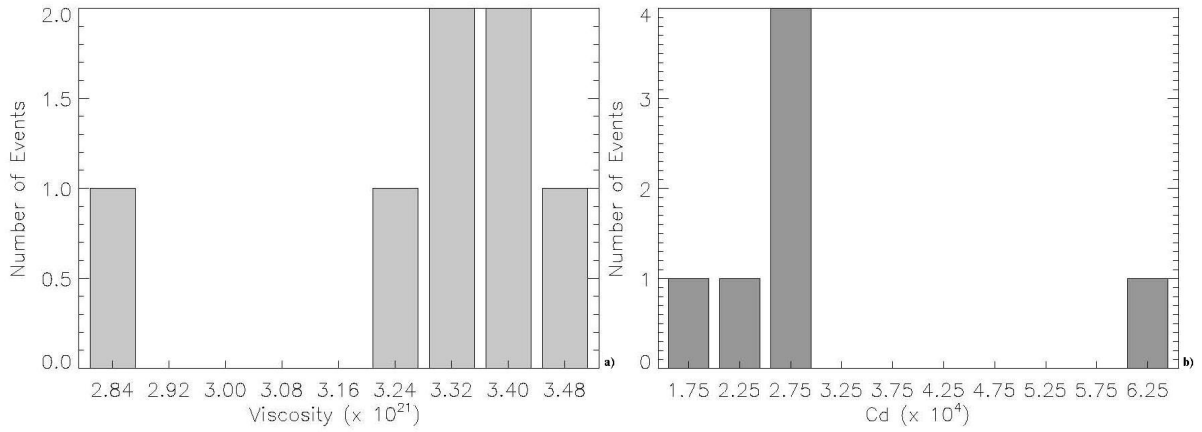


FIGURE 6.7 - Histograms for coefficients ν and C_d . Case: Satellite at distances lower than 1 AU, Table (5.5). a) Laminar regime, b) Turbulent regime.

Figures (6.2), (6.8) and (6.14) show the distribution of the radial exponent p in the laminar and turbulent regimes. In the first case the values are between 0.71 - 0.89, with the maximum in 0.77 (independently of the type of data, i.e., satellite at 1 AU, satellite at distances lower than 1 AU or Type II burst). For the second case (turbulent regime) corresponds the same interval but with the maximum in 0.81.

In Figures (6.3), (6.9) and (6.15) we show the histograms of values for the mass m_{cme} . The range is between $5.2 \times 10^{15} - 9.8 \times 10^{15}$ g, with the maximum value equal to 9.2×10^{15} g in the laminar regime. In the turbulent case the range is the

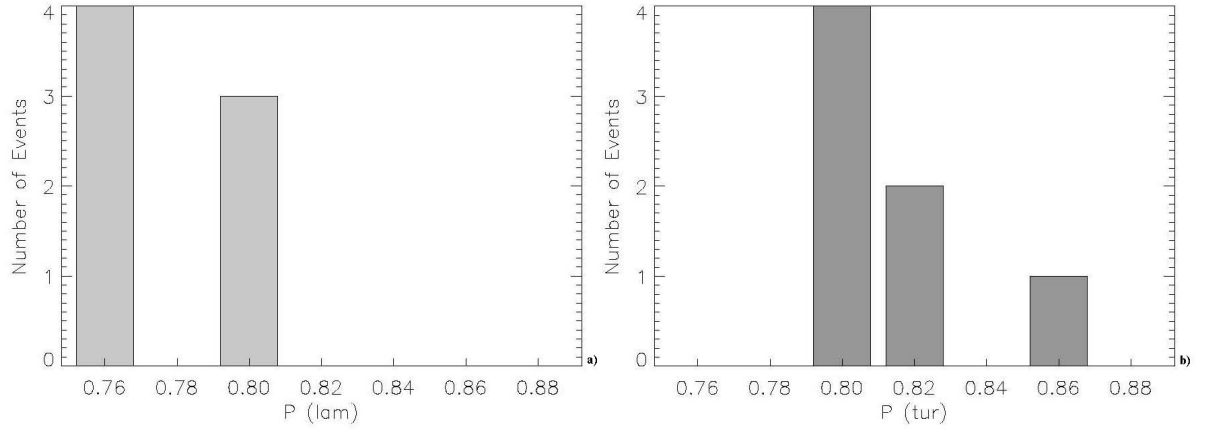


FIGURE 6.8 - Histograms for radial exponent p . Case: Satellite at distances lower than 1 AU, Table (5.5). a) Laminar regime, b) Turbulent regime.

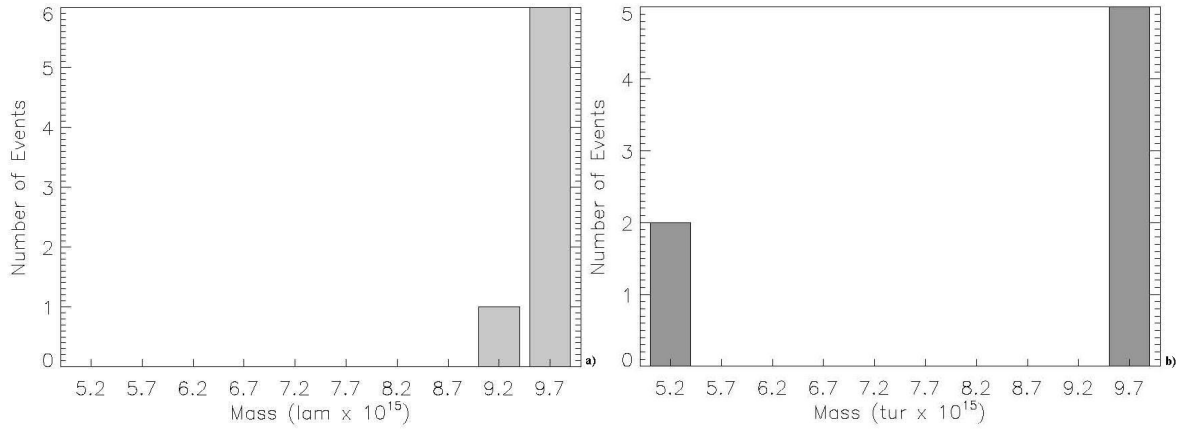


FIGURE 6.9 - Histograms for mass m_{cme} . Case: Satellite at distances lower than 1 AU, Table (5.5). a) Laminar regime, b) Turbulent regime.

same as the laminar regime but with the maximum value equal to 9.7×10^{15} g. The analysis shows that for the three types of data, satellites at 1 AU, satellites at distances lower than 1 AU and Type II burst, the medium value for the mass is in the upper extreme of the interval, i.e., for high values of the mass (9.7×10^{15} g - 9.8×10^{15} g).

The distributions of solar wind density, are presented in Figures (6.4), (6.10) and (6.16). In the first case, laminar regime, the values are between $1.50 - 17.5 \text{ part/cm}^3$ with the maximum in 5.50 part/cm^3 . In the turbulent regime the value range is the same as the laminar regime with the same maximum value, i.e., 5.50 part/cm^3 . In

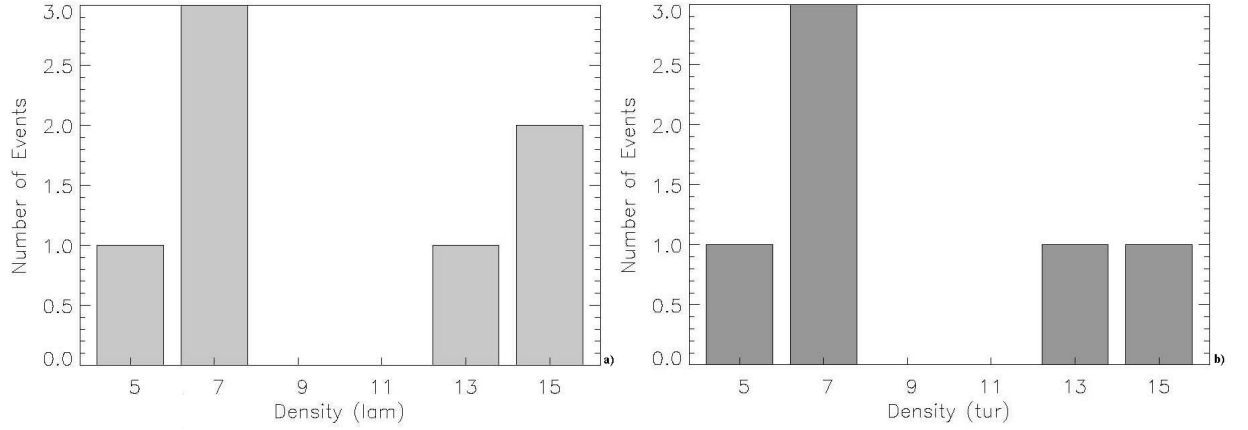


FIGURE 6.10 - Histograms for density. Case: Satellite at distances lower than 1 AU, Table (5.5). a) Laminar regime, b) Turbulent regime.

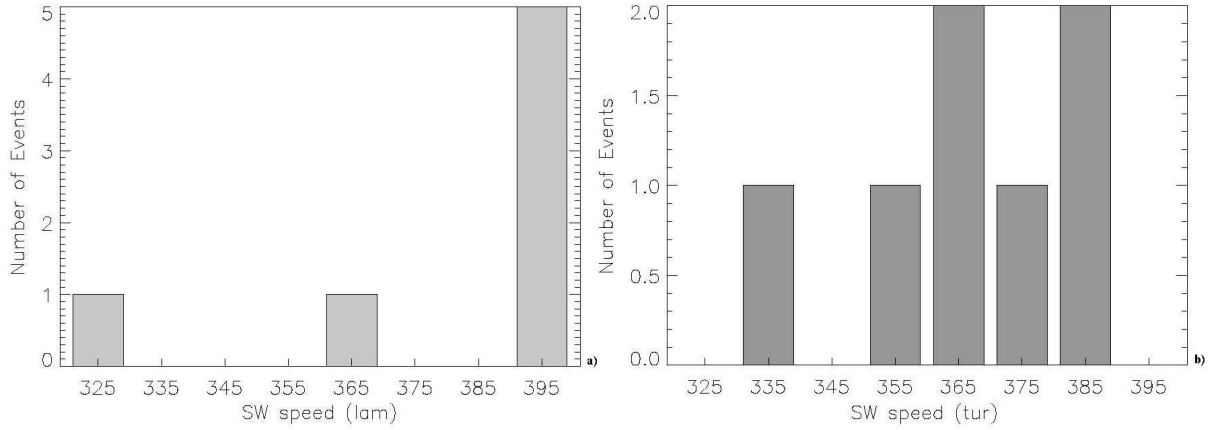


FIGURE 6.11 - Histograms for solar wind velocity V_{sw} . Case: Satellite at distances lower than 1 AU, Table (5.5). a) Laminar regime, b) Turbulent regime.

view of this analysis we can estimate a medium value for the solar wind density as 5 part/cm^3 at 1 AU.

Figures (6.5), (6.13) and (6.17) show the histograms of the solar wind speed V_{sw} . The values are between 325 km/s - 680 km/s in the laminar regime with the maximum in 600 km/s. For the turbulent case the values are in the same range but the maximum is in 400 km/s. It is evident from this analysis that it is different the behavior in the laminar and turbulent regime. For the laminar case the solar wind takes values of 600 km/s and in the turbulent regime the values are low, compared with the laminar regime, i.e., 400 km/s.

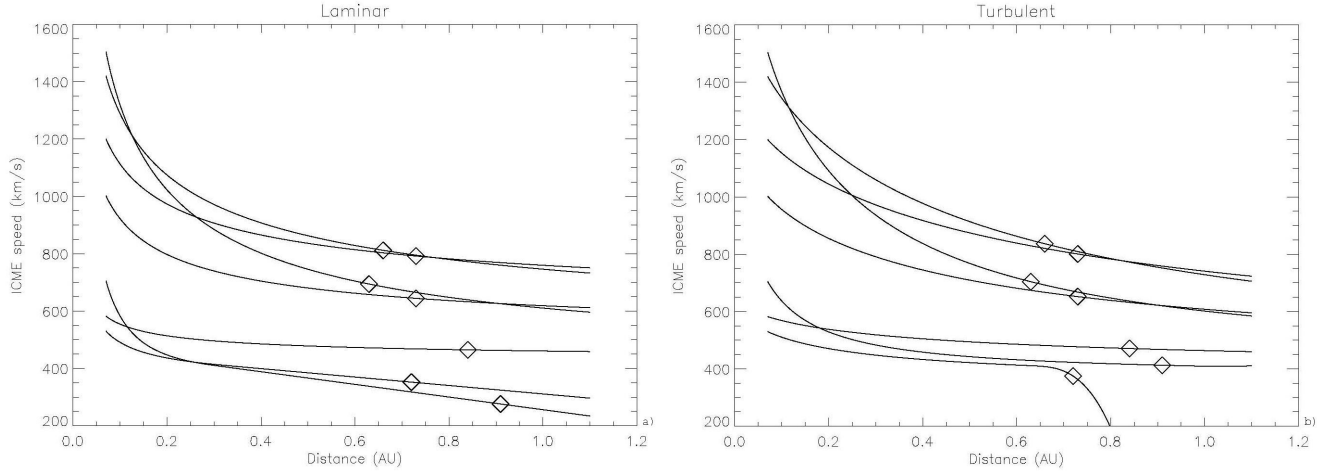


FIGURE 6.12 - Model ICME speed versus distance. Case: Satellite at distances lower than 1 AU, a) Laminar regime, b) Turbulent. The diamonds correspond to the satellite position and velocity of ICME for each event.

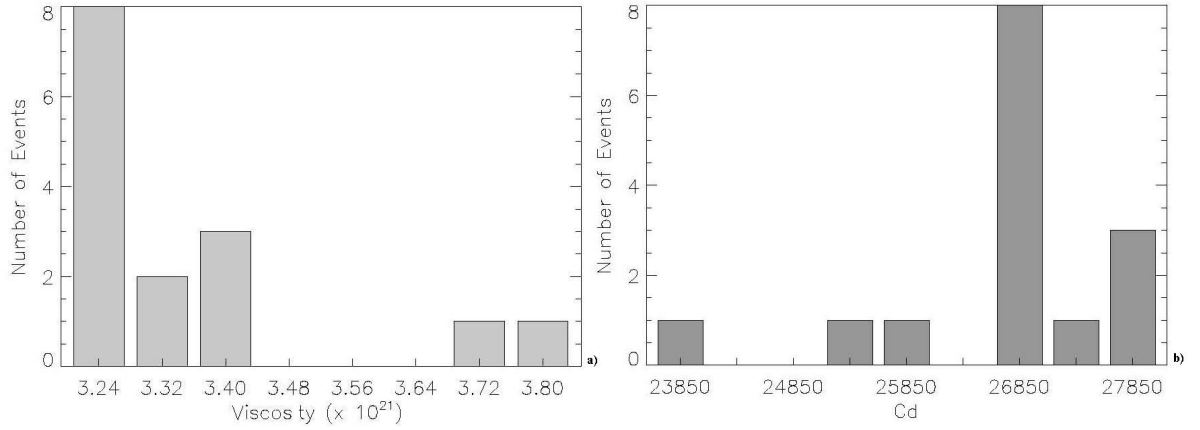


FIGURE 6.13 - Histograms for coefficients ν and C_d . Case: Type II burst, Table (5.8). a) Laminar regime, b) Turbulent regime.

6.4 ICME Travel Time

The ICME travel time from the Sun to the Earth is an important parameter in terms of space weather prediction. Empirical models (GOPALSWAMY et al., 2000; GOPALSWAMY et al., 2001; GOPALSWAMY et al., 2005) and (VRSNAK, 2001; VRSNAK, 2002; VRSNAK et al., 2004; VRSNAK; ZIC, 2007) and others like (DALLAGO et al., 2004; HOWARD et al., 2007; LINDSAY et al., 1999; SCHWENN; LAGO; GONZALEZ, 2005;

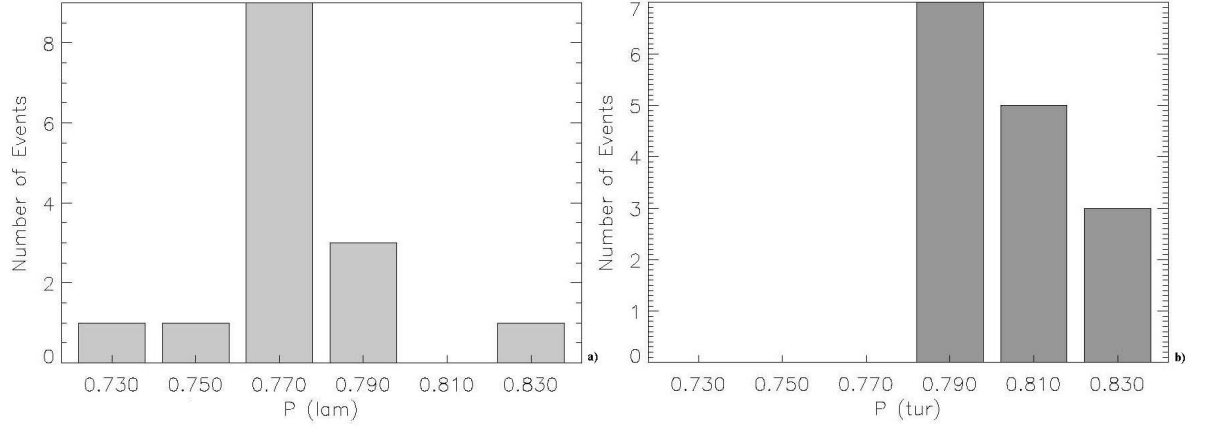


FIGURE 6.14 - Histograms for radial exponent p . Case: Type II burst, Table (5.8). a) Laminar regime, b) Turbulent regime.

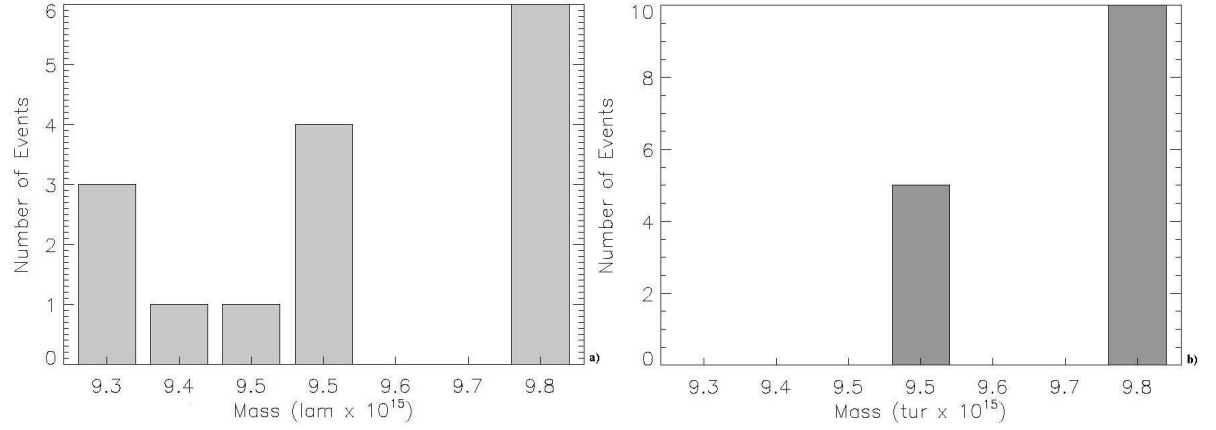


FIGURE 6.15 - Histograms for mass m_{cme} . Case: Type II burst, Table (5.8). a) Laminar regime, b) Turbulent regime.

WEBB et al., 2000b; WEBB et al., 2000a) have proposed predictions at 1 AU of the arrival time of coronal mass ejections. In order to show the comparison between our results and these models, we have plotted in Figure (6.19) the travel time versus the ICME velocities, considering different cases of the drag force. The thick dark green line is the solution for the laminar regime, with $\nu_1 = 0.002$ kg/m.s, the thick clear green line represents the same regime but with $\nu_2 = 0.02$ kg/m.s. The turbulent regime travel times are plotted with dot lines, clear blue for $C_{d1} = 200$ and violet for $C_{d2} = 2000$. In the case of coupled (laminar plus turbulent) regime, the pink dash line corresponds to coefficients ν_1 and C_{d1} . The red dash line corresponds to the same regime but with coefficients ν_2 and C_{d2} . When using the low values of

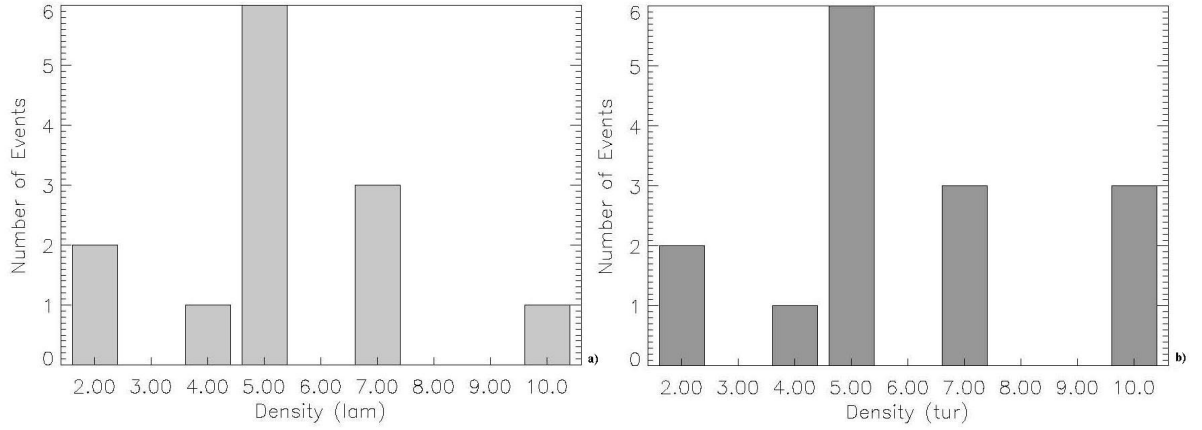


FIGURE 6.16 - Histograms for density. Case: Type II burst, Table (5.8). a) Laminar regime, b) Turbulent regime.

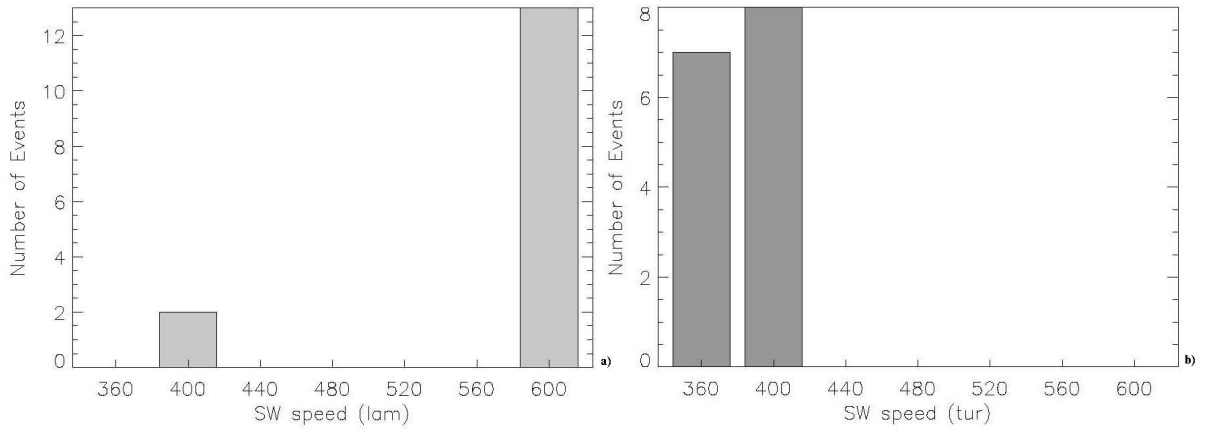


FIGURE 6.17 - Histograms for solar wind velocity V_{sw} . Case: Type II burst, Table (5.8). a) Laminar regime, b) Turbulent regime.

the coefficients (ν_1 and C_{d1}) the travel times are similar. On the other hand, the travel time profiles change significantly when using the high value coefficients (ν_2 and C_{d2}). In order to compare our results with some empirical models, we have plotted the Gopalswamy et al. (2000) model (thick black continuous line) and the Gopalswamy et al. (2001) modified model (thin black continuous line). We can see that the empirical model Gopalswamy et al. (2001) presents good agreement with our result for the laminar regime higher limit (using a viscous coefficient of 0.02 kg/m.s).

Independently of the values of the coefficients (drag or viscous), it is easy to see that

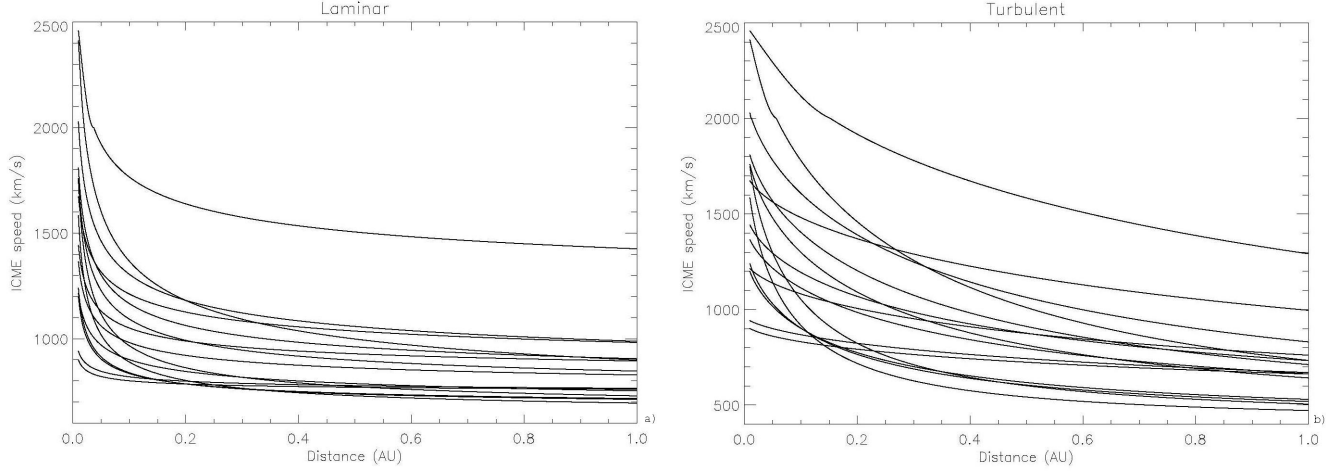


FIGURE 6.18 - Model ICME speed versus distance. Case: Type II burst, a) Laminar regime, b) Turbulent regime.

in all cases, the ICME has a damping (more accentuated when the coefficients have higher values) that agrees with the idea of a kind of viscous interaction between the ICME and the interplanetary solar wind. This interaction produces the deceleration of the structure to an asymptotic value of 400 km/s, that corresponds to the ambient solar wind velocity. This figure shows that our simple and systematic analytical approach may represent the ICME dynamics as well as the empirical models. We are reproducing, in a quite good shape, through a theoretical model, the empirical results claimed by Gopalswamy et al. (2000, 2001).

6.5 The drag term

According to Reiner, Kaiser and Bougeret (2003) the radio observations show that the propagation of fast CMEs away from the Sun are inconsistent with the drag term that causes deceleration with the distance from the Sun. The distinction is between a speed versus distance profile that changes the concavity downward to upward. In that work, Reiner pointed out that the standard form of the drag term gives profiles that are incorrectly concave upwards, which leads to the important conclusion that the standard form of the drag term evidently does not apply to CME propagation. As is mentioned in chapter (3), Section (3.9.3), the drag term takes the form of Equation (6.1):

$$F_t = \frac{C_d A \rho_{sw} \cdot (U - U_{sw})^2}{2}. \quad (6.1)$$

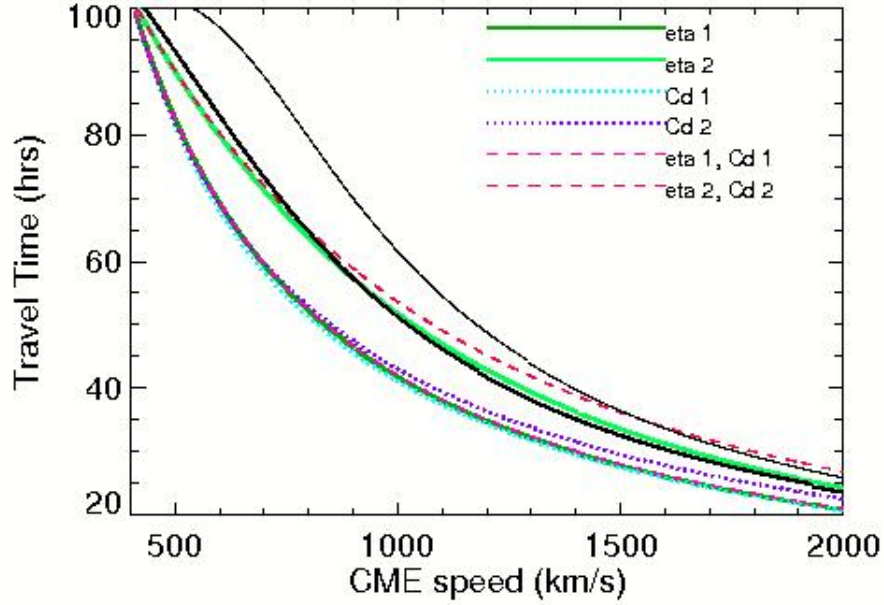


FIGURE 6.19 - This figure shows the time-travel covered by the ICME as a function of its velocity comparing our results for different ν and C_d values with respect to empirical models (GOPALSWAMY et al., 2000; GOPALSWAMY et al., 2001).

SOURCE: Borgazzi et al. (2008).

Vrsnak (2002) shows that the disagreement mentioned between the work of Gopalswamy and Reiner (2005, 2003) and the standard drag term occurs also if the drag term goes linearly with the speed difference instead of quadratic. In either case, the primary reason that the velocity versus distance profiles are concave upward is that, near the Sun, the density, ρ_{sw} , is large and the velocity difference, $U_{cme} - U_{sw}$, is large too, and in this form the terms are small far from the Sun.

It means that drag term is relevant near the Sun and can be negligible farther. The problem might go away if the drag coefficient C_d , is small near the Sun making the magnetic pressure larger than the plasma pressure in this region (CARGILL; CHEN, 1996). The idea is that a body moving fast through a fluid experiences drag force as a result of the flow separating the flanks from the body. Analysing scintillation data (IPS), Manoharan et al. (2001, 2006) found that ICMEs show a low decline in speed below $100 R_{\odot}$ (0.36 AU) and a rapid decrease after this distance.

This behavior is in agreement with the concavity of the curves (speed versus dis-

tance) of Borgazzi et al. (2009). On the other hand, by analyzing type II bursts, Reiner et al. (2003) found that a drag force can not explain the observed frequency drift. They argued that it is necessary a change in concavity of the velocity-distance curve in order to fit the type II data. As is mentioned in Borgazzi et al. (2009) the work of Reiner et al. (2003) uses similar variations for both CME area ($\sim x^2$) and SW density ($\sim x^{-2}$).

6.6 ICME speed versus distance

The acceleration in the interplanetary medium of CMEs is well established (GOPALSWAMY et al., 2000; GOPALSWAMY et al., 2001; MANOHARAN et al., 2001; MANOHARAN, 2006; HOWARD et al., 2007). This acceleration has been explained by an increase of the ICME mass (snow-plough model (TAPPIN, 2006)) or due to Lorentz force (CHEN, 1996; HOWARD et al., 2007), although it is more common to attribute this acceleration to drag forces (VRSNAK, 2001; CARGILL, 2004).

However, the exact form, the magnitude of the related coefficients and the dependence of this drag force with the CME or SW parameters are still unknown. Even more, there are doubts about this force acting on ICMEs (REINER; KAISER; BOUGERET, 2003; FORBES et al., 2006). As pointed out by Vrsnak (2006), by considering the kinetic energy of ICMEs, the gravity and Lorentz forces are negligible in the interplanetary space.

Therefore, a drag force should act in the interchange of momentum between the ICME and the SW. All forces, Lorentz, aerodynamic drag, and gravity, decrease with the heliocentric distance (CHEN; GARREN, 1993; CHEN, 1996; SHEELEY et al., 1997; VRSNAK, 2006). Although, the Lorentz force is the most important at low heights then the drag becomes predominant after $\sim 30 R_{\odot}$ (VRSNAK, 2006). Recently, to explain IPS and white light observations (SMEI), (HOWARD et al., 2007) has suggested that the drag force overcomes the Lorentz force at greater distances, between 80 to 100 R_{\odot} . Here, since we are not taking the magnetic field effects into account, we neglect the Lorentz force.

In order to understand and model the drag force acting on the ICME - SW system, we explore two forms of this force (linearly and quadratically dependent with the ICME speed) and variations in the CME radius and the SW density. Our analytical model helps to physically understand the effects of these parameters and dependences in

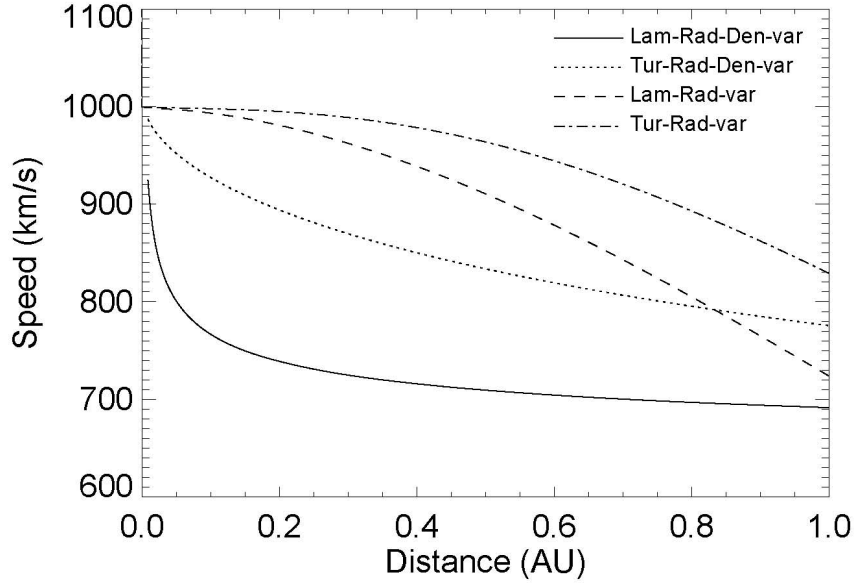


FIGURE 6.20 - ICME speed versus distance for the four models analyzed in this work. a) laminar regime considering variability in ICME radius (Eq. 4.9) and $\mu = 0.175 \text{ g/cm} \cdot \text{s}$ (dashed line). b) turbulent regime considering variability in ICME radius (Eq. 4.10) and $C_d = 5 \times 10^4$ (dot-dashed line). c) laminar regime considering variability in ICME radius and SW density (Eq. 4.16) and $\nu = 8.75 \times 10^{20} \text{ cm}^2/\text{s}$ (continuous line). and d) turbulent regime considering variability in ICME radius and SW density (Eq. 4.13) and $C_d = 1.1 \times 10^5$ (dot line).

the ICME dynamics. To perform such comparison, in Figure (6.20) we plot the solutions of Equations (4.9), (4.10), (4.13), and (4.16), assuming an initial speed of 1000 km/s and the parameters (μ and C_d) corresponding to the mean values of these parameters used in Figure (4.7) to (4.8). Upon inspection of Figure (6.20), it is easy to see a completely different behavior between the models considering only variability of the ICME radius and considering variability of both, ICME radius and solar wind density.

When the dominant variation is the CME radius (as $x^{0.78}$), the curves have negative concavity; whereas the density variation (as x^{-2}) is dominant, the concavity changes, meaning that the density of the medium plays an important role in the transport of the ICMEs (REINER; KAISER; BOUGERET, 2003). Using scintillation data (IPS), (MANOHARAN et al., 2001) and (MANOHARAN, 2006) have found that ICMEs show a low decline in speed below $100 R_{\odot}$ (0.36 AU) and a rapid decrease after this distance.

7 CONCLUSION AND FUTURE WORKS

In this work we present an analytical model which describes the momentum exchange between ICMEs and the solar wind, from the point of view of the fluid dynamics, considering the ICMEs and the solar wind as two interacting fluids with viscous interaction. We have tested the ICME dynamics using linear, and polynomial (order 2) drag forces.

We find 5 parameters related with the interaction between the ICME and the medium surrounding, the solar wind. These values have been quantified and we can give an estimation of the importance of each one.

Our model can reproduce the differences between the CME speed observed near the Sun and the ICME speeds observed near 1 AU. Also, this model is able to reproduce, in a qualitatively good shape, an empirical model for the ICME travel time.

The model reproduces the dynamics of Type II bursts in the interplanetary medium also, and it is possible to observe how the theoretical curves of our model have a similar drift to the Type II burst drift.

Even though we did not take into account the magnetic field with this hydrodynamics approximation, we can give values for the drag coefficient C_d and dynamics viscous coefficient μ at 1 AU.

This model could be used as a first approximation to the understanding of the ICME dynamics in the interplanetary medium.

Giving continuity to this work we will use a more extended data base to corroborate the analytical solutions presented in this work. We also intend to construct a more accurate description of the ICME dynamics; it will be necessary to introduce new factors to the model as: geometry of the ICME, interplanetary and ICME magnetic field, solar wind dependence with position.

Another point to be treated is the study of the functional dependence of the drag and viscous coefficients to give a more accurate description of these values in the interplanetary medium.

REFERENCES

- ANTIOCHOS, S.; DEVORE, C.; KLIMCHUK, J. A model for solar coronal mass ejections. *The Astrophysical Journal*, v. 510, p. 485–493, 1999. [34](#), [36](#)
- BATCHELOR, G. *An introduction to fluid dynamics*. [S.l.]: Cambridge University Press, 2000. 615 p. [48](#)
- BISKAMP, D.; WELTER, H. Magnetic arcade evolution and instability. *Solar Physics*, v. 120, p. 49–77, 1989. [34](#)
- BORGAZZI, A. *Space-time correlation analysis between EIT and Moreton waves*. [S.l.: s.n.], 2003. 114 p. [28](#)
- BORGAZZI, A. et al. Dynamics of coronal mass ejections in the interplanetary medium. *Astronomy and Astrophysics*, v. 498, n. 3, 2009. [37](#), [59](#), [61](#), [65](#), [66](#), [114](#)
- BORGAZZI, A. et al. Transport in the interplanetary medium of coronal mass ejections. *Geofisica Internacional*, v. 47, n. 3, p. 301–310, 2008. [61](#), [62](#), [63](#), [64](#), [113](#)
- BOUGERET, J. et al. Waves: The radio and plasma wave investigation on the wind spacecraft. *Space Science Reviews*, v. 71, n. 1–4, p. 231–263, 1995. [90](#)
- BRUECKNER, G. et al. The large angle spectroscopic coronagraph (lasco). *Solar Physics*, v. 162, n. 1–2, 1995. [26](#)
- CANE, H.; SHEELEY, N.; HOWARD, R. Energetic interplanetary shocks, radio emission, and coronal mass ejections. *Journal of Geophysical Research*, v. 92, 1987. [27](#)
- CANTO, J. et al. The dynamics of velocity fluctuations in the solar wind i. coronal mass ejections. *Mon. Not. Astron. Soc.*, v. 357, p. 572–578, 2005. [29](#)
- CARGILL, P. On the aerodynamic drag for acting on interplanetary coronal mass ejections. *Solar Physics*, v. 221, p. 135–149, 2004. [28](#), [30](#), [114](#)
- CARGILL, P.; CHEN, J. Magnetohydrodynamics simulation of the motion of a magnetic flux tubes through a magnetized plasma. *Journal of Geophysical Research*, v. 101, n. A3, 1996. [30](#), [113](#)
- CHAKRAVARTI; LAHA; ROY. *Handbook of methods of applied statistics*. [S.l.]: John Wiley and Sons, 1967. [129](#)

- CHEN, J. Effects of toroidal forces in current loops embedded in a background plasma. *Astrophys. J.*, v. 338, p. 453–470, 1989. [34](#), [36](#)
- CHEN, J. Theory of prominence eruption and propagation: Interplanetary consequences. *J. Geophys. Res.*, v. 101, p. 27499–27519, 1996. [36](#), [38](#), [57](#), [114](#)
- CHEN, J. Coronal mass ejections. In: *Geophysical Monograph 99*. Washington, D. C.: Crooker, N.; Joselyn, J.; Feyman, J., 1997. p. 65–81. [36](#), [38](#)
- CHEN, J.; GARREN, D. Interplanetary magnetic clouds: Topology and driving mechanism. *Geophys. Res. Lett.*, v. 20, n. 21, p. 2319–2322, 1993. [57](#), [114](#)
- CHEN, J. et al. Magnetic geometry and dynamics of the fast coronal mass ejection of 1997 september 9. *Astrophys. J.*, v. 553, p. 481–500, 2000. [36](#)
- CHEN, P.; SHIBATA, K.; YOKOYAMA, T. Physics of coronal mass ejections: A new paradigm of solar eruptions. *Earth, Planets and Space*, v. 53, 2001. [34](#)
- CYR, O. S. et al. A comparison of ground-based and spacecraft observations of coronal mass ejections from 1980-1989. *Journal of Geophysical Research*, v. 104, n. A6, p. 12493–12506, 1999. [26](#)
- DALLAGO, A. et al. Comparison between halo cme expansion speeds observed on the sun, the related shock transit speeds to earth and the corresponding ejecta speeds at 1 au. *Solar Physics*, v. 222, p. 323–328, 2004. [30](#), [37](#), [109](#), [110](#)
- DAUGHERTY, R.; FRANZINI, J.; FINNEMORE, E. *Fluid mechanics with engineering applications*. [S.l.]: McGraw-Hill, 1989. [54](#)
- DELANNÉE, C. Another view of the eit wave phenomenon. *The Astrophysical Journal*, v. 545, n. 1, 2000. [26](#)
- DEVORE, C. R.; ANTIOCHOS, S. K. Magnetic free energies of breakout coronal mass ejections. *The Astrophysical Journal*, v. 628, n. 2, p. 1031–1045, 2005. [34](#)
- DUNGEY, J. The steady state of the chapman-ferraro problem in two dimensions. *Journal of Geophysical Research*, v. 66, n. 4, p. 1043–1047, 1961. [27](#)
- ECHER, E. et al. On the preferential occurrence of interplanetary shocks in july and november: Causes (solar wind annual dependence) and consequences (intense magnetic storms). *Journal of Geophysical Research*, v. 110, n. A2, 2005. [25](#), [27](#)

- EDDY, J. The maunder minimum. *Science*, v. 192, p. 1189–1202, 1976. [25](#)
- FORBES, T. et al. Cme theory and models. *Space Science Reviews*, v. 123, 2006. [34](#), [35](#), [38](#), [114](#)
- GINZBURG, V.; ZHELEZNYAKOV, V. On the possible mechanism of sporadic solar radio emission (radiation in an isotropic plasma). *Astron. Zh.*, v. 35, n. 694, 1958. [133](#)
- GONZALEZ-ESPARZA, A. et al. A numerical study on the acceleration and transit time of coronal mass ejections in the interplanetary medium. *Journal of Geophysical Research*, v. 108, n. A1, 2003. [30](#)
- GONZALEZ, W.; ECHER, E. A study on the peak dst and peak negative bz relationship during intense geomagnetic storms. *Geophysical Research Letters*, v. 32, n. 18, p. L18103, 2005. [27](#)
- GONZALEZ, W. D.; TSURUTANI, B. T.; GONZALEZ, A. L. Clua de. Interplanetary origin of geomagnetic storms. *Space Science Reviews*, v. 88, n. 3–4, p. 529–562, 1999. [25](#), [27](#)
- GOPALSWAMY, N. Table events. *Goddard Space Flight Center, 2004*, Private communication. [37](#)
- GOPALSWAMY, N. et al. Type ii radio burst and energetic solar eruptions. *Journal of Geophysical Research*, v. 110, n. A12S07, 2005. [91](#)
- GOPALSWAMY, N. et al. Interplanetary acceleration of coronal mass ejections. *Geophysical Research Letters*, v. 27, p. 145–148, 2000. [20](#), [26](#), [29](#), [37](#), [61](#), [109](#), [111](#), [112](#), [113](#), [114](#)
- GOPALSWAMY, N. et al. An empirical model to predict the 1-au arrival of the interplanetary shocks. *Advance Space Research*, v. 36, p. 2.289–2.294, 2005. [27](#), [29](#), [109](#), [113](#)
- GOPALSWAMY, N. et al. Predicting the 1-au times of coronal mass ejections. *Journal of Geophysical research*, v. 18, p. 29.207–29.217, 2001. [20](#), [26](#), [29](#), [84](#), [85](#), [109](#), [111](#), [112](#), [113](#), [114](#)
- GOSLING, J. Coronal mass ejections. In: *INTERNATIONAL COSMIC RAY CONFERENCE (ICRC XXVI)*, 26. [S.l.]: Proceedings. American Institute of Physics, 2000. p. 59. [26](#)

- HARRISON, R. Solar coronal mass ejections and flares. *Astronomy and Astrophysics*, v. 162, 1986. [34](#)
- HOWARD, T. A. et al. On the evolution of coronal mass ejections in the interplanetary medium. *Astrophysics Journal*, v. 667, p. 620–625, 2007. [30](#), [109](#), [110](#), [114](#)
- HU, Q.; SONNERUP, B. Reconstruction of magnetic clouds in the solar wind: Orientations and configurations. *J. Geophys. Res.*, v. 107, n. A7, 2002. [37](#), [38](#)
- ILLING, R.; HUNDHAUSEN, A. Disruption of a coronal streamer by an eruptive prominence and coronal mass ejection. *J. Geophys. Res.*, v. 90, p. 257–282, 1986. [36](#)
- KAISER, M. The stereo mission: an overview. *Adv. Space Res.*, v. 36, p. 1483–1488, 2005. [33](#)
- KLEIN, L.; BURLAGA, L. Interplanetary magnetic clouds at 1 au. *J. Geophys. Res.*, v. 87, p. 613–624, 1982. [37](#)
- KRALL, J.; CHEN, J.; SANTORO, R. Drive mechanisms of erupting solar magnetic flux ropes. *Astrophys. J.*, v. 539, p. 964–982, 2000. [34](#), [36](#)
- KUNDU, P. K.; COHEN, I. M. *Fluid mechanics*. [S.l.]: Elsevier Academic Press, 2004. 759 p. [39](#), [40](#), [41](#), [42](#), [46](#), [48](#), [50](#), [51](#), [60](#)
- KUPERUS, M.; RAADU, M. The evolution of magnetic fields and unstable solar plasmas. *Astronomy and Astrophysics*, v. 31, 1974. [34](#), [35](#)
- KUSANO, K. et al. Study of magnetic helicity in the solar corona. *Astrophysics Journal*, v. 610, 2004. [34](#)
- LANDAU, L.; LIFSHITZ, M. *Fluid mechanics*. [S.l.]: Elsevier Academic Press, 1987. [53](#)
- LANZEROTTI, J. *Handbook of the solar-terrestrial environment*. [S.l.]: Berlin, Springer, 2007. [25](#)
- LARA, A.; BORGAZZI, A. Dynamics of interplanetary cmes and associated type ii burst. In: INTERNATIONAL ASTRONOMICAL UNION, 2008, Greece. *Proceedings IAU Symposium*. [S.l.]: International Astronomical Union, 2008. p. 287–290. [90](#)

LEBLANC, Y.; DULK, G.; BOUGERET, J. Tracing the electron density from the corona to 1 au. *Solar Physics*, v. 183, 1996. [26](#), [27](#), [58](#), [59](#)

LEPPING, R. et al. Profile of an average magnetic cloud at 1 au for the quiet solar phase: Wind observations. *Solar Physics*, v. 212, p. 425–444, 2003. [38](#)

LEROY, J.; BOMMIER, V.; SAHAL-BRECHOT, S. The magnetic field in the prominences of the polar crown. *Solar Physics*, v. 83, 1983. [35](#)

LIN, J.; RAYMOND, J.; BALLEGOOIJEN, A. The role of magnetic reconnection in the observable features of solar eruptions. *Astrophysical Journal*, v. 602, p. 422–435, 2004. [35](#)

LINDSAY, G. M. et al. Relationships between coronal mass ejection speeds from coronagraph images and interplanetary characteristics of associated interplanetary coronal mass ejections. *Journal of Geophysical Research*, v. 104, n. A6, p. 12.515–12.523, 1999. [30](#), [109](#), [110](#)

LINKER, J. et al. Eruptive behavior originating in active regions. *Physics Plasmas*, v. 10, 2003. [34](#)

LITES, B. et al. The possible ascent of a closed magnetic system through the photosphere. *Astrophysics Journal*, v. 446, 1995. [35](#)

LIU, I.; RICHARDSON, J.; BELCHER, J. *Planetary and Space Science*, v. 53, p. 3 – 17, 2005. [55](#), [57](#)

LIVI, S. et al. The association of flares to cancelling magnetic features on the sun. *Solar Physics*, v. 121, p. 197–214, 1989. [35](#)

MANOHARAN, P. Evolution of coronal mass ejections in the inner heliosphere: A study using white light and scintillation images. *Solar Physics*, v. 235, 2006. [27](#), [113](#), [114](#), [115](#), [131](#)

MANOHARAN, P. Table events. *Ooty Radioastronomy Center, 2007*, Private communication, 2007. [82](#), [84](#)

MANOHARAN, P. et al. Coronal mass ejection of 2000 july 14 flare event: Imaging from near-sun to earth environment. *Astrophysical Journal*, v. 559, p. 1180–1189, 2001. [113](#), [114](#), [115](#)

- MARTIN, S.; LIVI, S.; WANG, J. The cancellation of magnetic flux ii - in a decaying active region. *Australian J. Phys.*, v. 38, p. 929–959, 1985. [35](#)
- MCCOMAS, D. et al. Solar wind electron proton alpha monitor (swepam) for the advanced composition explorer. *Space Science Reviews*, v. 86, n. 1/4, 1998. [26](#)
- MCLEAN, D.; LABRUM, R. *Solar radiophysics: estudies of emissions from the sun at meter wavelengths*. [S.l.]: Knudsen, 1985. [131](#)
- MIKIC, Z.; BARNES, D.; SCHNACK, D. *Astrophysics Journal*, v. 328, p. 830–847, 1988. [34](#)
- MULLIGAN, T.; RUSSELL, C. Multispacecraft modeling of the flux rope structure of interplanetary coronal mass ejections: Cylindrically symmetric versus nonsymmetric topologies. *J. Geophys. Res.*, v. 106, p. 10581–10596, 2001. [38](#)
- ODSTRCIL, D. et al. 3-d mhd simulations of cmes by coupled coronal and heliospheric models. *Journal of Geophysical Research*, v. 107, 2002. [34](#)
- ODSTRCIL, D.; PIZZO, V. Three-dimensional propagation of coronal mass ejections (cmes) in a structured solar wind flow 1. cme launched adjacent the streamer belt. *Journal of Geophysical Research*, v. 104, n. A1, 1999. [30](#)
- ODSTRCIL, D.; PIZZO, V. Three-dimensional propagation of coronal mass ejections (cmes) in a structured solar wind flow 2. cme launched within the steamer belt. *Journal of Geophysical Research*, v. 104, n. A1, 1999. [30](#)
- OWENS, M. et al. Characteristic magnetic field and speed properties of interplanetary coronal mass ejections and their sheath regions. *J. Geophys. Res.*, v. 110, n. A1, 2005. [37](#)
- PICK, M.; VILMER, N. Sixty - five years of solar radioastronomy: flares, coronal mass ejections and sun-earth connection. *Astron. Astrophys. Rev.*, v. 16, p. 1–153, 2005. [131](#), [133](#)
- REINER, M.; KAISER, M.; BOUGERET, J. On the deceleration of cmes in the corona and interplanetary medium deduced from radio and white-light observations. In: AMER. INST. PHYS., 2003. *Solar wind ten*. New York: Velli, M., 2003. p. 152–155. [112](#), [113](#), [114](#), [115](#)

- ROBINSON, P. A. Nonlinear wave collapse and strong turbulence. *Modern Physics*, v. 69, n. 2, p. 507–573, 1997. [133](#)
- RUST, D.; KUMAR, A. Helical magnetic fields in filaments. *Solar Physics*, v. 155, 1994. [35](#)
- SCHWENN, R. Space weather, living rev. *Solar Physics*, 2006. [25](#)
- SCHWENN, R.; LAGO, A. D.; GONZALEZ, W. D. The association of coronal mass ejections with their effects near the earth. *Annales Geophysicae*, v. 23, p. 1.033–1.059, 2005. [30](#), [109](#), [110](#)
- SHEELEY, N. et al. Measurements of flow speeds in the corona between 2 and 30 solar radii. *Astrophysical Journal*, v. 484, p. 472–478, 1997. [57](#), [114](#)
- SHKLOVSKY, I. On the emission of radio waves by the galaxy and upper layers of the solar atmosphere. *Astron. Zh.*, v. 23, 1956. [132](#)
- SRIVASTAVA, N. et al. *Astrophysics Journal*, v. 534, 1971. [34](#)
- STONE, E. et al. The solar isotope spectrometer for the advanced composition explorer. *Space Science Reviews*, v. 86, 1998. [26](#)
- TAPPIN, S. The deceleration of an interplanetary transient from the sun to 5 au. *Solar Physics*, v. 233, p. 233–248, 2006. [114](#)
- VANDAS, M. et al. Simulation of magnetic cloud propagation in the inner heliosphere in two-dimensions. 1: A loop perpendicular to the ecliptic plane. *Journal of Geophysical Research*, v. 100, n. A7, 1995. [30](#)
- VRSSNAK, B. Dynamics of solar coronal eruptions. *Journal of Geophysical Research*, v. 106, n. A11, p. 25.249–25.259, 2001. [109](#), [114](#)
- VRSSNAK, B. Influence of aerodynamic drag on the motion of interplanetary ejecta. *Journal of Geophysical Research*, v. 107, n. A2, 2002. [29](#), [109](#), [113](#)
- VRSSNAK, B. Forces governing coronal mass ejections. *Adv. Space Res.*, v. 38, p. 431–440, 2006. [114](#)
- VRSSNAK, B. et al. Kinematics of coronal mass ejections between 2 and 30 solar radii. *Astronomy & Astrophysics*, v. 423, p. 717–728, 2004. [29](#), [109](#)

- VRSNAK, B.; ZIC, T. Transit times of interplanetary coronal mass ejections and the solar wind speed. *Astronomy & Astrophysics*, v. 472, p. 973–943, 2007. [29](#), [109](#)
- WAGNER, W. et al. Radio and visible light observations of matter ejected from the sun. *Astrophysics Journal*, v. 244, 1981. [34](#)
- WANG, Y. Eit waves and fast-mode propagation in the solar corona. *The Astrophysical Journal*, v. 543, n. 1, 2000. [26](#)
- WEBB, D. F. et al. Relationship of halo coronal mass ejections, magnetic clouds, and magnetic storms. *Journal of Geophysical Research*, v. 105, n. A4, 2000. [30](#), [109](#), [110](#)
- WEBB, D. F. et al. The origin and development of the may 1997 magnetic cloud. *Journal of Geophysical Research*, v. 105, n. A12, 2000. [30](#), [109](#), [110](#)
- WHITE, F. M. *Fluid mechanics*. [S.l.]: McGraw-Hill, 1986. [42](#)
- WOOD, B. et al. Comparison of two coronal mass ejections observed by eit and lasco with a model of an erupting magnetic flux rope. *Astrophys. J.*, v. 512, p. 484–495, 1999. [36](#)
- ZHANG, J. Coronal and stellar mass ejections. In: CAMBRIDGE: IAU, 226., 2005. *IAU SYMPOSIUM 2005*. Cambridge UK, Proceedings, 2005. p. 65–70. [37](#)
- ZHANG, J.; HOWARD, R.; VOURLILAS, A. *Astrophysics Journal*, v. 604, 2004. [34](#)
- ZHANG, J. et al. Solar and interplanetary sources of major geomagnetic storms (dst < - 100 nt) during 1996-2005. *Journal of Geophysical Research*, v. 112, n. A1, 2007. [91](#)

A energetics consideration

To have an idea of the energetic balance of the ICME - SW interaction process, i.e., the transport of the ICME in the interplanetary medium, we present a quantitative point of view of the balance of energy, (kinematic and magnetic), that takes place in the evolution of the ICMEs in the interplanetary medium.

First, from a kinematic point of view, we have the kinetic energy of a fast CME, with initial velocity of 1000 km/s (value near the base of the corona). If we consider a mass of approximately 10^{16} g, then the kinetic energy is:

$$E_k^0 = \frac{1}{2}mv^2 = 5 \times 10^{24} \text{Joule.} \quad (\text{A.1})$$

The kinetic energy at 1 AU for the ICME, considering a final velocity of 700 km/s, is:

$$E_k^f = 2.4 \times 10^{24} \text{Joule.} \quad (\text{A.2})$$

Therefore, the variation of energy, ΔE_k , is:

$$\Delta E_k = -2.6 \times 10^{24} \text{Joules.} \quad (\text{A.3})$$

On the other hand, the magnetic density energy that is stored in a volume with characteristic dimension of 1/4 AU (approximated radius of a ICME at 1 AU) can be calculated as:

$$E_{mag} = \frac{B^2}{2\mu_0} dV, \quad (\text{A.4})$$

where $\mu_0 = 4 \cdot \pi \times 10^{-7} \text{ weber/amp}\cdot\text{m}$ is the permeability of the free space, taking into account values of the quiet magnetic field measured in the interplanetary medium, ($|B| \approx 3nT$). Then the magnetic energy stored in a volume of interplanetary medium that is displaced by the ICME when it moves to the Earth is:

$$E_{mag} = 7.88 \times 10^{20} \text{Joules.} \quad (\text{A.5})$$

We can evaluate the magnetic energy stored in a standard loop fixed to the photosphere (of radius $10 \times 10^6 m$ and height $100 \times 10^6 m$), with a medium value of magnetic field equal to 10 Gauss. The result is:

$$E_{mag} = 1.22 \times 10^{22} \text{Joules.} \quad (\text{A.6})$$

With these assumptions the variation of energy, ΔE_{mag} , is:

$$\Delta E_{mag} = -1.14 \times 10^{22} \text{Joules.} \quad (\text{A.7})$$

We have that, in this energy balance, the kinetic energy is two orders of magnitude higher than the magnetic energy involved in the process, for this reason we do not take into account the magnetic interactions (in this first approach). In other words, we do not consider an explicit term for the magnetic field in the equation of motion.

B KOLMOGOROV-SMIRNOV TEST

The Kolmogorov-Smirnov test (CHAKRAVARTI; LAHA; ROY, 1967) is applicable to unbinned distributions that are functions of a single independent variable, that is, to data sets where each data point can be associated with a single number.

In this case, data points can be converted to an unbiased estimator $S_N(x)$, of the cumulative distribution function of the probably distribution. Given N ordered data points X_1, X_2, \dots, X_N , the $S_N(x)$ is the function giving the fraction of data points to the left of a given value x . This function is constant between consecutive x_i 's and jumps by the same constant $1/N$ at each x_i (see Figure (B.1)).

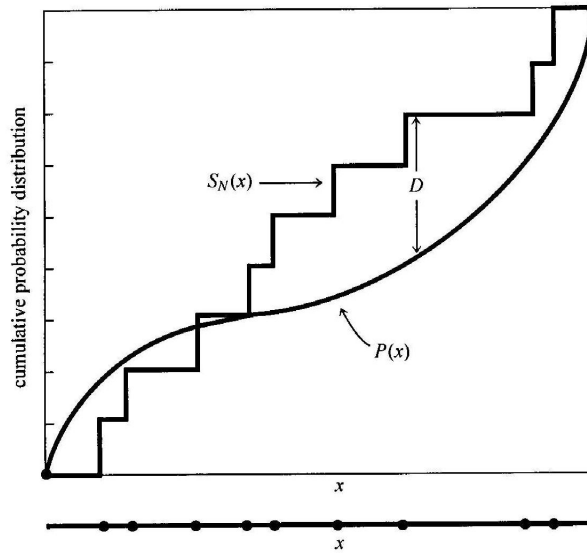


FIGURE B.1 - Kolmogorov-Smirnov statistics D . A measured distribution of values in x (shown as N dots on the lower abscissa) is to be compared with a theoretical distribution whose cumulative probability distribution is plotted as P_x . A step-function cumulative probability distribution $S_N(x)$ is constructed, on each rise an equal amount at each measured point. D is the greatest distance between the two cumulative distributions.

SOURCE: Numerical recipes.

Different distribution functions give different cumulative distribution functions estimates by the above procedure. All cumulative distribution function agree at the smallest allowable value of x (zero) and at the largest allowable value of x (unity). So it is the behavior between the largest and the smallest values that distinguishes

distributions. The Kolmogorov-Smirnov D is a measure that is defined ‘as the maximum value of the absolute difference between two cumulative distribution functions’. For comparing one data set’s $S_N(x)$ to an known cumulative distribution function $P(x)$, the K-S statistic is:

$$D = \max_{-\infty < x < \infty} | S_N(x) - P(x) |, \quad (\text{B.1})$$

and if it is necessary to compare two different cumulative distribution functions $S_{N_1}(x)$ and $S_{N_2}(x)$, the K-S statistic is:

$$D = \max_{-\infty < x < \infty} | S_{N_1}(x) - S_{N_2}(x) |. \quad (\text{B.2})$$

A central feature of the K-S test is that it is possible slide or stretch the x axis, and the maximum distance D remains unchanged.

An attractive feature of this test is that the distribution of the K-S test statistics itself does not depend on the underlying cumulative distribution function being tested. Another advantage is that it is an exact test (the chi-square goodness-of-fit test depends on an adequate sample size for the approximations to be valid). Despite these advantages, the K-S test has several important limitations:

- It only applies to continuous distributions.
- It tends to be more sensitive near the center of the distribution than at the tails.
- Perhaps the most serious limitation is that the distribution must be fully specified. That is, if location, scale, and shape parameters are estimated from the data, the critical region of the K-S test is no longer valid. It typically must be determined by simulation.

We use Equation (B.2) to measure the distance between two curves and then, ‘measure’ how close or far are two solutions.

C THEORY - TYPE II BURST

A way to quantify the coronal and interplanetary transport of CMEs is to use the fact that shocks, formed and driven by CMEs, can themselves generate (type II burst) radio emissions, which can be detected and tracked by remote sensing (MANOHARAN, 2006). There are different kinds of radio burst: Type I storm, Type II burst, Type III storm, slow drifting continuum, stationary Type IV storm, and fine structure bursts in storms (PICK; VILMER, 2005). We will briefly describe them here.

Type I storms usually have a duration of hours or days. The main characteristic is a narrow-band ($\Delta f/f = 0.025$) burst plus a broad-band continuum (50 to 100 MHz). The short duration of individual burst suggests local acceleration of electrons to a few times the thermal energy, and from the observed differences of the source height at each frequency, it is possible that plasma emission processes are involved.

The Type II burst show generally a slow drift ($< 1 \text{ MHz.s}^{-1}$) from high to low frequencies. The instantaneous bandwidth may be as narrow as a few megahertz. This drift in frequency is identified with outward motion of a shock wave, which is associated with the ejection of matter or sudden release of energy during a flare. Emissions occur at f_p and $2f_p$, probably by electrons accelerated within the shock front. We can recognize different kinds of Type II structures as (MCLEAN; LABRUM, 1985):

- 1) Herringbone structure in Type II burst: This variant of a Type II burst has many fine bursts, resembling Type II burst, that was originated in the ‘backbone’ of Type II burst and drifted to higher and/or lower frequencies. This give the appearance of a fishbone on the dynamic spectrum. The electrons accelerated by the shock front escape forward or backward (up or down in the corona) and generate bursts similar to Type III.
- 2) Split-band structure in Type II burst: During part of a Type II burst the fundamental and the harmonic bands are each double, with a separation of a few megahertz between the bands. The possible explanation for this split-band struture is the emission from the region in front of and from behind the shock front.
- 3) Multiple-band structure in Type II burst: The spectrum shows splitting into two or more bands which may have slightly different drift rates. This suggests that they are independent parts of the overall event. The interpretation is that the emission

bands come from different parts of the shock front. As the energy of the shock wave is refracted towards regions of low Alfvén speed, the shock front is fragmented, giving rise to discrete bands. The type III storm is the low-frequency ($f < 100\text{MHz}$) spectral extension of a storm. It consists of many type III bursts, up to thousands per hour. In this case the electrons which are accelerated in the energy release region of a Type I storm escape along open field lines. The emission process is the same as for other type III bursts.

The slow-drift continuum storm have the characteristic that the low frequency edge drifts from high to low frequencies. This slow drift is identified with rise of intruding magnetic field into the corona. This kind of event is always associated with eruptive prominences, and the emission mechanism is the same as for other Type I storms.

The stationary type IV burst generally have the shape of a storm that follows a major flare. The continuum of this burst is intense with manifestation of a few bursts, after that this storm evolves into a normal Type I storm, and without any shift of the source position. Exists, in the early stages of the event, a circular polarization that usually increases to levels close to 100 %.

And finally the fine structure burst in storms may be: Drift pairs: these bursts are rare and can occasionally be seen in great profusion during a Type III storm. They consist of short narrow-band burst, drifting to lower frequencies (forward drift pair) or to higher frequencies (reverse drift pair).

S-burst: these are bursts of very fine-structure and of very short duration. These burst are related to drift pairs.

Figure (C.1) shows a schematic representation of the different types of radio emission.

C.1 Mechanism of plasma emission

Plasma emission is the process for the majority of solar radio bursts at decimetric and longer wavelengths. The characteristic is a narrow band of emission near the plasma frequency and/or its harmonics, and polarization ranging from very weak to $\approx 100\%$, usually in a O-mode. From a theoretical point of view, plasma emission may be defined as any emission process in which the energy in Langmuir turbulence is converted into escaping radiation.

The first ideas of the process for the emission in solar radio burst (SHKLOVSKY, 1956) suggested that the possible mechanism for the emission is due to Langmuir

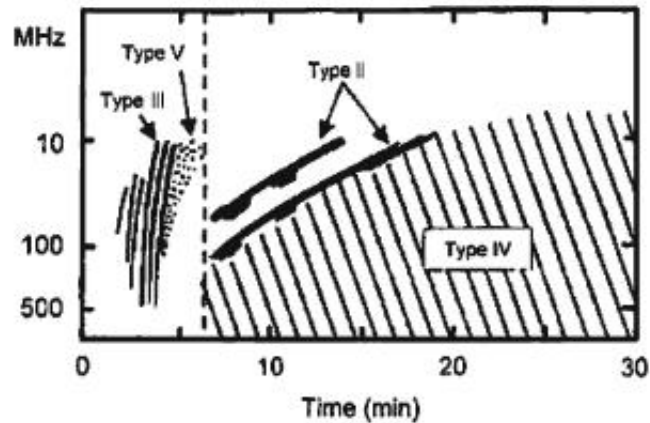


FIGURE C.1 - Idealized sketch of a complete radio event.

SOURCE: (PICK; VILMER, 2005)

waves, that could be generated through a streaming instability. The ideas on how the energy in the Langmuir waves might be converted into energy in scaping radiation is controversial. One suggestion, is in terms of transfer energy, in which the energy of Langmuir waves is converted into energy in fundamental transverse waves due to mode-mode coupling resulting from inhomogeneities in the plasma. Others authors (GINZBURG; ZHELEZNYAKOV, 1958) argued that the direct emission process is inefficient, and proposed an alternative mechanism in which the conversion is due to scattering off thermal ions.

The theory of scattering of thermal ions involves three process: 1) generation of Langmuir turbulence through a streaming instability, 2) conversion of Langmuir waves into fundamental transverse waves through scattering off thermal ions, 3) and coalescence of pairs of Langmuir waves into harmonic transverse waves. It is recognized that four process are involved in the production of plasma emission (ROBINSON, 1997):

- Generation of Langmuir turbulence.
- Partial conversion into fundamental transverse radiation.
- Production of secondary Langmuir waves.

- Generation of harmonic transverse radiation.

The first process, (generation of Langmuir turbulence), is related to an instability. In Type III burst is a streaming instability which produces waves with phase velocity:

$$\mathbf{V} = \frac{\omega}{k^2} \mathbf{k}, \quad (\text{C.1})$$

very close to the electron stream's velocity.

The second process involves scattering off thermal ions, or some process which causes little change in ω and allows k to be reduced from the large value for Langmuir waves to very small ($\ll \omega_p/c$) value for fundamental transverse waves. The scattering off particles with velocity \mathbf{V} has frequencies and wave vectors ω_1, \mathbf{k}_1 and ω_2, \mathbf{k}_2 of the scattered and unscattered waves and are related by:

$$\omega_1 - \mathbf{k}_1 \cdot \mathbf{V} = \omega_2 - \mathbf{k}_2 \cdot \mathbf{V}. \quad (\text{C.2})$$

In the case of thermal ions:

$$|\omega_1 - \omega_2| \leq k_2 V_i \quad \text{for } k_2 \gg k_1. \quad (\text{C.3})$$

The production of harmonic involves a three-wave process which satisfies:

$$\omega_1 + \omega_2 = \omega_3, \quad \mathbf{k}_1 + \mathbf{k}_2 = \mathbf{k}_3. \quad (\text{C.4})$$

The Langmuir waves have large \mathbf{k} and, for this reason the last equation in \mathbf{k} can be satisfied only for $\mathbf{k}_1 \approx -\mathbf{k}_2$. An intermediated step is the production of a secondary distribution of Langmuir waves. Harmonic emission may then result from coalescence either of waves from the primary and secondary distributions or of two waves from the secondary distribution. Thus harmonic emission is at least a three - stage process: 1) generation of the Langmuir waves, 2) scattering or other modification to produce secondary Langmuir waves, 3) coalescence of two Langmuir waves.

C.1.1 Induced scattering

Scattering off thermal ions is principally due to the scattering of the shield cloud of electrons that are co - moving with them. The induced scattering of Langmuir waves into transverse waves allows an exponential growth of the latter provided

that their frequency is below the frequency of the Langmuir waves. It is found that the induced scattering is important only for the fundamental transverse waves with brightness temperatures in excess of $T \approx 3 \times 10^9 \text{K}$. The problem is that it is difficult to account in this way for such high brightness temperatures, and it seems that a more efficient process than the scattering off thermal ions is required. The candidate is the coalescence with low - frequency waves.

C.1.2 Alternative forms of plasma emission

Another form of fundamental plasma emission involves a mode conversion due to inhomogeneity in the plasma. The Langmuir waves may be regarded as thermally modified Z - mode waves, that can couple in the solar corona and would lead to fundamental plasma emission.

Exists an alternative fundamental plasma emission process involving Langmuir waves. For a stream of electrons it is possible to be unstable and generate fundamental transverse waves with the presence of ion - sound or other low-frequency turbulence. The ion - sound turbulence can suppress the generation of Langmuir waves, and can stimulate the generation of transverse waves through a double - emission process.

All the processes mentioned may be treated using weak-turbulence theory. If the density in the Langmuir waves exceeds a certain threshold (10^{-4} of the thermal energy density) strong turbulence effects take over. In any case the radiation is produced by the ICME driven shock and the emission frequency may be used to trace the shock position (and the ICME position) at any time.

Livros Grátis

(<http://www.livrosgratis.com.br>)

Milhares de Livros para Download:

[Baixar livros de Administração](#)

[Baixar livros de Agronomia](#)

[Baixar livros de Arquitetura](#)

[Baixar livros de Artes](#)

[Baixar livros de Astronomia](#)

[Baixar livros de Biologia Geral](#)

[Baixar livros de Ciência da Computação](#)

[Baixar livros de Ciência da Informação](#)

[Baixar livros de Ciência Política](#)

[Baixar livros de Ciências da Saúde](#)

[Baixar livros de Comunicação](#)

[Baixar livros do Conselho Nacional de Educação - CNE](#)

[Baixar livros de Defesa civil](#)

[Baixar livros de Direito](#)

[Baixar livros de Direitos humanos](#)

[Baixar livros de Economia](#)

[Baixar livros de Economia Doméstica](#)

[Baixar livros de Educação](#)

[Baixar livros de Educação - Trânsito](#)

[Baixar livros de Educação Física](#)

[Baixar livros de Engenharia Aeroespacial](#)

[Baixar livros de Farmácia](#)

[Baixar livros de Filosofia](#)

[Baixar livros de Física](#)

[Baixar livros de Geociências](#)

[Baixar livros de Geografia](#)

[Baixar livros de História](#)

[Baixar livros de Línguas](#)

[Baixar livros de Literatura](#)
[Baixar livros de Literatura de Cordel](#)
[Baixar livros de Literatura Infantil](#)
[Baixar livros de Matemática](#)
[Baixar livros de Medicina](#)
[Baixar livros de Medicina Veterinária](#)
[Baixar livros de Meio Ambiente](#)
[Baixar livros de Meteorologia](#)
[Baixar Monografias e TCC](#)
[Baixar livros Multidisciplinar](#)
[Baixar livros de Música](#)
[Baixar livros de Psicologia](#)
[Baixar livros de Química](#)
[Baixar livros de Saúde Coletiva](#)
[Baixar livros de Serviço Social](#)
[Baixar livros de Sociologia](#)
[Baixar livros de Teologia](#)
[Baixar livros de Trabalho](#)
[Baixar livros de Turismo](#)